

DEVELOPMENT AND PRECLINICAL EVALUATION OF A COMPACT
IMAGE-GUIDED MICROBEAM RADIATION THERAPY SYSTEM

Lei Zhang

A dissertation submitted to the faculty at the University of North Carolina at Chapel Hill in
partial fulfillment of the requirements for the degree of Doctor of Philosophy in the
Department of Applied Physical Sciences.

Chapel Hill
2016

Approved by:

Otto Zhou

Jianping Lu

Sha Chang

Hong Yuan

Sean Washburn

Joel Tepper

© 2016
Lei Zhang
ALL RIGHTS RESERVED

ABSTRACT

LEI ZHANG: Development and Preclinical Evaluation of a Compact
Image-guided Microbeam Radiation Therapy System

(Under the direction of Otto Zhou)

Microbeam radiation therapy (MRT) is a novel and experimental cancer treatment modality. It has received increasing emphasis worldwide in recent years due to the demonstrated high therapeutic ratio in preclinical studies. MRT uses arrays of quasi-parallel radiation beams that are up to a few hundred microns wide and separated by several times of its beamwidth. Extensive preclinical experiments conducted at European Synchrotron Radiation Facility and several other national synchrotron facilities have shown that microbeams with doses of several hundreds of grays are well tolerated by healthy brain tissues while causing preferential damage in tumors. As the effort now moves towards large animal and clinical trials, there are eminent needs to develop compact and economically-viable microbeam irradiators for MRT radiobiology research and clinical installation eventually.

Our research group has invented the carbon nanotube (CNT) field emission based X-ray source technology and has been dedicated to CNT-based medical device research over the past decade. A laboratory-scale microbeam irradiator has been recently developed with

the CNT source array technology. The unique nature of CNT X-ray cathode allows for optimization of the anode focal spot shape and size, and therefore overcomes the obstacles of producing high flux microbeam radiation with conventional X-ray tubes. Preliminary studies have shown that the CNT-based MRT prototype is capable of generating orthovoltage radiation with all essential dosimetric characteristics of microbeam radiation therapy. The goals of this dissertation are to characterize and to optimize the system performance, to implement image guidance for dose delivery, and to evaluate the treatment efficacy in preclinical studies.

Characterization of radiation source and dosimetric parameters was performed and described in detail. An on-board imaging system was constructed and integrated with the microbeam irradiating system. Dedicated image-guidance protocols were developed for high accuracy microbeam delivery in small animal models. Therapeutic assessment of brain tumor bearing mice was conducted with the CNT-MRT prototype. Preliminary results included encouraging treatment effects in terms of tumor local control and mean survival time extension. MRT radiobiological evaluations were carried out, for the first time, using a non-synchrotron-based compact radiation source. Additionally, feasibility of delivering multi-arrays of microbeams cross-firing geometry at the brain tumor target was successfully demonstrated facilitated by multi-modality 3D image guidance.

The results in this work demonstrate the advantages of CNT-based MRT system as an attractive alternative for microbeam generation and delivery. With continued effort in system development and optimization, this nanotechnology-based compact MRT system could

become a powerful research tool that can be installed in a laboratory environment for elucidating the still poorly understood therapeutic mechanism of MRT without the need of synchrotron light sources. The feasibility studies also showed that the CNT-based MRT technology offers a promising pathway for clinical implementation in the near future.

To my parents

ACKNOWLEDGEMENTS

First and foremost, I would like to express my sincere gratitude to my advisor, Dr. Otto Zhou, for his guidance through my graduate studies. He is truly a great mentor and has inspired me in so many ways in my professional growth. His insights, expertise, and dedication to research and the advancement of medical technologies have been a great source of motivation through these years. It has been a privilege to work with him and conduct research under his supervision. I would like to thank Dr. Jianping Lu for his direction and help in addressing the challenges and obstacles in completing this work. Beyond that, I must thank both Dr. Lu and Dr. Zhou for their kindness and patience in helping me build up confidence. I'm deeply grateful to Dr. Sha Chang, who has guided me into the field of medical physics. I admire her vision in this field, and every discussion with her was enlightening to me. The small animal studies that constitute a great portion of this work were carried out as a collaborative work with Dr. Hong Yuan. It's her tireless support in all aspects that has made this work possible. It was a pleasure to work with her. I would also like to thank Dr. Joel Tepper for his thoughtful inputs in my research. It is an honor to have him on my committee. I must thank Dr. Sean Washburn, for being such a great director for the graduate studies in the department of applied sciences, for his advises in my research, and for being a good friend of mine.

I would like to thank the amazing members in our group, past and present: Christy Inscoe, Pavel Chtcheprov, Soha Bazyar, Jabari Calliste, Allison Hartman, Gongting Wu, Yueh Lee, Emily Gidcumb, Laurel Burk, Mike Hadsell, Andrew Tucker, Marci Potuzko, Jing Shan, Rachel Ger, Xin Qian, and Sigen Wang. Specially, I must thank Christy who I have been working closely on this project for the past three years. She has been so kind and supportive, and has taught me so many things over these years. This work would not have been completed without her. Thanks to all my friends for being here while I'm here, during joyful moments and struggling time. They all have made these years so much more colorful.

This project was funded through the National Cancer Institute and the Carolina Center of Cancer Nanotechnology Excellence. I would also like to thank the generous support from the Royster Society of Fellows and The Ross and Charlotte Johnson Family Dissertation Fellowship in completing this thesis.

Last but not least, I thank my dearest parents. They are the greatest source of motivation and support throughout years of education. Thanks for teaching me to be grateful for what I have been given, and for teaching me to make dreams come true through my own efforts. I'm proud to be the daughter of yours.

The first time I stepped onto our beautiful campus as a Carolina student with all my curiosities and enthusiasm, I did not realize that I would be building a bridge between the smallest material structures and a medical solution that could potentially benefit patients that suffer from cancer. The past six years' graduate training in such an interdisciplinary group has completely changed my perspective of how to turn thoughts into actions, and how basic

sciences can revolutionize daily life. What I have learned is far beyond the content of this thesis, and will be a lifetime fortune that continues to benefit me in the years to come.

TABLE OF CONTENTS

LIST OF TABLES	XV
LIST OF FIGURES	XVI
LIST OF ABBREVIATIONS.....	XXV
CHAPTER 1: INTRODUCTION	1
1.1 Radiotherapy for Cancer Management	1
1.2 Microbeam Radiation Therapy – Roots, Status, and Prospects	5
1.2.1 History and inspiration.....	5
1.2.2 Synchrotron-based microbeam radiation therapy	8
1.2.2.1 Experimental characteristics	8
1.2.2.2 Biological features	11
Overview.....	11
Bystander effects.....	13
Vasculature responses.....	14
1.2.3 Compact microbeam delivery systems – challenges and efforts	16
1.3 The Scope of This Work.....	17
References.....	20
CHAPTER 2: CARBON NANOTUBE FIELD EMISSION SOURCE ARRAYS	28
2.1 Overview.....	28
2.2 Structures and Physical Properties of Carbon Nanotubes.....	28
2.3 Field Emission from Carbon Nanotubes.....	30

2.3.1	Fundamentals of field emission theory	30
2.3.2	Carbon nanotubes as field emitters	33
2.3.3	Carbon nanotube field emission X-ray technology	35
2.3.4	Carbon nanotube source array based medical devices.....	37
2.3.4.1	Diagnostic imaging devices	38
2.3.4.2	Radiotherapy systems for preclinical studies.....	45
	Cellular irradiator and multi-pixel micro-radiotherapy system	45
	Image-guided microbeam radiation therapy system	45
	References.....	47
CHAPTER 3: DEVELOPING A COMPACT MICROBEAM IRRADIATOR USING THE CARBON NANOTUBE FIELD EMISSION SOURCE ARRAY.....		52
3.1	Overview.....	52
3.2	The First-generation Prototype	55
3.2.1	Main components.....	56
3.2.2	Source characteristics.....	60
3.2.2.1	Tube specifications in standard mode of operation (full power)	61
3.2.2.2	Photon energy spectrum.....	62
3.2.2.3	Focal line size	62
3.3	Dosimetric Characteristics	63
3.3.1	Film dosimetry with Gafchromic EBT2/EBT3 films	64
3.3.2	Half value layer (HVL).....	69
3.3.3	Dose rate	71
3.3.4	Distance correction	72
3.3.5	Percentage depth dose (PDD).....	75

3.3.6	Tissue maximum ratio (TMR)	76
3.4	Challenges and Remedies	79
3.4.1	Microbeam collimator alignment.....	79
3.4.2	Anode rotation	84
	References.....	89
CHAPTER 4: IMAGE GUIDANCE FOR MICROBEAM RADIATION THERAPY		91
4.1	Motivation.....	91
4.2	Implementing Image Guidance for Microbeam Delivery.....	92
4.2.1	Construction of the imaging system	92
4.2.2	Integration of the IGMRT system.....	95
4.2.3	Design of the animal positioning device.....	96
4.2.4	Peripheral components.....	99
4.2.5	System calibration and testing	100
	References.....	101
CHAPTER 5: IMAGE-GUIDED MICROBEAM DELIVERY IN SMALL ANIMALS.....		102
5.1	Motivation.....	102
5.2	Delivery of Single Array Microbeams in Mouse Brain with 2D Image Guidance ..	104
5.2.1	Methods.....	104
5.2.1.1	Tumor cell and animal preparation	105
5.2.1.2	Imaging and beam planning.....	106
5.2.1.3	Image processing and registration	108
5.2.1.4	Microbeam alignment and irradiation.....	109
5.2.1.5	Beam verification using immunohistological staining	111
5.2.2	Results.....	112

5.2.2.1	Dose verification	112
5.2.2.2	Immunohistological staining.....	114
5.2.3	Discussion.....	116
5.3	Multi-array Microbeam Irradiation in Brain Tumor Bearing Mice	119
5.3.1	Upgrade in animal positioning device	120
5.3.2	Image guidance protocols	123
5.3.2.1	Two-view planar image guidance with 2D image registration	123
5.3.2.2	MRI/CT guidance with 3D image registration	126
	References.....	134
CHAPTER 6: PRECLINICAL EVALUATION OF MRT THERAPEUTIC EFFICACY USING THE COMPACT IRRADIATOR.....		136
6.1	Introduction.....	136
6.2	Methods and Materials.....	137
6.2.1	Brain tumor bearing mouse model.....	137
6.2.2	Image guidance	138
6.2.2.1	Unidirectional microbeam array	138
6.2.2.2	Crossbeam MRT	139
6.2.3	Radiation treatment.....	139
6.2.3.1	Microbeam radiation therapy.....	139
6.2.3.2	Broad-beam radiation treatment	140
6.2.4	Survival & statistical analysis.....	141
6.2.5	Immunohistological analysis	141
6.2.5.1	Characterize DNA damage with γ -H2AX staining.....	143
6.2.5.2	Characterize cell apoptosis using cleaved caspase-3	143

6.2.5.3	Characterize cell proliferation using Ki-67 immunofluorescence staining	144
6.3	Results	144
6.3.1	Verification of dose delivery	144
6.3.2	Microbeam effects on the mean survival time	146
6.3.3	Microbeam effects on tumor local control	146
6.3.4	Microbeam radiation induced DNA damage and its dynamics	148
6.3.5	Microbeam effects on apoptosis and cell proliferation	149
6.3.6	Preliminary results with MRT delivered in orthogonal arrays	154
6.4	Discussion	155
	References	161
CHAPTER 7: CONCLUSIONS AND PROSPECTS		163
7.1	Summary of This Work	163
7.2	High-power Compact MRT System	165
7.2.1	The second-generation prototype	165
7.2.2	Design for human MRT with multiple beam arrays	166
7.3	Future Directions	167
	References	169

LIST OF TABLES

Table 2.1 Selected physical properties of carbon nanotubes [3, 6]	30
Table 3.1 Selected parameters for full power operation of the first CNT-MRT prototype	61
Table 4.1 Characteristics of the three cathodes in the micro-focused tube of the CT scanner	93
Table 5.1 A flow chart illustrating the procedure of multi-modality image-guided microbeam radiation therapy in brain tumor bearing mouse models.	105
Table 5.2 Summary of the uncertainties in beam targeting using the 2D image-guided MRT protocol. Pictures are reprinted with permission from Zhang <i>et al. Physics in Medicine and Biology</i> 59, 1283-1303 (2014) [1].	116
Table 5.3 Summary of the results from the MRI/CT image guided MRT delivered in orthogonal arrays.	130
Table 6.1 Summary of the biological studies carried out with the CNT-MRT system	137
Table 7.1 Comparison of the system specifications of the first and second generation CNT-based MRT prototypes.....	167

LIST OF FIGURES

Figure 1.1 The radiation biology flow chart (Lecture handout for Radiation biology at UNC Chapel Hill. Reprinted with permission from Dr. Elaine Zeman, UNC Department of Radiation Oncology)	2
Figure 1.2 Histopathologic evidence of different radiobiological effects caused by microscopic versus millimeter-sized deuteron beam on the visual cortex of the mouse brain, which is a direct proof of the dose-volume effect. Adapted from Zeman W. et al., Radiation Research 15, 4 (1961).....	7
Figure 1.3 A photo of the sample positioning stage in the MRT experiment room at ESRF Biomedical Beamline ID17	10
Figure 2.1 Electronic density of states for two zigzag carbon nanotubes, a metallic (9, 0) one on the left, and a semiconducting (10, 0) one on the right. Reprinted from Saito et al. <i>Applied Physics Letters</i> 60(18), 1992 [5].....	30
Figure 2.2 A schematic illustration of the potential energy of electron $U(x)$ (in eV) as a function of the distance x from the metal surface in an external static electric field. The effective energy barrier is sufficiently narrowed that the electrons could tunnel through. Horizontal dotted line illustrates the energy barrier width for electrons at Fermi level to tunnel through.....	31
Figure 2.3 The configuration of an X-ray tube with the CNT field emission cathode. G represents the gate mesh where the electrostatic potential is applied for electron extraction. F1 and F2 are focusing electrodes for customizing the shape of the electron beam as well as the resultant focal spot on the anode. High voltages (kV) are applied between the cathode and anode for electron acceleration and X-ray generation. All parts are sealed inside an evacuated housing with a thin layer of window material as X-ray exit port. Electronic control circuit is now shown here for simplicity purpose.....	36
Figure 2.4 A schematic illustration (left) of a multi-beam x-ray source with five individually controlled CNT emitting pixels [53]; and examples of CNT-based X-ray tubes with multiple sources and in linear (middle) or square (right) geometries, photos courtesy of XinRay Systems Inc.	37
Figure 2.5 Top: a photo of the CNT field emission based microfocus X-ray tube built in the CNT-based micro-CT scanner. Reprinted from Cao et al. <i>Medical Physics</i> 37 (10), 2010 [57]. Bottom left: a photo showing the main components of the CNT micro-CT scanner including a rotating gantry, a CNT-based microfocus X-ray tube, a high-resolution flat panel detector, a high voltage power unit, and a sample stage. The gantry and sample stage are mounted on an optical table. Bottom right: a photo of the external appearance of the CNT micro-CT scanner Charybdis enclosed inside a painted shielding housing	40
Figure 2.6 Left: the original Hologic Selenia Dimensions DBT system with a rotating gantry; middle: the prototype s-DBT system with a linear CNT source array retro-fitted into the Hologic	

Selenia Dimensions scanner; right: a photo of the s-DBT prototype installed at North Carolina Cancer Hospital (Chapel Hill, NC) for clinical trial [68].	42
Figure 2.7 Comparison of the reconstructed images from s-DBT and DBT in human specimen study. Photos adapted from Tucker et al. Proc. of SPIE Vol. 9033, 903316 Medical Imaging 2014 [70]	43
Figure 2.8 The s-DCT prototype installed at the Cystic Fibrosis and Pulmonary Diseases Research and Treatment Center, at UNC Marsico Lung Institute for clinical trials.....	44
Figure 3.1 Schematic drawing illustrating the difference of point focus and line-focusing X-ray sources, the microbeam collimator needed for each source, and the resultant dose profiles.	52
Figure 3.2 Schematic drawings of the design concept of compact high-flux microbeam delivery systems with multiple arrays of CNT generated microbeams arranged in a ring (left) or a square (right) configuration around the target to achieve dose conformality physically. Customized MRT treatment can be delivered by electronically programming the on-and-off status of individual cathode segments.	54
Figure 3.3 A photograph of the CNT-MRT first prototype constructed on an optical table inside a shielded enclosure in our lab at UNC Chapel Hill. Some of the main external components are indicated. Secondary shielding panels are also installed surrounding the MRT tube on the optical table during operation. As can be seen, a CNT-based micro-CT scanner is built on the same optical table to provide image guidance.	55
Figure 3.4 Illustration of the main components of the CNT-MRT system including the photon production structures enclosed in the vacuum chamber, and the microbeam collimator underneath the X-ray window.....	56
Figure 3.5 Top left: a photograph of the CNT cathode. The area in black is the deposited layer of CNT emitters. Top right: SolidWorks drawings (trimetric view) of the cathode assembly. Bottom: cross-sectional view. Main structures are labeled, including the cathode (CNT emitters deposited on molybdenum substrate), gate mesh, and two focusing electrodes.	58
Figure 3.6 SolidWorks drawings of the microbeam collimator assembly.....	60
Figure 3.7 The measured photon energy spectrum measured using AmpTek XR-100T-CeTl X-ray detector (top), and the simulated spectrum using SpekCalc (bottom).....	63
Figure 3.8 Illustration of the different layer configurations of Gafchromic EBT2 (left) and EBT3 (right) films [13].	65
Figure 3.9 Top: Illustration of the side-by-side setup of EBT3 film and an ion chamber in the cross-calibration process. A piece of EBT3 film was placed between two thin layers of plastic, with the plane of EBT3 film aligned with the central plane of the ion chamber. Bottom: Illustration of the sectional view of an ion chamber, with sensitive air cavity and collecting electrode indicated.....	67

Figure 3.10 Dose responding curves of EBT3 film (lot number 07221303) in three color channels obtained through cross calibration to ion chamber. The system was operating in standard mode at full power, i.e. 160 kVp, 30mA tube current, 500 μ m pulse width at 8% duty cycle. Spline-fitted are shown only to guide the eyes. 68

Figure 3.11 A photograph (left) and drawing (right) of the aluminum step phantom for half value layer measurement. The phantom has a total of ten identical steps, with each being 2.54 mm in height and 7.56 mm in width. The direction of microbeam penetrating through the step is indicated. The measurement EBT3 film sandwiched between two thin layers of acrylic was placed underneath the phantom. The dimensions are not drawn to scale. 70

Figure 3.12 Results of HVL determination. Measurements were carried out in step-and-shoot mode with ten microbeam exposures onto each step of the aluminum phantom. The absorbed doses from ten exposures were recorded by a single piece of EBT3 film placed underneath the phantom. The successive exposures were separated horizontally far enough to avoid the effect or scatter from the previous or subsequent exposures..... 71

Figure 3.13 Results from the average dose rate measurements that were performed with the system operating at 160 kVp, 30 mA anode current, 8% duty cycle, and 500 μ s pulse width. The film was placed at 122.10 mm down from the focal line..... 72

Figure 3.14 The distance correction curve obtained using EBT3 films, for SSD between 114 to 140 mm, with the system operating at 160 kVp, 30 mA tube current, 8% duty cycle, and 500 μ s pulse width. 74

Figure 3.15 Beam profiles (bottom) at different distances recorded by the EBT3 film (top) during the measurement of distance correction curve. The beam center-to-center distance shown in this figure does not correspond to the vertical distance translation, but the horizontal translation distance between two successive exposures on the film..... 74

Figure 3.16 Illustration of the acrylic phantom for PDD measurement. Each slab was 2.8 mm thick. Seven pieces of EBT3 films were inserted between adjacent layers. One microbeam irradiation was carried which exposed all seven films simultaneously at 8° angle, as shown in the side view of the phantom on right. The figure is not drawn to scale. 75

Figure 3.17 Percentage depth dose (PDD) curve taken with EBT3 films and the acrylic phantom placed at 22.19 mm down from the bottom of the collimator. 76

Figure 3.18 Photographs of the acrylic step phantom for the measurement of TMR..... 77

Figure 3.19 The tissue attenuation of the microbeam in acrylic. Data were obtained using EBT3 film placed at 122.10 mm downstream from the focal line. 79

Figure 3.20 Left: Illustration of setup and irradiation configuration for microbeam collimator alignment; right: beam profile recorded on the detector. Dimensions are not drawn to scale. 82

Figure 3.21 Top row: Screenshots of the detector readout of the beam profile and photon flux during the collimator alignment. Two segments appear shifted if the collimator slit is not in

parallel position with respect to the focal line on the anode, as shown on the left. The one on the right indicates a parallel-aligned slit and focal track. Middle row: images acquired by the detector shown in ImageJ. Bottom row: illustrations of the relative locations of the collimator slit and the anode focal line when not-aligned (left) and aligned (right) corresponding to the beam profiles as shown in the top and middle row. Dimensions are not drawn to scale. 83

Figure 3.22 Comparison of the beam profiles before (right) and after (left) collimator alignment. Notice the change in the beam shape and peak dose rate. 84

Figure 3.23 Left: Non-tilted (in both vertical and horizontal directions) anode as originally installed. Right: the rotated anode with further end from the plane of the paper drifted towards the cathode assembly, while the closer end moved towards the back wall of the chamber. 85

Figure 3.24 Left: SolidWorks drawing highlighting the cylinder that connects the anode to the HV feedthrough with two threaded joints on both ends. Right: two setscrews were added subsequently after the anode rotation was found, to prevent any rotation that might have occurred at the joints on the cylinder from the side towards the back wall of the vacuum chamber. 86

Figure 3.25 SolidWorks drawing and a photograph (bottom view) of the anode assembly highlighting the two setscrews at the bottom of the anode. 87

Figure 3.26 Left: original design of the anode assembly. Right: modified design of the L-bracket to avoid anode rotation. 88

Figure 4.1 SolidWorks design of a compact system for micro-CT guided microbeam radiation therapy. 92

Figure 4.2 Left: A photograph of the micro-CT scanner built on the side of the microbeam irradiator, with key components indicated with red arrows. The gantry stands on top of the optical table, facing the back side of the turbo pump on the microbeam irradiator. Right: control console for the micro-CT outside the shielded enclosure. 94

Figure 4.3 Illustration of the changes made to the turbo pump support (highlighted in blue color) in the microbeam irradiator, and the extended tube stand. Drawing on the left is the original design, while the one on the right demonstrates the modification. 95

Figure 4.4 SolidWorks drawing of the home-made mouse holder. The design includes two parts, i.e. the main body of the holder and a nosecone holder attached on top. [7]. 97

Figure 4.5 A photo of a nude mouse positioned on the mouse holder under anesthesia. 98

Figure 4.6 SolidWorks drawings of the modified mouse holder for P12 mouse pups (left); and the double-stage (right). 98

Figure 4.7 A photo of the anesthesia setup equipped to the CNT-MRT system for small animal studies. 99

Figure 4.8 A photograph of the CNT-based image-guided microbeam radiation therapy system constructed on an optical table in our lab at the University of North Carolina at Chapel Hill... 100

Figure 5.1 Illustration of a single array of microbeams irradiating the mouse brain. The relative locations of target, landmarks, and radiation field are defined by a Cartesian coordinate system as indicated..... 104

Figure 5.2 Top row: on the left is a picture of animal immobilized on the customized mouse holder under anesthesia, while on the right is a picture showing the setup of double-mouse imaging. Bottom row: illustrations of two mice imaged by the micro-CT scanner one after the other, in the image-and-shift manner. Pictures are reprinted with permission from Zhang *et al. Physics in Medicine and Biology* 59, 1283-1303 (2014) [1]. 106

Figure 5.3 Left: MR image of the mouse brain with the targeted tumour circled. Middle: X-ray projection of the same animal showing the landmark ear bars and skull features. Right: X-ray projection registered with MR image showing the relative position of the tumour and ear bars. Pictures are reprinted with permission from Zhang *et al. Physics in Medicine and Biology* 59, 1283-1303 (2014) [1]. 108

Figure 5.4 Diagram showing the geometric relations between the targeted tumor, landmark, and microbeam locations. The z-direction is perpendicular to the paper plane. The microbeam plane is in the y-z plane. Δx_1 is the distance from the tumor to the ear bars measured in the registered image, Δx_2 is the distance of translation from the MRT chamber to the micro-CT, and Δx_3 is the distance between the center of the ear bar and the alignment microbeam track measured during microbeam alignment. The mouse holder with the Gafchromic film was first irradiated for beam alignment, as shown on the left, and then translated to the right, followed by mouse positioning and X-ray imaging. Pictures are reprinted with permission from Zhang *et al. Physics in Medicine and Biology* 59, 1283-1303 (2014) [1]. 109

Figure 5.5 Left: illustration of the beam planning procedure based on the size and location of the tumor from the registered image. Regions in green color are from the MR layer showing soft tissue contrast, while bony structures and the mouse bed presented in the planar X-ray images are overlapped on top. The red lines indicate the microbeams penetrating through the tumor target (outlined in darker green). Microbeams project at an 8° angle from collimator tile as described in Chapter 3. Right: a picture of the double-mouse setup in the microbeam irradiator, ready for treatment. The pink plane indicates the microbeam entrance plane. Also noticeable is the heat lamp placed inside the lead chamber. The heat lamp switch is controlled electronically to maintain a proper body temperature in the mice. Pictures are reprinted with permission from Zhang *et al. Physics in Medicine and Biology* 59, 1283-1303 (2014) [1]. 110

Figure 5.6 Pictures of the recovering animal on the mouse holders. As shown here, Gafchromic films were placed at the beam entrance, exit, as well as on the side of the mouse bed, to verify the delivered radiation dose and beam patterns. 112

Figure 5.7 Beam patterns recorded by Gafchromic EBT2 films at the entrance (top left) and exit (top right) planes on the mouse head, and corresponding dose profiles (bottom) analyzed by FilmQAPro program (using multi-channel dosimetry). The beam width at the entrance plane is

about 280 microns, and 380 microns at the exit plane. The PVDRs recorded for this animal were roughly 16 at the entrance plane, and 15 at the exit plane. Pictures are reprinted with permission from Zhang *et al. Physics in Medicine and Biology* 59, 1283-1303 (2014) [1]. 113

Figure 5.8 Fluorescence images of γ -H2AX stained mouse brain tissue slices after microbeam irradiation. The γ -H2AX foci-positive cells, shown as pink strips, correspond to the microbeam pattern. Areas circled in yellow are tumour targets. The images correspond to animal ID 1087 (left) that was treated with two microbeams with 109 Gy/beam, and 1089 (right) which received a single microbeam radiation with 138 Gy entrance dose. In both cases, microbeams were delivered right on target as planned. Pictures are reprinted with permission from Zhang *et al. Physics in Medicine and Biology* 59, 1283-1303 (2014) [1]. 114

Figure 5.9 Comparison of the γ -H2AX stained mouse brain tissue slices from animal ID 1152 and ID 1149 both treated with three microbeams with 48 Gy/beam entrance dose. As labeled in the images, three planned microbeams were delivered on target for the case on left, while for the one right, two out of the planned three microbeams were delivered off-target. Pictures are reprinted with permission from Zhang *et al. Physics in Medicine and Biology* 59, 1283-1303 (2014) [1]. 115

Figure 5.10 γ -H2AX stained, sagittal image registered with MR projection for the same slice of tissue, from two animals (Left: ID 1152 and right: ID 1145) irradiated with three microbeams of 48 Gy/beam. Microbeam tracks are the pink strips through the higher contrast tumour region, demarcated by the yellow circle. The targeting error was measured from the microbeam location to the targeted tumour center. Pictures are reprinted with permission from Zhang *et al. Physics in Medicine and Biology* 59, 1283-1303 (2014) [1]. 115

Figure 5.11 Illustration of two orthogonal arrays of microbeams traversing through the mouse brain..... 120

Figure 5.12 Photographs of the setup for delivery two perpendicular arrays of microbeams in the cross-beam configuration. A mouse phantom is placed on the mouse holder, and the green lines demonstrate the microbeam entrance location on the mouse head. 122

Figure 5.13 SolidWorks drawings of the modified sample stage and mouse holder. The three mounting positions are indicated with dash lines (top right), and illustrated on the bottom row. 122

Figure 5.14 Registered MR/X-ray projections in sagittal view (left) and coronal view (right) for the same animal. The tumor target was circled out in green line. The tumor measured $1.5 \times 2 \text{ mm}^2$ in the sagittal plane, and $2 \times 2 \text{ mm}^2$ in the coronal plane..... 124

Figure 5.15 Left: A photograph of the U87MG human glioma bearing mouse after treatment of two orthogonal arrays of microbeams. As shown in the Gafchromic EBT3 films, each array consisted four 300 μm wide microbeams at equal spacing (900 μm c-t-c distance). Right: an image of γ -H2AX stained mouse brain tissue (sliced in coronal plane) from the same animal, capturing the microbeam patterns (pink lines) and the covered tumor target ($\sim 2 \text{ mm}$ in diameter).

Animal euthanization was performed 4 hours after radiation was completed for tissue collection and fixation.	125
Figure 5.16 Top: screenshot of the user interface of <i>PLUNC</i> , clinical treatment planning software developed at UNC Department of Radiation Oncology. A special edition was installed on the desktop computer for micro-CT operation. Bottom: a screenshot showing 3D registration (sagittal view) of a MR scan and CT scan of a mouse in <i>PLUNC</i> . Soft tissue contrast in MR image (shown in red) and the contrast in bony structures presented in CT (shown in green) can be adjusted individually. Translation and rotation are performed in three anatomical planes (coronal, sagittal, and axial).	127
Figure 5.17 Image registration in three anatomical planes using <i>PLUNC</i> . Tumor target is shown with hyper-intense signal from MR images (in green) with the center of volume indicated with a cross mark.	128
Figure 5.18 Photographs of the new mouse holder designed for crossbeam MRT. A metal bb (Aluminum, 0.79 mm in diameter) is embedded on the ear bar pillar as indicated. The picture on left is from a phantom study to test the reposition consistency of the sample stage, and the picture on right is from U87 bearing mouse irradiated with crossbeam MRT.	129
Figure 5.19 γ -H2AX stained tissue slices and the corresponding MR slices from animal ID 1293 (top row) and 1300 (bottom row). Tumor targets are indicated with yellow arrows in the histology slices. For both animals, one out of the two microbeam arrays was delivered accurately on tumor target. Beam array 2 was delivered off-center by about 350 μm for animal ID 1293, and 900 μm for animal ID 1300.	131
Figure 5.20 γ -H2AX stained tissue slices and the corresponding MR images for the other three animals with ID 1294, 1295 and 1298.	132
Figure 6.1 Illustration of the configuration of a mouse being irradiated in the head using the microbeam generated by the CNT-based microbeam radiation therapy system. The source-to-surface distance was kept at 124 mm for all treated animals.	140
Figure 6.2 Top row: microbeam profiles recorded by Gafchromic EBT2 films placed at the radiation entrance (left) and exit (right) planes on the mouse head. Middle row: images of γ -H2AX stained brain tissue from a normal mouse (left) and a brain tumor bearing mouse (right). The positive expression of γ -H2AX, shown as pink strips, correspond to the tracks of microbeam radiation dose deposition, which induced DNA double strand breaks in both normal and tumor cells. Bottom row: the beam profiles drawn from the histology slices. Reprinted with permission from Yuan <i>et al. Radiation Research</i> 184, 322-333 (2015) [3].	145
Figure 6.3 Survival curves of U87MG bearing mice with different treatments. Animals in the sham group were anesthetized with isoflurane without any radiation treatment. BRT group was treated with 10 Gy conventional radiation with a 1 cm \times 1 cm field size, using a clinical linear accelerator. Radiation doses were 48 Gy/microbeam and 72 Gy/microbeam for low-dose MRT and high-dose MRT groups, respectively. Reprinted with permission from Yuan <i>et al. Radiation Research</i> 184, 322-333 (2015) [3].	146

Figure 6.4 A: T2 weighted MR images of the mouse brains before and after different treatment. Tumor targets were contoured with white dash lines. B and C: absolute and relative tumor volumes growth calculated from the MR images. Reprinted with permission from Yuan *et al. Radiation Research* 184, 322-333 (2015) [3]. 147

Figure 6.5 γ -H2AX stained normal mouse brain tissue and brain tumor tissue after microbeam treatment. A: changes of γ -H2AX positive signal at different times post-irradiation. Microbeam paths were clearly distinguishable from the background in both tumor region and normal tissue at 1h and 24h post-irradiation. The beam tracks blurred out in tumor at 48h and 7 days after radiation, which was not observed in normal tissue in contrast. B and C: quantification of the γ -H2AX expression. The expression decreased over time after treatment, indicating the cell repair process. Reprinted with permission from Yuan *et al. Radiation Research* 184, 322-333 (2015) [3]. 149

Figure 6.6 Immunofluorescence staining of cleaved caspase-3 as cell apoptosis assay. Cleaved caspase-3 signal is shown in red, while DAPI counterstaining of the nuclei is shown in blue. A and B: Levels of apoptosis in tumor at 1h and 7d after MRT. Reprinted with permission from Yuan *et al. Radiation Research* 184, 322-333 (2015). 150

Figure 6.7 Immunofluorescence staining of Ki-67 on tumor as biomarker for cell proliferation 1h (A) and 48h (B) after MRT. Ki-67 positive cells are shown in red, while DAPI counterstaining of the nuclei are shown in blue. White arrows indicate the microbeam radiation paths on the tumor. Ratios of proliferation staining to non-irradiated control are plotted (C) over time for both the peak and valley regions. Proliferation rate continuously decreased from 1h to 48 h, but bounced back at day 7 after MRT. Reprinted with permission from Yuan *et al. Radiation Research* 184, 322-333 (2015). 151

Figure 6.8 Apoptosis in normal mouse brain tissue after MRT. Reprinted with permission from Yuan *et al. Radiation Research* 184, 322-333 (2015). 151

Figure 6.9 Quantification of cell proliferation using Ki-67 immunohistological staining on the contralateral normal mouse brain tissue after MRT and BRT. A significantly higher number of proliferation cells were found in the MRT treated mice, but not in the BRT treated mice at 24h or 48h post-irradiation (* $P < 0.05$, compared to BRT). Reprinted with permission from Yuan *et al. Radiation Research* 184, 322-333 (2015). 152

Figure 6.10 F4/80 immunostaining on normal mouse brain tissue at 24 hours and 30 days after MRT. No positively stained macrophages or microglia cells were found at either time point. No other morphological brain tissue damage was detected. Reprinted with permission from Yuan *et al. Radiation Research* 184, 322-333 (2015). 153

Figure 6.11 Tumor progression monitored by MRI following different treatments. Tumor volume was shown as relative to the volume one day prior to treatment. Adapted from Zhang *et al. in Expert Review of Anticancer Therapy* 14 (12), 1411 – 1418 (2014) [4]. 154

Figure 7.1 Top row: design of concept of the second-generation compact MRT system with three CNT cathodes arrays. A specially designed oil cooling system is incorporated in this upgraded system to increase anode heat capacity and radiation output. Three microbeams with adjustable

width can be generated simultaneously. Bottom row: a photograph of the three-line cathode assembly is shown on left; on right shows a photograph of the vacuum chamber of the second-generation system..... 166

Figure 7.2 Schematic illustration of the CNT-based human MRT system in a circular design. Microbeam are generated from distributed CNT source arrays from multiple directions and directed towards the treatment target simultaneously. Each beam array contains multiple microbeams for which the beamwidth and lengths can be adjusted individually. Figures were not drawn to scale. Picture on the left is adapted from Zhang *et al. Expert Review of Anticancer Therapy* 14(12), 1411-1418 (2014) [2]..... 168

LIST OF ABBREVIATIONS

BNL	Brookhaven National Laboratory
BRIC	Biomedical Research Imaging Center
BRT	Broad-beam radiation treatment / Broad-beam radiation therapy
CLS	Canadian light source
CNT	Carbon nanotubes
COST	Cooperation in Science and Technology
CT	Computed tomography
CTV	Clinical target volume
C-T-C	Center-to-center
DNA	Deoxyribonucleic acid
DR	Dose rate
EBL	Electron beam lithography
ECG	Electrocardiogram
EPD	Electrophoretic deposition
ESRF	European Synchrotron Radiation Facility
FE	Field emission
FED	Field emission display
FNTD	Fluorescence nuclear track detector
FWHM	Full-width-at-half maximum
GBM	Glioblastoma multiforme
GJIC	Gap junction intercellular communication
HV	High voltage

HVL	Half value layer
ICS	Inverse Compton Scattering
IGMRT	Image-guided microbeam radiation therapy
IGRT	Image-guided radiation therapy
IMRT	Intensity-modulated radiation therapy
LINAC	Linear Accelerators
MRI	Magnetic resonance imaging
MRT	Microbeam radiation therapy
MST	Median survival time
MTF	Modulation Transfer Function
MWNT	Multi-walled carbon nanotube
NSLS	National Synchrotron Light Source
PASS	Patient Safety System
PDD	Percentage depth dose
PVDR	Peak-to-valley-dose-ratio
RGA	Residual gas analyzer
RIBE	Radiation-induced bystander effect
RT	Radiation therapy
s-DBT	Stationary digital breast tomosynthesis
s-DCT	Stationary digital chest tomosynthesis
s-IOT	Stationary intra-oral digital tomosynthesis
SEM	Standard error of the mean
SRS	Stereotactic radiosurgery

SRT	Stereotactic radiotherapy
SR	Synchrotron radiation
SS	Specific Surfaces
SWNT	Single-walled carbon nanotube
TMR	Tissue maximum ratio
TPL	Translational Pathology Lab
TPR	Tissue phantom ratio
TR	Transmission rate
UHV	Ultra-high vacuum

CHAPTER 1: INTRODUCTION

1.1 Radiotherapy for Cancer Management

The human body is a complicated ecosystem whose individual members are cells that are organized into collaborative assemblies of tissues. Its integrity and stability are synergetic effects of “regulatory systems” composed of hierarchical components, from the chromosome in an individual cell to the whole body immune regulations. Only certain types of cells have the capability of dividing and proliferating, and errors occur during these processes due to internal instability or environmental influences. Some of the errors are fatal to the cells, and some can be reinstated by the gene repair mechanisms. The failure of proper repair of deoxyribonucleic acid (DNA) damage often results in cell death in most cases and mutagenesis that could lead to innocuous cell survival. Very rarely malignancies occur if mutated cells escape the restraints of replicative senescence and the guard of the human immune system, and persist to divide, invade and colonize territories normally reserved for other cells (Figure 1.1). About 90% of human cancers are carcinomas, perhaps because most of the cell proliferation in the body occurs in epithelia, or because epithelial tissues are most frequently exposed to the external damages that stimulated the form of cancer [1].

Cancer is one of the most significant terminal diseases in the western world, exceeded only by heart diseases as the second leading cause of death. In the United States, almost one in every three people develops certain type of cancer in their lifetime, and one out of four people will die of cancer eventually [2]. The development of cancer is a microevolutionary process that

usually takes years. Clinical data have shown clearly that for most cancers the treatment outcome is significantly better when the cancers are diagnosed at earlier than late stages. The limited capability of available technologies today to detect early stage, small, in situ tumors is the main challenge in cancer management, and the main cause of the high mortality.

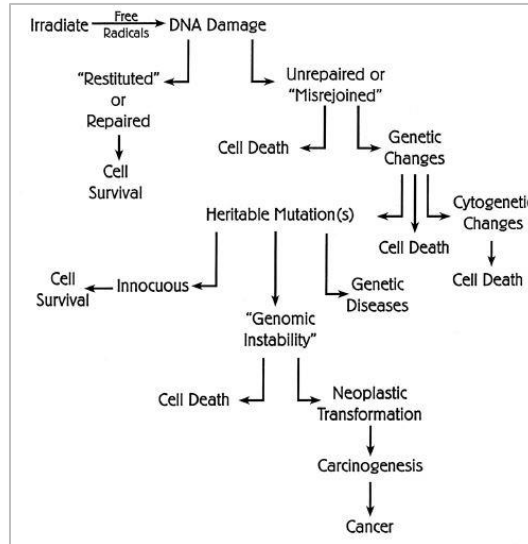


Figure 1.1 The radiation biology flow chart (Lecture handout for Radiation biology at UNC Chapel Hill. Reprinted with permission from Dr. Elaine Zeman, UNC Department of Radiation Oncology)

Radiation therapy (RT), or radiotherapy, is one of the most effective treatment modalities for cancer management together with surgical resection and chemotherapy. It uses ionizing radiation that damages the DNA in the cells through direct and indirect effects that may lead to cell death. RT demonstrates advantages in treating cancers located at eloquent sites that are physically not feasible for surgical removal, as well as in sterilizing remaining cancer cells after surgery. The sensitivity to radiation damage varies in different types of cells. To certain extend, normal tissue responds to radiation in a slightly different way compared to tumors. One of the main reasons is that tumors usually contain immature and less intact vasculature with a large amount of structural and functional abnormalities, and are therefore more sensitive to radiation

damage compared to those in the normal tissue. This opens up the therapeutic window in radiation therapy. However, the amount of the radiation dose and the treatment volume required for complete tumor cell sterilization often unavoidably lead to radiation dose to nearby normal structure that exceeds their tolerance, and hence increases the risk of severe normal tissue complications. Radiation-induced normal tissue complications remain as the major concern and a great challenge in RT. The risk of serious damage in normal tissue increases with radiation dose, as does the probability of local tumor control. The rapid rate of tumor regeneration and metastasis further complicates the treatment strategy. Improving the therapeutic ratio, i.e. maximizing the local or locoregional tumor control by permanently inactivating all cancer cells while minimizing the normal tissue damage, is the goal in radiotherapy [3]. In the last decade, new technologies in image guidance, treatment planning, as well as dose delivery have developed greatly and contributed substantially to the optimization in the clinical practice and treatment outcome of radiation therapy. One main way to improve the therapeutic efficacy is to achieve physical dose conformality in the clinical target volume (CTV) discerned by image guidance and decrease the volume of normal tissue irradiated and therefore the probability of normal tissue complications. In terms of external beam radiation therapy for instance, 3D conformal and intensity-modulated radiation therapy (IMRT) with the aid of computer-controlled dynamic multileaf collimators and treatment planning software has demonstrated significant advantage in delivering a high dose to the target volume and acceptably low dose to the surrounding normal structures. The advent of stereotactic radiosurgery (SRS) using X-rays or gamma rays, or stereotactic radiotherapy (SRT), is another advance for treating intracranial lesions. SRS is a single fraction radiotherapy procedure using a combination of a stereotactic apparatus and narrow multiple beams delivered through noncoplanar isocentric arcs. The same

procedure is called SRT if multiple dose fractions are delivered. A high degree of dose conformity is a hallmark of SRS, which is generally achieved by using appropriate circular beams to fit the lesion, optimizing arc angles and weights and using multiple isocenters or dynamically shaping the field during arc rotation with mini (or micro) multileaf collimators [4].

The effectiveness of tumor control using radiation therapy, as well as with other types of cancer treatments is not completely known yet. The treatment outcome is often largely dependent on various factors including the type of the cancer, the stage and progression, and the sites of the malignancies etc. Malignant brain cancer is one of the most aggressive cancers nowadays with minimum breakthrough made in terms of extending the patients lifespan using modern treatment technologies. The risk of losing major neurological functions often limits the extent and effect of surgical resection. Chemotherapy alone is often not effective for brain cancer management due to the blood-brain barrier which prevents a high dose uptake in the brain tumor. Radiation therapy plays an important role in the curative and palliative treatment of patients with primary and metastatic brain tumors. Existing SRS techniques including CyberKnife and Gamma Knife are able to achieve effective tumor control with minimum treatment toxicity for small lesions (<3 cm in diameter) at non-eloquent areas. The field size of gamma knife is limited to a maximum of 18 mm in diameter [4]. However, glioblastoma multiforme (GBM), the most common and malignant brain tumor, is highly aggressive and infiltrative in nature. These tumor cells are fast proliferating and tend to invade into the surrounding normal tissue, rendering a large and not well-defined lesion site surrounded by critical brain structures. The clinical target volume needs to be typically large in order to completely sterilize the primary tumor mass as well as the cancer cells that interdigitate with the surrounding normal brain tissue. For these reasons, severe radiation-induced side effects are difficult to avoid in GBM patients treated with existing RT

technologies, and tumor recurrence at the primary site happens in 90% of the cases [5]. The acute and late effects of RT on the brain are common and represent a significant source of morbidity. Primary brain cancer is also the second most prevalent cancer type in children, accounting for 22% of tumors in those < 18 years of age [6]. Radiation toxicity is even more of an issue for pediatric brain tumor patients as their developing central nervous system tissues can be more sensitive to chronic radiation damage. Over the last 50 years the survival extension has improved minimally for brain cancer patients. The median survival time in those with GBM is merely 15 months after diagnosis even when aggressive multi-modality treatments are applied [5, 7, 8].

1.2 Microbeam Radiation Therapy – Roots, Status, and Prospects

1.2.1 History and inspiration

Incidence of severe normal tissue complications is the major prohibitive factor from delivering sufficient radiation doses for effective tumor local control. The search for solutions to reduce RT-induced side effects and to achieve high dose in the CTV has been the ongoing task in the history of development and implementation of effective RT in cancer management. The first successful attempt was made by Dr. Alban Köhler in 1909 in Germany, by applying an iron grid with 1 mm thick wires and spaced 3.0 – 3.5 mm apart at the patient's skin when treating a large and deep-seated tumor using orthovoltage X-ray, the available radiation therapy technology at that time [9, 10]. This method allowed him to deliver a dose that was 10 – 20 times higher than typically tolerable with a seamless open field without inducing an incurable X-ray ulcer. Similar concept was employed by Dr. Liberson in the US later in 1933 by using a perforated lead sheet to prevent skin damage during the treatment of deep-seated lesions [11]. The grid was made of lead and rubber with equally spaced, 1cm circles cut into it presenting the entire treatment region with 50:50 open versus shielded areas. Both methods revealed the critical roles of the protected

normal cells that acted as the healing centers around the irradiated areas. This method was later recognized as spatially fractionated radiation therapy, or more commonly known as GRID therapy, and was routinely performed in orthovoltage beam RT in the 1950s to avoid prohibitive skin and subcutaneous tissue toxicity when treating deep-seated tumors [12, 13]. Nowadays, the advantage of GRID therapy has been largely overshadowed by the widely employed megavoltage beams RT with linear accelerators which achieve natural dose buildup underneath the skin entrance and deep penetration to reach internal tumors. GRID is mainly utilized as a palliative treatment for advanced bulky tumors using LINAC with new development in the grid design in recent years [14-16]. GRID therapy represents the very first successful clinical adaptation of the later formulated radiation dose-volume effect in the form of spatial-fractionation. The dose-volume effect describes the inverse relationship between the threshold of tolerable radiation dose in normal tissue and the irradiated macroscopic tissue volume [17]. As a common radiotherapeutic perception today, the radiation dose-volume effect is established based on accumulating preclinical and clinical experience, and has guided the development of modern radiotherapy in many ways [18, 19].

Microbeam radiation therapy [20] is also a spatially-fractionated radiotherapy modality that exploits the dose-volume effect at a microscopic scale. The concept was initially inspired by the studies led by Drs. Wolfgang Zeman and Howard J. Curtis at the Brookhaven National Laboratory (BNL) in the early 1960s to investigate the biological effect of heavy cosmic rays on astronauts in space primarily on brain tissue [21-24]. These pioneer experiments demonstrated the increased tolerance of mouse brain tissue to extremely high doses of microscopic radiation beams (Figure 1.2). Deuteron beams of 25 μm with dose of up to 4,000 Gy caused complete destruction of nerve cell bodies. However, the irradiated nerve fibers and interstitial glia cells

were largely preserved; neither was there permanent damage to the vessels. It was assumed then that the microscopic radiation beams only caused localized and predominantly direct injuries without much additional indirect effect such as interference with blood supply as seen in the broader beam irradiations. These encouraging findings correlated well with the macroscopic radiation dose-volume effect [17], but also led to the further exploration of using microbeam radiation for brain cancer treatment starting in the 1990s at both BNL National Synchrotron Light Source (NSLS) in Upton, New York and the European Synchrotron Radiation Facility (ESRF) in Grenoble, France [25-29].

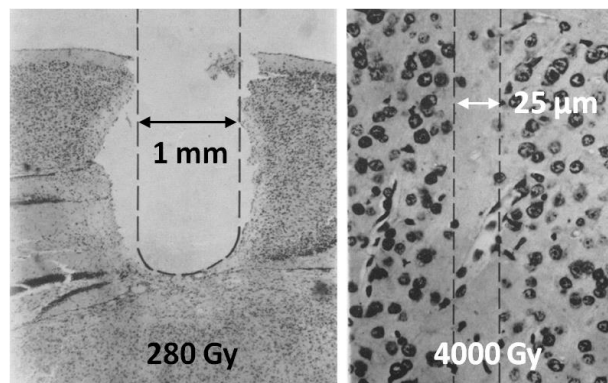


Figure 1.2 Histopathologic evidence of different radiobiological effects caused by microscopic versus millimeter-sized deuteron beam on the visual cortex of the mouse brain, which is a direct proof of the dose-volume effect. Adapted from Zeman W. et al., Radiation Research 15, 4 (1961)

As originally proposed, MRT refers to an experimental treatment technique which employs arrays of quasi-parallel, microscopically thin planar X-ray beams that are separated by a distance several times the beamwidth. Several features stand out in MRT compared to conventional external beam radiation therapy (or sometimes referred to as “broad beam” RT in this context). It uses orthovoltage radiation with the beamwidth ranging from 25 μm – 75 μm as in classic synchrotron MRT studies [25, 26, 28], to a few hundred microns as reported effective in recent experiments [30-34]. The microbeams create unique dose depositing profiles of

alternating peaks (high dose) regions and valleys (low dose) regions with a signature index named the peak-to-valley-dose-ratios, or PVDR [25, 29]. The total prescribed dose is usually delivered in a single fraction, either from one direction, or multiple ports around the target. The synchrotron generated microbeams are also featured by their ultra-high flux and minimal divergence. As shown in numerous preclinical studies using duck embryos, mice, rats and weanling piglets, MRT allows for administration of a single radiation dose that is two orders of magnitude higher than the total dose delivered in temporal fractionated RT from LINAC in the CTV without causing severe functional damage in normal tissue [26, 28, 35-47]. While existing RT technologies strive to achieve physically localized dose deposition for an optimal therapeutic ratio, MRT provides an alternative with the intrinsic differential radiobiological effects on tumor versus on normal brain tissue.

1.2.2 Synchrotron-based microbeam radiation therapy

1.2.2.1 Experimental characteristics

The original pilot experiments, as well as the majority of MRT preclinical studies in the last two decades were carried out at the NSLS and ESRF. Particularly, the ESRF Biomedical Beamline ID17 is currently the major beamline for MRT biological studies, veterinary trials and the clinical trials that are under preparation [48]. In recent years, increasing efforts have also been made in instrumentation upgrades and development to incorporate MRT studies at several other beamlines worldwide, including the Canadian Light Source (CLS) [49-52], the SPring-8 synchrotron radiation facility in Japan [53, 54], and the Australian Synchrotron facility [55]. As a powerful and valuable tool for a wide variety of research, synchrotron radiation differs dramatically in the beam generating mechanism. Inside a synchrotron facility, a group of charged particles (typically electrons) are circulating and accelerated into the relativistic regime in a

storage ring. The high-energy beam is then directed through strong magnetic fields generated by bending magnets or insertion devices (undulators or wigglers). The applied magnetic fields are perpendicular to the beam to deflect the beam trajectory and the synchrotron radiation is thus emitted at the bending points of the beam paths.

Compared to radiation generated through other mechanisms, synchrotron radiation demonstrates following properties [56]:

1. High intensity: the flux of synchrotron radiation is several orders of magnitude higher than that produced using conventional sources. Besides, the extremely high photon intensity is concentrated over a very small spatial and angular distribution, rendering an extreme beam brightness ($\text{photon} \cdot \text{s}^{-1} \cdot \text{mrad}^{-2} \cdot \text{mm}^{-2} \cdot (0.1\% \text{ bandwidth})^{-1}$);
2. Broad and continuous spectral range from far infrared ($<1 \text{ meV}$) to hard X-ray region (\sim hundreds of keV) with flexible energy modulation;
3. Natural narrow angular collimation: the emitted radiation beam is highly directional with minimal angular divergence;
4. High degree of polarization;
5. High beam stability.

The unique properties of SR present SR-based MRT with several characteristics. Firstly, the X-ray energy spectrum used in SR-based MRT is within the orthovoltage range. The treatment beam used at ESRF MRT is a filtered “white beam” (continuous spectrum from 50 – 350 keV) with a maximum intensity at 83 keV and a mean energy around 100 keV [25, 57]. Using orthovoltage radiation can largely preserve the sharp dose falloff and reduce the amount of scattered photons that would otherwise increase the energy deposition in the valley regions. The beam energy can also be tailored for imaging purposes [58]. Secondly, SR’s naturally low

divergence allows for generation of quasi-parallel ultra-thin microplanar beams using over a large range without redundant collimation. The radiation beam used for MRT experiments at ESRF Biomedical Beamline ID17, has a divergence of 1 mrad horizontally and 0.1 mrad vertically with a maximum dose rate of 16,000 Gy/s [59]. The typical microbeam width is 25 – 100 μm generated by the multislit collimator with little variation resulted from the beam divergence within the treatment volume. Kilovoltage photon energy with minimal beam divergence ensures a highly localized dose deposition in the microscopic scale, yielding a high PVDR and a small beam penumbra which are considered critical for achieving the biological advantages in MRT. The influence of beam divergence as well as polarization on the dose distribution in MRT has also been investigated and reported in detail by Dr. Heidi Nettelbeck et al., and Dr. Stefan Bartzsch et al. separately [60-62]. Besides, the large photon fluence and the resultant high dose rate essentially enable the delivery of high dose radiation within the shortest treatment time window. It could largely reduce the patient motion induced beam blurring and misfiring during the treatment, as well as discomforts of patients caused by long time treatment and immobilization.

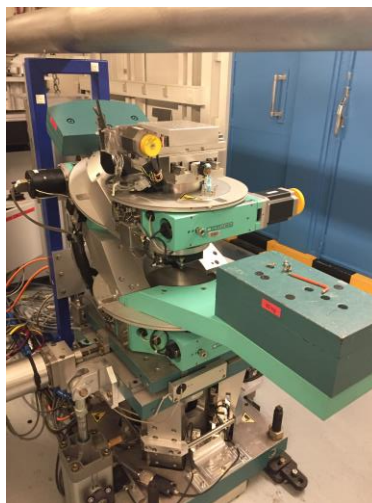


Figure 1.3 A photo of the sample positioning stage in the MRT experiment room at ESRF Biomedical Beamline ID17

In the implementation of synchrotron-based MRT preclinical studies as well as future clinical trials, substantial effort has been made in the past two decades through international collaboration of multiple research institutions and facilities. This includes, but not limited to, the design of multi-slit collimators [27, 63, 64], the development of positioning and patient safety system (PASS)[48, 65], developing new dosimeters, dosimetry and dosimeter calibration protocols [66], beam energy related simulations and optimizations [57, 67], image guidance protocols [58, 68], as well as the development of a dedicated treatment planning system [60, 69-71]. In May 2013, an European Union supported consortium of laboratories from 16 countries has launched within the European Cooperation in Science and Technology (COST) action TD1205 (SYRA3), which is dedicated to the Innovative Methods in Radiotherapy and Radiosurgery using Synchrotron Radiation to treat brain tumors and other diseases of the central nervous system [65]. The COST workgroup coordinates a multidisciplinary group of pioneers to address the challenges and solutions towards the clinical implementation of MRT. Veterinary trials were initiated in late 2013 and are ongoing at ESRF, with the aim to confirm the therapeutic efficacy and tissue responses in larger animals and further optimize the irradiation geometries and parameters prior to MRT human clinical trials [20, 72].

1.2.2.2 **Biological features**

Overview

Microbeam radiation therapy has the potential to outperform current external beam RT technologies with two main advantages identified in preclinical studies: 1) normal brain tissue and spinal cord have shown to tolerate peak MRT doses that are 100 times greater than those used in the conventional RT; 2) the entire tumor may be destroyed under MRT even though only a small portion of the entire volume is irradiated at peak doses. These extraordinary effects have

been confirmed in various synchrotron-based MRT studies using small animal models, including duck embryos [35], mice [36-38, 40], rats [26, 28, 41-45], and weanling piglets [46, 47] for histopathological response in normal tissue and tumors, tumor local control and survival investigations. Tumor types that have been investigated include 9L gliosarcoma (9LGS), C6 glioma and F98 glioma in rats, EMT-6 mammary carcinoma [36] and squamous cell carcinoma (SCCVII) [37] in mice. Various parameters that are considered directly related to the overall treatment outcome in MRT have been experimentally examined. These include beamwidth and center-to-center (c-t-c-) distance [37, 45, 73], peak and valley doses, and the PVDR, geometry of irradiation [31, 36, 74-77], spectrum and mean beam energy [25, 67, 78], effects of radiosensitizers [79-83].

Although there is accumulating preclinical evidence of high normal tissue tolerance and tumor ablation in MRT, the underlying biological mechanisms are yet to be revealed. It is believed that the additional biological mechanisms come into play when the spatial fractionation reaches microscopic scale other than the general dose-volume effect. MRT differs from conventional seamless beam RT in the way of spatial dose modulation with significantly increased areas of interface between irradiated and non-irradiated tissues. These specific surfaces (SS) are believed to play a key role in the mediation and repair of the heavily damaged tissue induced by the high dose irradiation [84]. Several effects related to the specific surfaces, including the bystander effect, the manifestations of microvasculature alteration and regeneration, have been hypothesized possibly responsible for parts of the biological responses induced by MRT. The systemic effects from the immune or endocrine systems have also been speculated to contribute to the preferential damage in tumor cells [85, 86]. However, none of these alone can be attributed to the overall biological responses. Substantial amount of systemic studies remain

to be carried out to elucidate the governing theory behind the therapeutic efficacy in MRT, which in turn would benefit the optimization of parameterized treatment planning and the eventual clinical use.

Bystander effects

The bystander effect is a widely discussed phenomenon in the field of gene therapy, toxicology and radiotherapy. It reflects the complex cell-to-cell communications through various pathways in order to govern their behavior for the benefit of the organism as a whole. Within the scope of radiation therapy, bystander effects refer to the presence of signal mediated effects induced by radiation in cells that are in the vicinity of the target volume and are exposed to only very low levels of scatter radiation, if any [87, 88]. These radiation induced signaling effects have been shown to be mediated through direct physical cell contact via gap junction intercellular communication (GJIC) [89, 90] or through the secretion of diffusible signaling molecules into the surrounding medium [91, 92]. Radiation-induced bystander effects (RIBEs) have been observed *in vitro* in a variety of cell lines and *in vivo* in rodent models exposed to both densely ionizing and sparsely ionizing radiations [93-95]. Dilmanian, et al. used a single microbeam that is 270 μm wide to irradiate the rats' spinal cords [96]. They hypothesized the involvement of a "beneficial" bystander effect in the repair process that led to the tissue restoration likely through the release of growth factors such as cytokines and the initiation of cell-signaling cascades. These cascades have possibly promoted angiogenesis to replace damaged capillary blood vessels, and proliferation, migration and differentiation of the progenitor glial cells to produce new, mature, and functional glial cells. The fact that certain types of signaling can coordinate decisions by groups of identical cells and different cells respond differently to the same type of extracellular signal molecules could explain part of the

different bystander responses observed in the normal tissue versus tumor cells that irradiated by high dose microbeams [1].

On the other hand, with the highly localized dose deposition as well as the ability of precise delivery of radiation microbeam radiation has also been a valuable tool in identification and analysis of the signaling factors that mediate the bystander effect [93, 97]. In the studies by Mothersill, et al., an inter-mammal bystander effect has been observed in the cage mates of rats irradiated by high doses of MRT [95]. Our evolving understanding towards the radiobiological responses in RIBE will certainly benefit the elucidation of the therapeutic mechanisms in MRT.

Vasculature responses

Blood vessels extend into the tissues to replenish nutrients, protein growth factors and oxygen and meanwhile carrying off waste products, in support of the normal functions and sometimes proliferations of the local organs. Besides, the immune responses as well as certain types of cell communication through secreted signaling molecules rely largely on the transportation via bloodstream. Fast proliferation in tumors induces angiogenesis with wide spread network of capillaries in response to the high demand of nutrients which thereafter promote further expansion and invasion of tumors into surrounding regions. Evidence however has pointed out the immaturity of tumor vasculatures with profound structural and functional abnormalities compared to the more intact and radioresistant vessels in normal tissue. This gives the chance of cancer cure by attacking the more vulnerable vessels to achieve tumor eradication. Indeed, the different microvasculatures and angiogenesis behaviors have been assumed largely responsible to the tissue specified responses to microbeam irradiation, as supported by accumulating numbers of small animal studies. The experiments by Bouchet, et al. showed for the first time that preferential damage of MRT to tumor vessels versus preservation of

radioresistant normal brain vessels contributes to the efficient palliation of 9L gliosarcomas in rats [98]. Sabatasso, et al. used chick chorioallantoic membrane model of an almost pure vascular system with immature vessels to study the microbeam effects and found out that MRT-induced vascular toxicity and physiological effects depend on the stage of capillary maturation [99].

Severe complications such as cerebral edema, hemorrhage, or necrosis that are typically associated with blood vessel damage were not observed in high dose microbeam irradiated normal tissues, indicating the high radioresistance of large mature vessels or the existence of rapid repair effects in damaged microvasculature [39, 43, 100]. Repopulation and migration of unirradiated cells from the valleys into the peak regions through the large area of interfaces (i.e. specific surface) were suggested to have facilitated the replacement of dead cells and the repair the highly damaged microvasculature [26]. A high level of vascular endothelial growth factor (VEGF) expression was also observed in the irradiated normal tissue, which could have contributed to the rapid repair of the destroyed microvessels and stimulated vascularization [98]. Therefore an adequate blood supply was maintained in microbeam irradiated normal tissue, whereas MRT induced tumor hypoxia in 9L gliosarcoma bearing rats [101-103].

Studies by van der Sanden, et al. have shown that microbeam peak doses under a certain range is able to reduce the clinical risks of long-delayed disruption or occlusion of non-targeted arteries from MRT compared to the corresponding risks from broad-beam radiosurgery [104].

Tumor vascular damage induced by high dose microbeams may provoke vascular normalization and may be exploited to improve tumor control using agents targeting angiogenesis [105].

1.2.3 Compact microbeam delivery systems – challenges and efforts

In the last half century, synchrotron light source has played a pioneering role in developing and advancing MRT research. The extremely high beam brilliance and low divergence provide unsurpassed dosimetric characteristics that are customizable for optimizing treatment parameters and probing into the radiobiologies. However, widely accessible, compact radiation sources are desired not only to promote the worldwide research to address the remaining technical and biological issues associated with the current state-of-the-art MRT, but also to expedite the ultimate clinical applications.

Spatial modulation in the microscopic range with high photon flux and steep dose gradient is the key to achieve therapeutic effect in MRT. Such dosimetric characteristics, however, are challenging to produce with conventional X-ray sources. Flux and collimation are the main problems with thermionic orthovoltage cathodes. Substantial collimation (small opening and high aspect ratio) has to be applied to the naturally divergent photon beam from the large and isotropic focal spot, in order to keep a small beam penumbra and a low valley dose. Therefore the overall efficiency in microbeam production is extremely low as the majority of x-ray photons are wasted as heat. Although micro-focused orthovoltage X-ray tubes are commercially available, they operate at much lower power and therefore cannot meet the required photon flux that is needed for treatment. Clinically employed LINAC uses megavoltage radiation that produces a large number of scattered, secondary charged particles. These high-energy charged particles leave a long-range of dose deposition outside the beam path and therefore smear out the microbeam patterns [106].

Currently, two types of new radiation sources are considered potential candidates for microbeam generation and delivery. The first one employs inverse Compton scattering (ICS) and

is currently being exploited by several groups around the world, including the French ThomX project [107-109], and the California based Lyncean Technologies Inc (Palo Alto, CA). The first generation ICS based irradiator developed by Lyncean has been installed at the Technische Universität München Institute for Medical Engineering (IMETUM) in Germany. Several limitations with the current ICS technologies exist, including relatively low photon flux and beam energy. The other radiation source being explored for compact MRT is the carbon nanotube (CNT) distributed source array technology [110, 111], which is the enabling X-ray technology for the work presented in this thesis. CNT distributed source array technology demonstrates numerous advantages over conventional X-ray tubes, and provides an attractive alternative and practical solution for generating the specific dosimetric characteristics in MRT in a laboratory-scale device.

1.3 **The Scope of This Work**

The development of a CNT-based compact MRT system is a continuing long-term effort that requires iterations of system optimization, large amount of systemic preclinical validations from various perspectives, and extensive multi-disciplinary collaborations. It has brought together the expertise of several research groups and pioneers since the beginning, and also inspired related new endeavors both at the University of North Carolina at Chapel Hill, and Duke University. As part the effort in developing a compact microbeam radiation therapy system using carbon nanotube distributed source array technology, my work conducted at the Applied Nanotechnology Lab that constitutes the bulk of this thesis mainly focused on the following two aspects:

- 1) To bridge the system design and biological studies by implementing image guidance for microbeam delivery.

- 2) To initiate the preclinical studies using the first-generation system with the aim to validate the system's therapeutic performance as a microbeam irradiator, as well as to investigate the radiobiological mechanisms in MRT using small animal models.

The first part includes hardware design, construction and conditioning, as well as establishing and validating methodologies and protocols regarding the detailed procedures to demonstrate targeted microbeam delivery in small animal models. These efforts are detailed in chapters 4 and 5.

Demonstrating the treatment efficacy with the specific dosimetric characteristics produced by the new system is the main topic of the second part. The work completed in this part has involved extensive collaborations with the UNC Biomedical Research Imaging Center (BRIC) and the kind support from the Translational Pathology Lab (TPL) at UNC Lineberger Comprehensive Cancer Center. Tumor local control, survival time and histopathological analysis have been performed with the aid of several techniques and facilities. This is detailed in chapter 6.

Feasibility of multi-array microbeam delivery to enhance dose deposition in tumor with the CNT-based MRT system has also been explored. Chapters 5 and 6 covered the methodology development, dedicated hardware upgrade, image guidance protocols as well as comparative studies of treatment outcome tested in U87MG bearing mice.

A brief introduction of MRT from the historical, experimental and biological perspectives is presented in Chapter 1. Carbon nanotube distributed source array technology and applications in medical imaging and therapy are reviewed in Chapter 2. Chapter 3 discusses the current status of the system development, system characterization, and several issues and corresponding

remedies identified during the course of my thesis project over the past 5 years using the first-generation prototype.

Finally, the concluding chapter presents the summaries of this work, and some prospective discussion.

REFERENCES

1. Alberts, B., J. Lewis, and D. Bray, *Molecular biology of the cell*. 2000: Garland Science.
2. *United States Cancer Statistics, Centers for Disease Control and Prevention*. Available from: <https://nccd.cdc.gov/uscs/>.
3. Holthusen, H., *Erfahrungen über die Verträglichkeitsgrenze für Röntgenstrahlen und deren Nutzenanwendung zur Verhütung von Schäden*. *Strahlentherapie*, 1936. **57**: p. 254-269.
4. Khan, F.M., *The physics of radiation therapy*. 2010: Lippincott Williams & Wilkins.
5. Jovčevska, I., N. Kočevar, and R. Komel, *Glioma and glioblastoma-how much do we (not) know?* *Molecular and clinical oncology*, 2013. **1**(6): p. 935-941.
6. Lawrence, Y.R., et al., *Radiation dose-volume effects in the brain*. *Int J Radiat Oncol Biol Phys*, 2010. **76**(3 Suppl): p. S20-7.
7. Stewart, L.A., *Chemotherapy in adult high-grade glioma: a systematic review and meta-analysis of individual patient data from 12 randomised trials*. *Lancet*, 2002. **359**: p. 1011-1018.
8. Huse, J.T. and E.C. Holland, *Targeting brain cancer: advances in the molecular pathology of malignant glioma and medulloblastoma*. *Nature reviews cancer*, 2010. **10**(5): p. 319-331.
9. Köhler, A., *Röntgentiefentherapie mit Metallnetzschutz*. *Strahlentherapie*, 1912. **1**: p. 121-131.
10. Laissue, J.A., H. Blattmann, and D.N. Slatkin, *Alban Kohler (1874-1947): Inventor of grid therapy*. *Z Med Phys*, 2012. **22**(2): p. 90-9.
11. Liberson, F., *The Value of a Multi-perforated Screen in Deep X-ray Therapy: A Preliminary Report on a New Method of Delivering Multiple Erythema Doses without Permanent Injury to the Skin*. *Radiology*, 1933. **20**(3): p. 186-195.
12. Marks, H., *A New Approach to the Roentgen Therapy of Cancer with the Use of a Grid (Preliminary Report)*. *J. Mt. Sinai Hosp. NY*, 1950. **17**.
13. Marks, H., *Clinical Experience with Irradiation Through a Grid I*. *Radiology*, 1952. **58**(3): p. 338-342.
14. Mohiuddin, M., et al., *High-dose spatially-fractionated radiation (GRID): a new paradigm in the management of advanced cancers*. *Int J Radiat Oncol Biol Phys*, 1999. **45**(3): p. 721-7.
15. Buckey, C., et al., *Evaluation of a commercially-available block for spatially fractionated radiation therapy*. *J Appl Clin Med Phys*, 2010. **11**(3): p. 3163.

16. Mohiuddin, M. and H. Park. *Spatially Fractionated GRID radiation therapy (SFGRT) using a brass collimator*. in *American Association of Medical Dosimetrists*. 2013.
17. Rodney, W., J.M.G. Taylor, and B. Maciejewski, *Treatment volume and tissue tolerance*. *International Journal of Radiation Oncology*Biology*Physics*, 1988. **14**(4): p. 751-759.
18. Emami, B., et al., *Tolerance of normal tissue to therapeutic irradiation*. *International Journal of Radiation Oncology*Biology*Physics*, 1991. **21**(1): p. 109-122.
19. Hopewell, J.W. and K.-R. Trott, *Volume effects in radiobiology as applied to radiotherapy*. *Radiotherapy and Oncology*, 2000. **56**(3): p. 283-288.
20. Brauer-Krisch, E. and R.S.o.b.o.t.s.c.t.c.t.i. MRT. *The minipig experiment: a last major milestone prior clinical trials in MRT [unpublished results]*. in *Medical Applications of Synchrotron Radiation 2015*. 2015. Grenoble & Villard de Lans, France.
21. Zeman, W., et al., *Tolerance of mouse-brain tissue to high-energy deuterons*. *Science*, 1959. **130**(3391): p. 1760-1.
22. Zeman, W., H.J. Curtis, and C.P. Baker, *Histopathologic effect of high-energy-particle microbeams on the visual cortex of the mouse brain*. *Radiat. Res.*, 1961. **15**(4): p. 496-514.
23. Baker, C.P., et al., *The design and calibration of a deuteron microbeam for biological studies*. *Radiat Res*, 1961. **15**(4): p. 489-95.
24. Curtis, H.J., *The Use of a Deuteron Microbeam for Simulating the Biological Effects of Heavy Cosmic-Ray Particles*. *Radiat. Res. Suppl.*, 1967. **7**: p. 250-257.
25. Slatkin, D.N., et al., *Microbeam radiation therapy*. *Med. Phys.*, 1992. **19**(6): p. 1395-400.
26. Slatkin, D.N., et al., *Subacute neuropathological effects of microplanar beams of x-rays from a synchrotron wiggler*. *Proc. Natl. Acad. Sci. USA*, 1995. **92**(19): p. 8783-7.
27. Slatkin, D.N., et al., *Design of a Multislit, Variable Width Collimator for Microplanar Beam Radiotherapy*. *Review of Scientific Instruments*, 1995. **66**(2): p. 1459-1460.
28. Laissue, J.A., et al., *Neuropathology of ablation of rat gliosarcomas and contiguous brain tissues using a microplanar beam of synchrotron-wiggler-generated X rays*. *Int. J. Cancer*, 1998. **78**(5): p. 654-660.
29. Laissue, J.A., et al. *Microbeam radiation therapy*. in *SPIE*. 1999. Denver, CO USA.
30. Dilmanian, F.A., et al., *X-ray microbeams: Tumor therapy and central nervous system research*. *Nucl. Instrum. Methods Phys. Res. A*, 2005. **548**(1-2): p. 30-37.
31. Dilmanian, F.A., et al., *Interlaced x-ray microplanar beams: a radiosurgery approach with clinical potential*. *Proc. Natl. Acad. Sci. USA*, 2006. **103**(25): p. 9709-14.

32. Anshel, D.J., et al., *Evolution of a focal brain lesion produced by interlaced microplanar X-rays*. Minim Invasive Neurosurg, 2007. **50**(1): p. 43-6.
33. Dilmanian, F.A., et al., *X-Ray Microbeam Irradiation of the Contusion-Injured Rat Spinal Cord Temporarily Improves Hind-Limb Function*. Radiation Research, 2013. **179**(1): p. 76-88.
34. Prezado, Y., et al., *Increase of lifespan for glioma-bearing rats by using minibeam radiation therapy*. J. Synchrotron Radiat., 2012. **19**(Pt 1): p. 60-5.
35. Dilmanian, F.A., et al., *Response of avian embryonic brain to spatially segmented x-ray microbeams*. Cell Mol Biol (Noisy-le-grand), 2001. **47**(3): p. 485-93.
36. Dilmanian, F.A., et al., *Murine EMT-6 carcinoma: high therapeutic efficacy of microbeam radiation therapy*. Radiat. Res., 2003. **159**(5): p. 632-41.
37. Miura, M., et al., *Radiosurgical palliation of aggressive murine SCCVII squamous cell carcinomas using synchrotron-generated X-ray microbeams*. Br. J. Radiol., 2006. **79**(937): p. 71-5.
38. Serduc, R., et al., *In vivo two-photon microscopy study of short-term effects of microbeam irradiation on normal mouse brain microvasculature*. Int. J. Radiat. Oncol. Biol. Phys., 2006. **64**(5): p. 1519-27.
39. Serduc, R., et al., *Brain tumor vessel response to synchrotron microbeam radiation therapy: a short-term in vivo study*. Phys. Med. Biol., 2008. **53**(13): p. 3609-22.
40. Serduc, R., et al., *Characterization and quantification of cerebral edema induced by synchrotron x-ray microbeam radiation therapy*. Phys. Med. Biol., 2008. **53**(5): p. 1153-66.
41. Laissue, J.A., et al., *Response of the rat spinal cord to X-ray microbeams*. Radiother. Oncol., 2013. **106**(1): p. 106-11.
42. Dilmanian, F.A., et al., *Response of rat intracranial 9L gliosarcoma to microbeam radiation therapy*. Neuro. Oncol., 2002. **4**(1): p. 26-38.
43. Zhong, N., et al., *Response of rat skin to high-dose unidirectional x-ray microbeams: a histological study*. Radiat. Res., 2003. **160**(2): p. 133-42.
44. Smilowitz, H.M., et al., *Synergy of gene-mediated immunoprophylaxis and microbeam radiation therapy for advanced intracerebral rat 9L gliosarcomas*. J. Neuro-Oncology, 2006. **78**(2): p. 135-43.
45. Regnard, P., et al., *Irradiation of intracerebral 9L gliosarcoma by a single array of microplanar x-ray beams from a synchrotron: balance between curing and sparing*. Phys. Med. Biol., 2008. **53**(4): p. 861-878.

46. Laissue, J.A., et al. *Weanling piglet cerebellum: a surrogate for tolerance to MRT (microbeam radiation therapy) in pediatric neuro-oncology.* in *SPIE*. 2001. San Diego, CA USA.
47. Laissue, J.A., et al., *Prospects for microbeam radiation therapy of brain tumours in children to reduce neurological sequelae.* *Dev. Med. Child. Neurol.*, 2007. **49**(8): p. 577-81.
48. Requardt, H., et al., *The Clinical Trials Program at the ESRF Biomedical Beamline ID17: Status and Remaining Steps.* *AIP Conference Proceedings*, 2010. **1234**(1): p. 161-164.
49. Chapman, D., *Biomedical imaging and therapy beamline preliminary design report.* CLSI Document, 2006(26.2): p. 1.2.
50. Wysokinski, T.W., et al., *Beamlines of the biomedical imaging and therapy facility at the Canadian light source—Part 1.* *Nuclear Instruments and Methods in Physics Research Section A: Accelerators, Spectrometers, Detectors and Associated Equipment*, 2007. **582**(1): p. 73-76.
51. Wysokinski, T.W., et al., *Beamlines of the Biomedical Imaging and Therapy Facility at the Canadian Light Source - Part 2.* *Journal of Physics: Conference Series*, 2013. **425**(7): p. 072013.
52. Wysokinski, T.W., et al., *Beamlines of the biomedical imaging and therapy facility at the Canadian light source - part 3.* *Nuclear Instruments & Methods in Physics Research Section a-Accelerators Spectrometers Detectors and Associated Equipment*, 2015. **775**: p. 1-4.
53. *SPring-8* http://www.spring8.or.jp/wkg/BL28B2/instrument/lang-en/INS-0000000374/instrument_summary_view.
54. Torikoshi, M., et al., *Dosimetry for a microbeam array generated by synchrotron radiation at SPring-8.* *Eur. J. Radiol.*, 2008. **68**(3 Suppl): p. S114-7.
55. Lewis, R.A., *Medical applications of synchrotron radiation in Australia.* *Nuclear Instruments and Methods in Physics Research Section A: Accelerators, Spectrometers, Detectors and Associated Equipment*, 2005. **548**(1–2): p. 23-29.
56. Mobilio, S., F. Boscherini, and C. Meneghini, *Synchrotron Radiation: Basics, Methods and Applications.* 2014: Springer.
57. Siegbahn, E.A., et al., *Determination of dosimetrical quantities used in microbeam radiation therapy (MRT) with Monte Carlo simulations.* *Medical Physics*, 2006. **33**(9): p. 3248-3259.
58. Serduc, R., et al., *In vivo pink-beam imaging and fast alignment procedure for rat brain lesion microbeam radiation therapy.* *J. Synchrotron Radiat.*, 2010. **17**(3): p. 325-31.

59. Bräuer-Krisch, E., et al., *The preclinical set-up at the ID17 biomedical beamline to achieve high local dose deposition using interlaced microbeams*. Journal of Physics: Conference Series, 2013. **425**(2): p. 022001.
60. Bartzsch, S., *Microbeam Radiation Therapy - Physical and biological aspects of a new cancer therapy and development of a treatment planning system*, in Institute of Physics. 2014, University of Heidelberg
61. Bartzsch, S., et al., *Influence of polarization and a source model for dose calculation in MRT*. Medical Physics, 2014. **41**(4): p. -.
62. Nettelbeck, H., et al., *Microbeam radiation therapy: a Monte Carlo study of the influence of the source, multislit collimator, and beam divergence on microbeams*. Med Phys, 2009. **36**(2): p. 447-56.
63. Archer, D.W., *Collimator for producing an array of microbeams*. 1998, Google Patents.
64. Brauer-Krisch, E., et al., *New technology enables high precision multislit collimators for microbeam radiation therapy*. Rev Sci Instrum, 2009. **80**(7): p. 074301.
65. Bravin, A., et al., *SYRA3 COST Action--Microbeam radiation therapy: Roots and prospects*. Phys Med, 2015. **31**(6): p. 561-3.
66. Brauer-Krisch, E., et al., *Medical physics aspects of the synchrotron radiation therapies: Microbeam radiation therapy (MRT) and synchrotron stereotactic radiotherapy (SSRT)*. Phys Med, 2015. **31**(6): p. 568-83.
67. Crosbie, J.C., et al., *Energy spectra considerations for synchrotron radiotherapy trials on the ID17 bio-medical beamline at the European Synchrotron Radiation Facility*. J Synchrotron Radiat, 2015. **22**(4): p. 1035-41.
68. Umetani, K. and T. Kondoh. *Phase contrast portal imaging for image-guided microbeam radiation therapy*. in SPIE. 2014.
69. Martinez-Rovira, I., J. Sempau, and Y. Prezado, *Monte Carlo-based treatment planning system calculation engine for microbeam radiation therapy*. Med. Phys., 2012. **39**(5): p. 2829-38.
70. Martinez-Rovira, I., J. Sempau, and Y. Prezado, *Development and commissioning of a Monte Carlo photon beam model for the forthcoming clinical trials in microbeam radiation therapy*. Med Phys, 2012. **39**(1): p. 119-31.
71. Bartzsch, S. and U. Oelfke, *A new concept of pencil beam dose calculation for 40-200 keV photons using analytical dose kernels*. Medical Physics, 2013. **40**(11): p. 111714.
72. Laissue, J.A., et al. *MRT for pet animals: normal organ tolerance of the rabbit nose and jaws; preliminary data [unpublished results]*. in Medical Applications of Synchrotron Radiation 2015. 2015. Grenoble & Villard de Lans, France.

73. Serduc, R., et al., *Synchrotron microbeam radiation therapy for rat brain tumor palliation—influence of the microbeam width at constant valley dose*. *Phys. Med. Biol.*, 2009. **54**(21): p. 6711.
74. Bräuer-Krisch, E., et al., *New irradiation geometry for microbeam radiation therapy*. *Phys. Med. Biol.*, 2005. **50**(13): p. 3103-11.
75. Dilmanian, F.A., G.M. Morris, and J.F. Hainfeld, *Methods for implementing microbeam radiation therapy*. 2007, Google Patents: US.
76. Serduc, R., et al., *First trial of spatial and temporal fractionations of the delivered dose using synchrotron microbeam radiation therapy*. *J. Synchrotron Radiat.*, 2009. **16**(Pt 4): p. 587-90.
77. Serduc, R., et al., *High-precision radiosurgical dose delivery by interlaced microbeam arrays of high-flux low-energy synchrotron X-rays*. *PLoS one*, 2010. **5**(2): p. e9028.
78. Shinohara, K., et al., *Optimization of X-ray microplanar beam radiation therapy for deep-seated tumors by a simulation study*. *Journal of X-Ray Science and Technology*, 2014. **22**(3): p. 395-406.
79. Le Duc, G.r., et al., *Toward an image-guided microbeam radiation therapy using gadolinium-based nanoparticles*. *Acs Nano*, 2011. **5**(12): p. 9566-9574.
80. Régnard, P., et al., *Enhancement of survival of 9L gliosarcoma bearing rats following intracerebral delivery of drugs in combination with microbeam radiation therapy*. *European journal of radiology*, 2008. **68**(3): p. S151-S155.
81. Prezado, Y., et al., *Gadolinium dose enhancement studies in microbeam radiation therapy*. *Med Phys*, 2009. **36**(8): p. 3568-74.
82. Alric, C., et al., *Gold nanoparticles designed for combining dual modality imaging and radiotherapy*. *Gold Bulletin*, 2008. **41**(2): p. 90-97.
83. Rahman, W.N., et al., *Influence of gold nanoparticles on radiation dose enhancement and cellular migration in microbeam-irradiated cells*. *BioNanoScience*, 2011. **1**(1-2): p. 4-13.
84. Brauer-Krisch, E., et al., *Effects of pulsed, spatially fractionated, microscopic synchrotron X-ray beams on normal and tumoral brain tissue*. *Mutat. Res.*, 2010. **704**(1-3): p. 160-6.
85. Bouchet, A., et al., *Early gene expression analysis in 9L orthotopic tumor-bearing rats identifies immune modulation in molecular response to synchrotron microbeam radiation therapy*. *PloS one*, 2013. **8**(12): p. e81874.
86. Sprung, C.N., et al., *Genome-wide transcription responses to synchrotron microbeam radiotherapy*. *Radiat. Res.*, 2012. **178**(4): p. 249-59.

87. Snyder, A.R., *Review of radiation-induced bystander effects*. Hum Exp Toxicol, 2004. **23**(2): p. 87-9.
88. Blyth, B.J. and P.J. Sykes, *Radiation-Induced Bystander Effects: What Are They, and How Relevant Are They to Human Radiation Exposures?* Radiation Research, 2011. **176**(2): p. 139-157.
89. Azzam, E.I., S.M. de Toledo, and J.B. Little, *Direct evidence for the participation of gap junction-mediated intercellular communication in the transmission of damage signals from alpha -particle irradiated to nonirradiated cells*. Proc Natl Acad Sci U S A, 2001. **98**(2): p. 473-8.
90. Azzam, E.I. and J.B. Little, *The radiation-induced bystander effect: evidence and significance*. Human & experimental toxicology, 2004. **23**(2): p. 61-65.
91. Mothersill, C. and C.B. Seymour, *Cell-Cell Contact during Gamma Irradiation Is Not Required to Induce a Bystander Effect in Normal Human Keratinocytes: Evidence for Release during Irradiation of a Signal Controlling Survival into the Medium*. Radiation Research, 1998. **149**(3): p. 256.
92. Asur, R., et al., *High dose bystander effects in spatially fractionated radiation therapy*. Cancer Lett, 2015. **356**(1): p. 52-7.
93. Mothersill, C. and C. Seymour, *Radiation-induced bystander effects: past history and future directions*. Radiat Res, 2001. **155**(6): p. 759-67.
94. Fernandez-Palomo, C., et al., *Bystander effects in tumor-free and tumor-bearing rat brains following irradiation by synchrotron X-rays*. Int. J. Radiat. Biol., 2013. **89**(6): p. 445-53.
95. Mothersill, C., et al., *Transmission of Signals from Rats Receiving High Doses of Microbeam Radiation to Cage Mates: An Inter-Mammal Bystander Effect*. Dose-Response, 2013. **1**(1): p. 1-21.
96. Dilmanian, F.A., et al., *Tissue-sparing effect of x-ray microplanar beams particularly in the CNS: is a bystander effect involved?* Exp. Hematol., 2007. **35**(4 Suppl 1): p. 69-77.
97. Prise, K.M., et al., *Microbeam studies of the bystander response*. Journal of radiation research, 2009. **50**(Suppl A): p. A1-A6.
98. Bouchet, A., et al., *Preferential effect of synchrotron microbeam radiation therapy on intracerebral 9L gliosarcoma vascular networks*. Int. J. Radiat. Oncol. Biol. Phys., 2010. **78**(5): p. 1503-12.
99. Sabatasso, S., et al., *Microbeam radiation-induced tissue damage depends on the stage of vascular maturation*. Int J Radiat Oncol Biol Phys, 2011. **80**(5): p. 1522-32.

100. Blattmann, H., et al., *Applications of synchrotron X-rays to radiotherapy*. Nucl. Instrum. Methods Phys. Res. A, 2005. **548**(1-2): p. 17-22.
101. Bouchet, A., et al., *Synchrotron microbeam radiation therapy induces hypoxia in intracerebral gliosarcoma but not in the normal brain*. Radiother. Oncol., 2013. **108**(1): p. 143-8.
102. Bouchet, A., et al., *Effects of microbeam radiation therapy on normal and tumoral blood vessels*. Phys Med, 2015(0).
103. Bouchet, A., et al., *Identification of AREG and PLK1 pathway modulation as a potential key of the response of intracranial 9L tumor to microbeam radiation therapy*. Int J Cancer, 2015. **136**(11): p. 2705-16.
104. van der Sanden, B., et al., *Tolerance of arteries to microplanar X-ray beams*. Int J Radiat Oncol Biol Phys, 2010. **77**(5): p. 1545-52.
105. Griffin, R.J., et al., *Microbeam radiation therapy alters vascular architecture and tumor oxygenation and is enhanced by a galectin-1 targeted anti-angiogenic peptide*. Radiat Res, 2012. **177**(6): p. 804-12.
106. Gokeri, G., et al., *Monte Carlo simulation of stereotactic microbeam radiation therapy: evaluation of the usage of a linear accelerator as the x-ray source*. Phys Med Biol, 2013. **58**(13): p. 4621-42.
107. Variola, A. *The ThomX Project*. in *International Particle Accelerator Conference*. 2011. Spain.
108. Variola, A., et al., *The ThomX project status*, in *5th International Particle Accelerator Conference IPAC*. 2014: Dresden, Germany.
109. Jacquet, M. and P. Suortti, *Radiation therapy at compact Compton sources*. Phys Med, 2015.
110. Zhou, O.Z. and J. Lu, *X-ray generating mechanism using electron field emission cathode*. 2003, The University of North Carolina at Chapel Hill: U. S.
111. Zhou, O.Z. and S.X. Chang, *Compact microbeam radiation therapy systems and methods for cancer treatment and research*. 2010, A61N 5/10; A61B 6/03; A61B 6/00: U.S.

CHAPTER 2: CARBON NANOTUBE FIELD EMISSION SOURCE ARRAYS

2.1 Overview

Carbon nanotube is a relatively new member of the large family of carbon allotropes. It is generally believed to be experimentally observed and structurally characterized in 1991 for the first time, not long after the discovery of fullerenes, by Dr. Iijima [1] although the true identity of the discoverers of CNTs remains somewhat controversial. Since this pioneering work, the worldwide study of carbon nanotubes in terms of their synthesis, properties, and applications in various fields has progressed rapidly.

This chapter reviews the fundamentals of carbon nanotubes from material science perspectives, the CNT field emission source array technology, and its recent applications and advancement in medical devices including diagnostic imaging and radiotherapy systems.

2.2 Structures and Physical Properties of Carbon Nanotubes

Structurally, a carbon nanotube can be described as a honeycomb lattice (one or multiple sheets of graphene) seamlessly rolled into a cylindrical shape, with one or both ends capped with a fullerene hemisphere. On each graphene layer along the cylindrical section, carbon atoms are arranged in repeating hexagonal units. Each cap, on the other hand, contains six pentagons and an appropriate number and location of hexagons that are selected to fit perfectly to the long cylindrical tube body [2]. Depending on the number of graphene sheets they consist of, CNTs are often named as single-walled carbon nanotube (SWNT), or multi-walled carbon nanotube (MWNT) with an average inlayer spacing of 0.344 nm [3]. The diameter of a carbon nanotube is

of nanometer size, ranging from less than 1.0 nm to 50.0 nm, depending on the number of walls composing the nanotubes. For example, a SWNT usually has a diameter of 0.7 – 10.0 nm, although most of the observed SWNTs have diameters < 2 nm [2]. The length of the tube can be more than 10 μm or even longer [3], resulting in a large length-to-diameter aspect ratio in the order of 10^4 - 10^5 or more. Single-walled CNTs are the sharpest inorganic structures found in nature so far [4].

The structure of a carbon nanotube is specified by the chiral vector, which describes the orientation of the repeating hexagonal unit on each layer relative to the axis of the nanotube as well as the diameter of the nanotube. The chiral vector thus classifies the symmetry of a carbon nanotube being either achiral (symmorphic) or chiral (non-symmorphic). An achiral carbon nanotube is the one whose mirror image has an identical structure to the original one, whereas a chiral nanotube exhibits a spiral symmetry whose mirror image cannot be superimposed on to the original one. There are only two cases of achiral nanotubes, namely armchair and zigzag nanotubes. The names of armchair and zigzag characterize the shape of the cross-section of the edge of the cut nanotubes.

Therefore, the full geometry of a carbon nanotube can be described mainly by its diameter, chirality, cap structures, and number of layers. Carbon nanotubes demonstrate a variety of unique physical properties (thermally, electrically, mechanically, etc.) due to the uniqueness in their structures. Notably, a CNT can be either metallic or semiconducting, depending on its chirality, which changes subtly their electronic structures, and therefore the electrical conductivity, as shown in Figure 2.1. Furthermore, the energy gap of semiconducting carbon nanotubes can be varied continuously from 1 eV to 0 eV, by varying the diameter [2]. Some of the main physical properties of carbon nanotubes are summarized in Table 2.1.

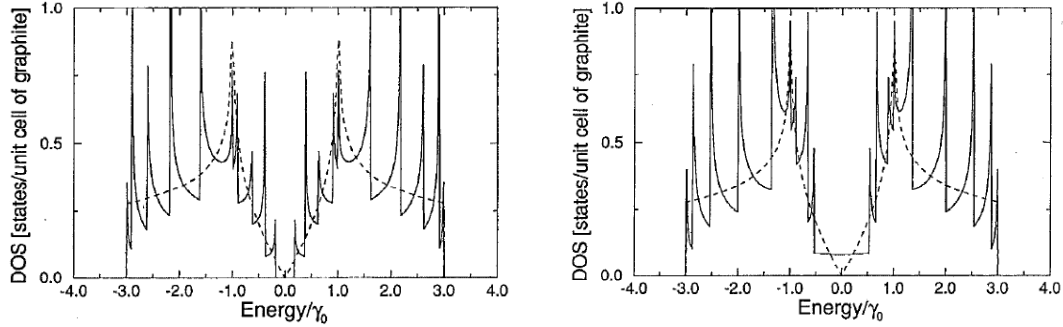


Figure 2.1 Electronic density of states for two zigzag carbon nanotubes, a metallic (9, 0) one on the left, and a semiconducting (10, 0) one on the right. Reprinted from Saito et al. *Applied Physics Letters* **60**(18), 1992 [5]

Table 2.1 Selected physical properties of carbon nanotubes [3, 6]

Attribute	Comments
Metallic to semiconductor electrical conductivity, depending on microstructure	No other known molecule has this property
Electrical conductivity: $10^8 \Omega^{-1} \text{m}^{-1}$	Comparable to that of copper
Thermal conductivity: $10^4 \text{W m}^{-1} \text{K}^{-1}$	> that of diamond, the highest thermal conductivity near room temperature
Carrier mobility: $10^4 \text{cm}^2 \text{V}^{-1} \text{s}^{-1}$	> That of GaAs
Withstands a current density up to 10^9A cm^{-1}	Due to very weak electromigration
Young's modulus of the order of 1 TPa	Stiffest material so far
Tensile strength: 150 GPa	600 times the strength/weight ratio of steel

2.3 Field Emission from Carbon Nanotubes

2.3.1 Fundamentals of field emission theory

Electron field emission (FE) is a well-known quantum-mechanical effect [7]. Briefly, it describes the phenomenon of extraction of electrons from the surface of condensed matter (solid or liquid) into vacuum under an intense static electric field. As illustrated in Figure 2.2, the combined effect of image force potential and the strong external electric field narrows the effective potential barrier of electrons at the surface of the condensed matter (e.g. metal) into a rounded triangle shape, so that electrons around the Fermi level would have a significant probability to escape from the surface to the vacuum level through the quantum tunneling effect.

The stronger the external electric field, the narrower the energy barrier is. The emission coefficient and current are mainly determined by the strength of the electric field and the type of material, and have been quantified by Fowler – Nordheim theory [8-10].

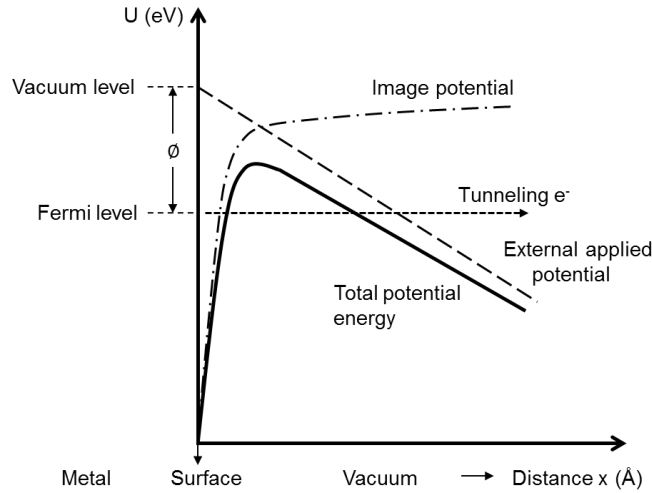


Figure 2.2 A schematic illustration of the potential energy of electron $U(x)$ (in eV) as a function of the distance x from the metal surface in an external static electric field. The effective energy barrier is sufficiently narrowed that the electrons could tunnel through. Horizontal dotted line illustrates the energy barrier width for electrons at Fermi level to tunnel through.

The Fowler-Nordheim equation [11-13] is as follows :

$$I = aV^2 \exp\left(-\frac{b\phi^{3/2}}{\beta V}\right)$$

where a and b are constants, I is the emission current, V is the applied voltage, ϕ is the work function of the material, and β is the field emission enhancement factor. The work function ranges from 2-5 eV for metals, and depends strongly on the surface crystallographic structures [14]. Detectable field emission starts at extremely high local electric field about $10^7 - 10^8$ V/cm. In order to achieve such high local fields at the metal surface using attainable potential, a geometrically sharp emitting tip/protrusion with the apex radius of curvature ranging from tens

of angstroms to several microns is practically favorable, producing a largely intensified local electrical field at the tip end that is much higher than the macroscopic applied field [15]. This geometrical effect at the surface is characterized by the factor β in the equation namely the field enhancement factor, i.e. the ratio between the local and applied electric fields. The larger the β is, the higher the field strength enhanced at the surface, and therefore the lower the effective threshold voltage requires to apply for emission [16]. For an isolated tip shaped as a hemisphere-on-orthogonal cone, β is well approximated by $1/(5r)$ where r is the radius of curvature of the tip [17].

Commonly used field emitters include sharp metals tips (mainly tungsten and molybdenum), silicon, diamond, graphite, and more recently nanostructures especially carbon nanotubes which will be discussed in section 3.3.2. [15].

Field emission is an alternative to classical thermionic emission for electron generation, with numerous advantages including (but not limited to) [15, 18]:

- a) No heating required in the FE process, i.e. “cold cathode” (although FE are combined with thermionic emission in some circumstances);
- b) High steady-state FE current density (approaching $10^5 - 10^6$ A/cm²);
- c) Small electron energy spread;
- d) A high beam coherence due to the narrow energy spread and the use of small (atomic dimension) emission areas;
- e) Sub-millisecond response to electric field variation;
- f) Resistance to temperature fluctuations;
- g) Small source dimensions (compared to thermionic cathodes);
- h) Longer service life (compared to thermionic cathodes);

Field emission sources do generally require relatively higher vacuum level compared to thermionic electron sources (10^{-9} - 10^{-10} torr for FE versus as low as 10^{-5} torr for thermionic filament) [15]. Field emission electron sources have found widespread applications in vacuum microelectronic devices such as in high-resolution electron microscopy, electron lithography, holography, frequency amplifiers, field emission displays (FEDs), X-ray generators etc. [3, 11, 14, 15, 19]

2.3.2 Carbon nanotubes as field emitters

Field emission from individual carbon nanotubes

As mentioned in section 2.1, carbon nanotubes are among the sharpest inorganic structures found in nature. The small radius of curvature at the tips, high aspect ratio, exceptional thermal and chemical stability, high mechanical strength, as well as high electrical conductivity make CNTs ideal field emitters [3, 17]. Particularly, the tip geometry (i.e. the tube chirality and diameter as well as the presence of defects) is the main factor that determines the field emission properties of the nanotubes [20, 21]. Electron field emission from both single-walled and multi-walled CNTs was first demonstrated in 1995 [22-24] and has since been studied extensively. Carbon nanotubes as field emitters exhibit superior features compared to field emitters made of sharp metal tips [3, 13, 17, 25-29]:

- a) high brightness: the reduced brightness can be an order of magnitude larger than the values of metal field emitters such as tungsten;
- b) highly stable electron emission: much more stable at high currents compared to other field emitters;
- c) low threshold field for emission (i.e. the electric field to produce a current density of 10 mA/cm^2) due to small radius of curvature and high aspect ratio, the emission

- threshold field of CNTs is 2-5 V/ μm which is significantly lower than the values reported for other field emitters;
- d) relatively low vacuum level required: CNT can stably operate at 10^{-8} torr, whereas ultra-high vacuum (UHV) of 10^{-10} torr is generally required for metal field emitters such as tungsten;
narrow energy spread: $\sim 0.2 - 0.3$ eV, which is half that of metallic emitters (typically around 0.45 eV);
 - e) environmentally and economically friendly: no hazardous or precious elements used;
 - f) long lifetime: CNTs are resistant to sputtering and oxidation, and degrade gently under non-UHV, high-current, high-temperature, and high-electric-field conditions;
 - g) relatively low-cost mass production;
 - h) energy savings.

The exceptional characteristics of CNT field emitters have found them applications in a large variety of electronic devices with either single- or multiple-electron-beam, such as light sources [17, 30-33], microwave amplifiers [3, 13, 34, 35], discharge tubes for over-voltage protection [36], high-resolution electron beam instruments such as electron beam lithography (EBL) and electron microscopes [4, 35, 37], field emission displays [19, 35, 38-41], X-ray generators [26, 42, 43], etc. Some of the applications have already hit the market such as CNT based X-ray tubes (Oxford Instruments X-ray technology Inc., Xintek Inc., etc.), while others are still under active investigation or at prototyping stage.

Macroscopic FE cathodes with CNTs

Most applications of CNT field emission sources require the utilization of macroscopic cathodes with continuous or patterned films consisting ensembles of highly aligned and

uniformly distributed CNT emitters, as well as stable electron emission with high current densities. It is indeed technically challenging to achieve optimal emission performance from an array or a group of nanotubes since not only the microscopic structures of individual CNTs but also the higher-level architecture of the cathode have to be considered and optimized systemically. The key materials parameters that affect the macroscopic performance of the cathode include: the type of CNTs (i.e. SWNT versus MWNT, with closed or open caps), the presence of defects in the crystalline structure, additions of dopants, the purity of the CNTs in the film (e.g. presence of amorphous carbon or other residues), the orientation of the CNTs, the height and diameter of CNTs, the density of the CNTs, the uniformity in the distribution of CNT emitters, and the interaction of the CNTs with the supporting substrates [16, 28]. The CNT cathodes fabrication techniques have been explored and the performances of CNT cathodes for different applications have been evaluated extensively [3, 26, 33]. In particular, the technology of fabricating high current and high current density CNT field emission source array for x-ray production, and related applications developed previously and currently at the University of North Carolina at Chapel Hill are briefly reviewed in the following sections of this chapter.

2.3.3 Carbon nanotube field emission X-ray technology

The methods of fabricating carbon nanotube field emission cathodes have been studied and optimized over the past decade in our lab at the University of North Carolina at Chapel Hill [16, 27, 44-47]. The technology of developing CNT-based X-ray systems has been successfully developed and its potential for medical applications has been investigated [43, 46, 48, 49]. As illustrated in Figure 2.3, the main components of a CNT-based X-ray tube include (i) CNT field emission cathode, (ii) anode, (iii) gate electrode, and (iv) focusing electrodes. Instead of heating the cathode filament to an ultrahigh temperature as in conventional thermionic X-ray tubes, an

electric field is applied between the cathode and the gate electrode to extract the electrons from the CNT emitters. Under the high voltage (\sim kV) electrons are accelerated to bombard the anode surface for X-ray production. Two focusing lenses are usually arranged next to the gate mesh to define the shape and size of the electron beam and the resultant focal spot on the anode. All components are sealed inside a stainless steel vacuum chamber with a window made of less attenuating materials such as aluminum, beryllium, or stainless steel as X-ray exit port.

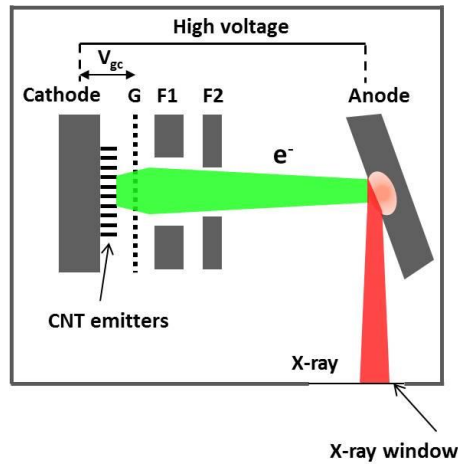


Figure 2.3 The configuration of an X-ray tube with the CNT field emission cathode. G represents the gate mesh where the electrostatic potential is applied for electron extraction. F1 and F2 are focusing electrodes for customizing the shape of the electron beam as well as the resultant focal spot on the anode. High voltages (kV) are applied between the cathode and anode for electron acceleration and X-ray generation. All parts are sealed inside an evacuated housing with a thin layer of window material as X-ray exit port. Electronic control circuit is now shown here for simplicity purpose.

The cathode is fabricated by depositing multi-walled CNTs onto the conducting substrate using a liquid-phase room temperature electrophoretic deposition (EPD) method developed previous in our lab [48, 50-52]. The CNT cathodes fabricated in such manner have demonstrated long-term stability under high current and high voltage conditions [48]. This method has enabled fabrication of CNT cathodes with variable geometries and dimensions including multi-pixel cathode arrays. The variation among individual cathodes has shown to be generally small [48].

CNT field emission based X-ray tubes have intrinsic advantages over conventional thermionic X-ray tubes. They are compact in size, with the flexibility of constructing X-ray tubes with multiple sources, and/or in different geometries and configurations (Figure 2.4). Because of the nature of field emission mechanism, the source can be electronically controlled with near-instantaneous response in either continuous or pulsed mode [43]. This allows for programmable control of each individual source when an array of multiple emitting pixels is used, as shown in on the left in Figure 2.4, meaning a more flexible utilization of the X-ray and more efficient heat management of the anode heat load.

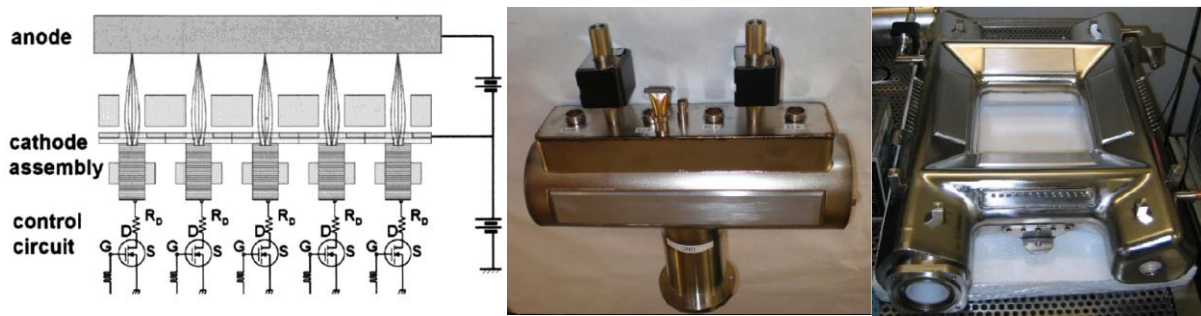


Figure 2.4 A schematic illustration (left) of a multi-beam x-ray source with five individually controlled CNT emitting pixels [53]; and examples of CNT-based X-ray tubes with multiple sources and in linear (middle) or square (right) geometries, photos courtesy of XinRay Systems Inc.

2.3.4 Carbon nanotube source array based medical devices

Carbon nanotube field emission source array technology brings a wide range of possibilities for practical applications with numerous advantages over the state-of-the-art X-ray technologies as discussed previously. In particular, the potential of translating this technology into clinical uses in both diagnostic imaging and radiotherapy devices has been extensively explored and demonstrated in our lab at the University of North Carolina at Chapel Hill.

2.3.4.1 Diagnostic imaging devices

A dynamic micro-computed tomography (micro-CT) scanner

Small animal imaging is challenging especially for organs such as lung and heart due to the extremely fine anatomical structures and the motion blurs induced by the rapid respiratory and cardiac rates. Therefore imaging techniques with both high spatial and temporal resolutions are generally required for detailed anatomical and physiological characterization in preclinical studies using small animal models. Micro-CT is widely used as a non-invasive imaging modality with resolution in the micrometer scales. The high spatial resolution is achieved by utilizing a microfocus tube with small focal spot sizes, and a high resolution detector. However the performance of most micro-CT scanners with conventional thermionic sources is still poor in resolving the fine internal structures in the organs such as heart and lung with high-frequency motion.

Gated imaging can largely reduce the physiological motion (both respiratory and cardiac) induced blurring artifacts and therefore improve the overall image quality, without having to intubate the patients, which compromises the physiological parameters of interests. There are typically two methods to perform physiologically gated CT imaging, namely retrospective gating and prospective gating [54]. Retrospective gated imaging requires taking multiple complete sets of CT projections meanwhile acquiring the physiological (respiratory or cardiac) traces. Projections are sorted into bins based on the phases they are captured and reconstructed afterwards. This method is relatively time efficient but results in a higher level of radiation dose. The other approach, prospective gated imaging, is to “freeze” the organ motion by exposing the object of interest to X-rays only at certain phase of the respiratory and/or electrocardiogram (ECG) cycles. The CNT field emission source array technology with swift switching and precise

pulse control of individual sources is an ideal suit for achieving gated X-ray imaging, and has therefore enabled the successful development of preclinical micro-CT scanners with the capability of both respiratory and cardiac gating for in-vivo pulmonary and cardiac imaging [54-57]. Two different setups have been investigated over the course of development. The first prototype contained a stationary pair of X-ray source and a flat panel detector with a rotating sample stage. The later modified model introduced a rotating gantry where the microfocus tube and detector are mounted to rotate in synchrony on opposite sides of the imaged object which stays still during image acquisition. The sample holder is mounted on a stage with freedom of linear translation along three axes. 3D volume information is acquired by rotating the source-detector pair around the sample for a full coverage of region of interest.

Figure 2.5 shows photos of the CNT-based microfocus tube and the latest model of CNT-based micro-CT scanner named Charybdis with a rotating gantry built in our lab. The microfocus X-ray tube has a focal spot size of about 50 μm and can operate at up to 50 kVp. The flat panel detector (Hamamatsu Photonics K.K., Japan) has a pixel size of 50 μm with a 50 x 50 mm active area. The scanner is equipped with physiological monitoring sensors and user control interface for monitoring the respiratory and cardiac signals which are used to gate the X-ray exposures and image acquisition. A commercial software Cobra (Exxim Computing Corp., CA) is installed for image reconstruction. Studies have demonstrated that using this CNT-based micro-CT scanner high-resolution CT images of beating mouse hearts can be obtained at 15 ms temporal resolution and 6.2 lp/mm spatial resolution at 10% system modulation transfer function (MTF) [57]. Prospectively gated pulmonary imaging with high resolution has also been demonstrated using this scanner [54]. So far the CNT-based micro-CT scanners have been installed at several facilities, including the Biomedical Research Imaging Center at UNC Chapel Hill, the

comprehensive lung imaging center at the University of Iowa, and the department of Physics and Astronomy at UNC for image-guided microbeam radiation therapy research.

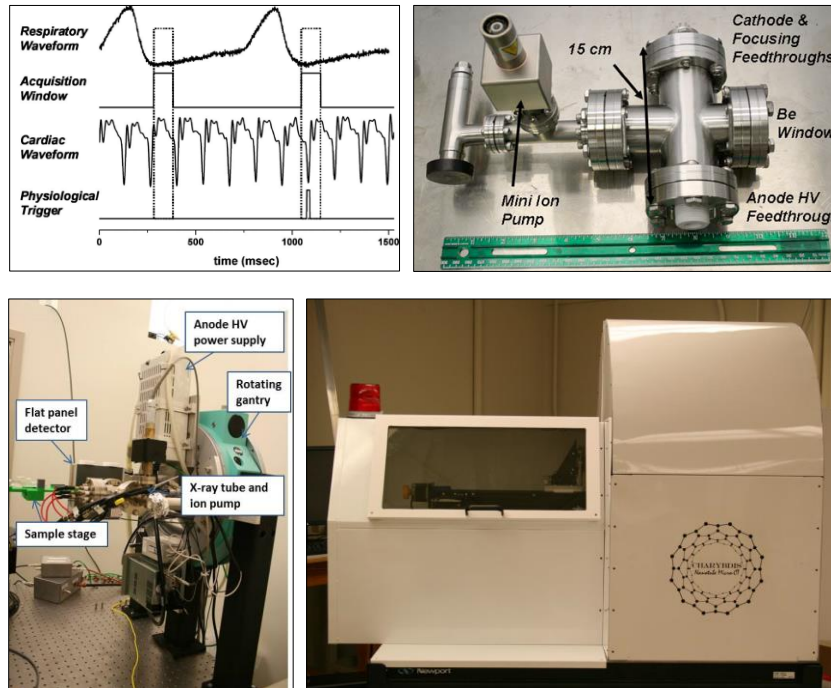


Figure 2.5 Top: a photo of the CNT field emission based microfocus X-ray tube built in the CNT-based micro-CT scanner. Reprinted from Cao et al. Medical Physics 37 (10), 2010 [57]. Bottom left: a photo showing the main components of the CNT micro-CT scanner including a rotating gantry, a CNT-based microfocus X-ray tube, a high-resolution flat panel detector, a high voltage power unit, and a sample stage. The gantry and sample stage are mounted on an optical table. Bottom right: a photo of the external appearance of the CNT micro-CT scanner Charybdis enclosed inside a painted shielding housing .

Stationary digital tomosynthesis systems

Digital X-ray tomosynthesis is a type of new imaging technique developed based upon principles of computed tomography [58] initially designed for breast cancer screening. The main idea is to produce arbitrary number of slice images over a limited angular coverage (i.e. smaller angular span than that is used in CT) and create a pseudo-3D reconstruction of the imaged object. It improves the depth information of overlapping anatomical structures that are obscured in conventional 2D radiography, with the benefit of reduced radiation dose compared to a full CT scan. Digital tomosynthesis bears great potential as a clinical imaging modality with the recent

advances in the source development, digital detector speed and efficiency, reconstruction algorithms, computer calculation power, and methods for noise reduction. The applications of digital tomosynthesis have been investigated in breast imaging, chest imaging, joint imaging, angiography and dental imaging [59].

Previously two acquisition modes are used in digital tomosynthesis systems, step-and-shoot, and continuous motion. Both modes employ a single X-ray source rotating around the object of interest and a stationary detector over the angular span [60]. Motion-induced image blurring is one of the major artifacts in digital tomosynthesis, which degrades the image resolution and therefore compromises its detection capability for objects with fine anatomical structures, or in extremely small scales such as microcalcifications in breast imaging. Continuous motion tomosynthesis systems suffer from the image blurring induced by the continuous travel of the X-ray source during image acquisition. The step-and-shoot tomosynthesis systems, on the other hand, have sources of motion from the patients due to the extended scan time, as well as mechanical vibration due to the incomplete stop of the gantry at each angular location for exposure.

The innovation of introducing CNT-based field emission source arrays into tomosynthesis creates a new mode of system operation namely the stationary digital tomosynthesis. This is an example of utilizing the unique characteristics of CNT cathodes, e.g. compact in size, electronic programmability and near-instantaneous beam response. The main concept of stationary tomosynthesis is to replace the single X-ray tube in the original digital tomosynthesis with an array of multiple X-ray sources aligned along the moving track over the angular coverage. Therefore projections are captured sequentially by individual sources in the stationary fashion which completely eliminates the use of a rotating gantry and the subsequent

focal spot blur. Besides, the rapid beam response with convenient electronic control largely reduces the overall scan time and thus limits the patient motion during the exposure.

So far, several prototypes of stationary digital tomosynthesis dedicated for different diagnostic purposes have been developed in our lab, including the stationary digital breast tomosynthesis (s-DBT) system [61-64], the stationary digital chest tomosynthesis (s-DCT) system [65, 66], and the recently demonstrated stationary intra-oral digital tomosynthesis (s-IOT) unit [67].

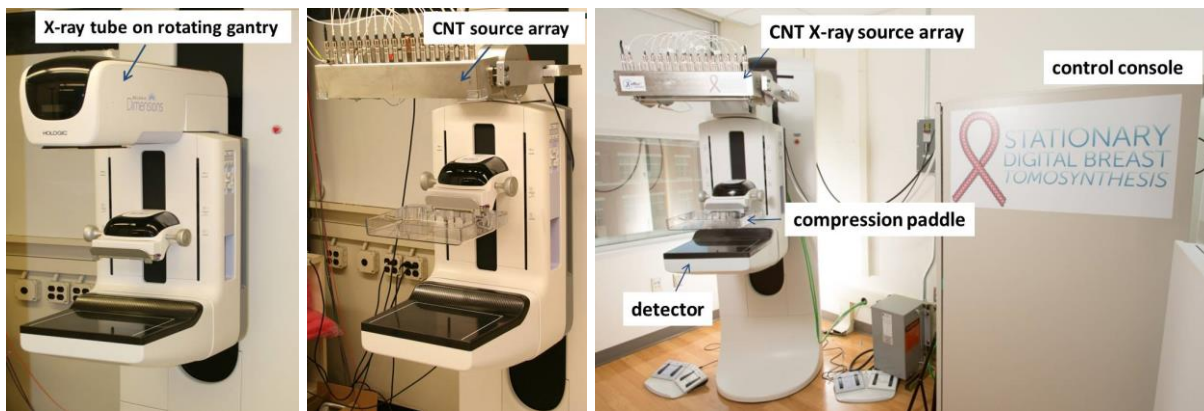


Figure 2.6 Left: the original Hologic Selenia Dimensions DBT system with a rotating gantry; middle: the prototype s-DBT system with a linear CNT source array retro-fitted into the Hologic Selenia Dimensions scanner; right: a photo of the s-DBT prototype installed at North Carolina Cancer Hospital (Chapel Hill, NC) for clinical trial [68].

Stationary digital breast tomosynthesis system

Digital breast tomosynthesis serves as a new imaging modality for breast cancer detection, and has shown to improve the detection capability over 2-D digital mammography by reducing the blur and obstruction from overlapping anatomical noise [60]. So far, there are three main commercial tomosynthesis systems made by GE, Siemens, and Hologic, respectively. The Hologic Selenia Dimensions system is the only one that has received FDA approval. Collaborating with Hologic, our group has successfully constructed an s-DBT system by retro-

fitting a linear array of CNT field emission cathodes into a Hologic Selenia Dimensions system with a rotating gantry (Hologic Corp., MA) (Figure 2.6 left and middle). The linear source array contains 31 CNT cathodes, and the focal spots span a distance of 370 mm from end to end with equal angular spacing of 1° with a maximum angular range of 30° [62]. The X-ray source array is mounted 700 mm above the detector surface with 1 mm aluminum X-ray window. The tube can operate at up to 45 kV anode voltage with a typical operation range from 26 to 36 kV. One prototype s-DBT system (Figure 2.6 right) has been installed at North Carolina Cancer Hospital for clinical trial [68], setting a milestone for CNT x-ray source array technology for medical uses.

The s-DBT system demonstrated a significantly higher spatial resolution than continuous motion DBT systems. an significant improved detections sensitivity on lesions compared to digital mammography [69]. The comparison studies by Tucker, *et al.* of imaging microcalcifications in lumpectomy specimens have shown that s-DBT produces better MC sharpness and reduced tissue overlap compared to continuous motion DBT systems [70], as illustrated in Figure 2.7.

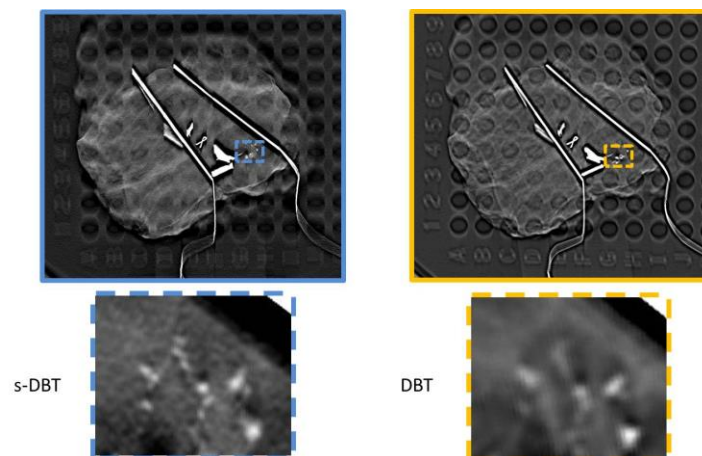


Figure 2.7 Comparison of the reconstructed images from s-DBT and DBT in human specimen study. Photos adapted from Tucker et al. Proc. of SPIE Vol. 9033, 903316 Medical Imaging 2014 [70]

Stationary digital chest tomosynthesis system



Figure 2.8 The s-DCT prototype installed at the Cystic Fibrosis and Pulmonary Diseases Research and Treatment Center, at UNC Marsico Lung Institute for clinical trials

Another stationary digital tomosynthesis (s-DCT) prototype dedicated for chest imaging has also been developed using the CNT field emission source array, with the capability to improve the detection sensitivity for small lung nodules compared to conventional 2D chest radiography [66]. A prototype s-DCT system (Figure 2.8) has been installed at the Marsico Lung Institute at the University of North Carolina at Chapel Hill for clinical trials [71]. System characterization and evaluation can be found in studies by Shan, *et al.* [66] and is not detailed here.

Stationary intraoral digital tomosynthesis system

The feasibility of using CNT field emission source array for stationary digital tomosynthesis for intraoral imaging has recently been demonstrated as well [67]. High resolution images were successfully generated with detailed 3D information of the dental and alveolar anatomy, at the patient dose comparable to a standard 2D intraoral radiography [67]. The studies

also showed improved detection sensitivity of caries, root fractures and defects. Further investigations are to be carried out to evaluate the overall diagnostic efficacy of this new intraoral imaging modality.

2.3.4.2 Radiotherapy systems for preclinical studies

The capability of CNT field emission cathodes for generating high current and current density makes them suitable sources for another medical application, i.e. radiotherapy systems.

Cellular irradiator and multi-pixel micro-radiotherapy system

Early efforts of using carbon nanotube field emission cathodes for high dose radiobiology and oncology studies include feasibility studies of developing a high-resolution electron beam irradiator for microscopic cellular region irradiation [72, 73], and a multi-pixel micro-radiotherapy (micro-RT) prototype for small animal irradiation and cancer research [53, 74-76].

The prototype single cell electron beam irradiator has demonstrated its ability of achieving a high spatial resolution of $\sim 25 \mu\text{m}$ (electron beam full-width-at-half-maximum or FWHM) with variable dose rates of 1-100 Gy/s, using a single CNT field emission cathode about 1 mm in diameter. The multi-pixel small animal micro-irradiator was proposed by fabricating a 2D array of CNT cathodes and incorporating a transmissive-type anode and a beam collimator. Desired irradiation field in various shapes can be formed by activating individual cathodes at different coordinates in the array, without having to move the animal, the source or the collimator.

Image-guided microbeam radiation therapy system

The carbon nanotube field emission source array technology enables modification of the focal spot shape from a small isotropic point to an elongated focal line. This increases the total interaction area on the anode surface, which results in a significant improvement in the total power of the X-ray production and the efficiency of heat dissipation. The CNT field emission

based line focus X-ray tubes are beneficial for certain applications where high power X-ray is required. In particular, it is an attractive alternative and practical solution for generating the specific radiation beam pattern, and it promises yet another RT modality namely microbeam radiation therapy or MRT. The feasibility of developing a CNT field emission source array based compact MRT system has been pursued and ongoing research on the system optimizing, characterization, and validation is discussed in the following chapters.

REFERENCES

1. Iijima, S., *Helical microtubules of graphitic carbon*. *nature*, 1991. **354**(6348): p. 56-58.
2. Saito, R., G. Dresselhaus, and M.S. Dresselhaus, *Physical properties of carbon nanotubes*. Vol. 35. 1998: World Scientific.
3. Saitō, Y., *Carbon nanotube and related field emitters*. 2010, Wiley-VCH: Weinheim. p. 479.
4. Bonard, J.M., et al., *Field emission from carbon nanotubes: perspectives for applications and clues to the emission mechanism*. *Applied Physics a-Materials Science & Processing*, 1999. **69**(3): p. 245-254.
5. Saito, R., et al., *Electronic-Structure of Chiral Graphene Tubules*. *Applied Physics Letters*, 1992. **60**(18): p. 2204-2206.
6. Baxendale, M., *The physics and applications of carbon nanotubes*. *Journal of Materials Science-Materials in Electronics*, 2003. **14**(10-12): p. 657-659.
7. Wood, R.W., *A New Form of Cathode Discharge and the Production of X-Rays, together with Some Notes on Diffraction. Preliminary Communication*. *Physical Review (Series I)*, 1897. **5**(1): p. 1-10.
8. Fowler, R.H. and L. Nordheim. *Electron emission in intense electric fields*. in *Proceedings of the Royal Society of London A: Mathematical, Physical and Engineering Sciences*. 1928. The Royal Society.
9. Nordheim, L.W., *The effect of the image force on the emission and reflexion of electrons by metals*. *Proceedings of the Royal Society of London. Series A, Containing Papers of a Mathematical and Physical Character*, 1928: p. 626-639.
10. Nordheim, L., *Zur Theorie der thermischen Emission und der Reflexion von Elektronen an Metallen*. *Zeitschrift für Physik*, 1928. **46**(11-12): p. 833-855.
11. Gomer, R., *Field Emission and Field Ionization*. 1961, Cambridge, MA: Harvard University Press.
12. Wiesner, J., *Characteristics and applications of pointed cathodes in scanning electron microscopes*. *Scanning Electron Microscopy*, 1973: p. 33-40.
13. Avouris, P., G. Dresselhaus, and M. Dresselhaus, *Carbon nanotubes: synthesis, structure, properties and applications*. *Topics in Applied Physics*, 2000.
14. Hainfeld, J.F., *Understanding and using field emission sources*. 1977. Medium: ED; Size: Pages: 14.
15. Fursey, G.N., *Field emission in vacuum microelectronics*. 2007: Springer Science & Business Media.

16. Cheng, Y. and O. Zhou, *Electron field emission from carbon nanotubes*. Comptes Rendus Physique, 2003. **4**(9): p. 1021-1033.
17. Saito, Y. and S. Uemura, *Field emission from carbon nanotubes and its application to electron sources*. Carbon, 2000. **38**(2): p. 169-182.
18. Ren, Z., Y. Lan, and Y. Wang, *Aligned carbon nanotubes: physics, concepts, fabrication and devices*. 2012: Springer Science & Business Media.
19. Wang, Q.H., et al., *A nanotube-based field-emission flat panel display*. Applied Physics Letters, 1998. **72**(22): p. 2912-2913.
20. Carroll, D.L., et al., *Electronic structure and localized states at carbon nanotube tips*. Physical Review Letters, 1997. **78**(14): p. 2811-2814.
21. De Vita, A., et al., *Electronic structure at carbon nanotube tips*. Applied Physics A: Materials Science & Processing, 1999. **68**(3): p. 283-286.
22. Rinzler, A.G., et al., *Unraveling nanotubes: field emission from an atomic wire*. Science, 1995. **269**(5230): p. 1550-3.
23. De Heer, W.A., A. Chatelain, and D. Ugarte, *A carbon nanotube field-emission electron source*. Science, 1995. **270**(5239): p. 1179-1180.
24. Chernozatonskii, L.A., et al., *Electron Field-Emission from Nanofilament Carbon-Films*. Chemical Physics Letters, 1995. **233**(1-2): p. 63-68.
25. Baughman, R.H., A.A. Zakhidov, and W.A. de Heer, *Carbon nanotubes - the route toward applications*. Science, 2002. **297**(5582): p. 787-792.
26. de Jonge, N. and J.M. Bonard, *Carbon nanotube electron sources and applications*. Philos Trans A Math Phys Eng Sci, 2004. **362**(1823): p. 2239-66.
27. Zhou, O., et al., *Materials science of carbon nanotubes: fabrication, integration, and properties of macroscopic structures of carbon nanotubes*. Acc Chem Res, 2002. **35**(12): p. 1045-53.
28. Hamanaka, M., V. Mammana, and P. Tatsch, *Review of field emission from carbon nanotubes: highlighting measuring energy spread*, in *NanoCarbon 2011*. 2013, Springer. p. 1-32.
29. Teo, K., *Carbon nanotube electron source technology*. Jom, 2007. **59**(3): p. 29-32.
30. Saito, Y., S. Uemura, and K. Hamaguchi, *Cathode ray tube lighting elements with carbon nanotube field emitters*. Japanese Journal of Applied Physics Part 2-Letters, 1998. **37**(3B): p. L346-L348.

31. Bonard, J.M., et al., *Field emission from cylindrical carbon nanotube cathodes: Possibilities for luminescent tubes*. Applied Physics Letters, 2001. **78**(18): p. 2775-2777.
32. Chen, J., et al., *The application of carbon nanotubes in high-efficiency low power consumption field-emission luminescent tube*. Ultramicroscopy, 2003. **95**(1-4): p. 153-6.
33. Murakami, H., et al., *Field emission from well-aligned, patterned, carbon nanotube emitters*. Applied Physics Letters, 2000. **76**(13): p. 1776-1778.
34. Meyyappan, M., *Carbon nanotubes: science and applications*. 2004: CRC press.
35. Milne, W.I., et al., *Carbon nanotubes as field emission sources*. Journal of Materials Chemistry, 2004. **14**(6): p. 933-943.
36. Rosen, R., et al., *Application of carbon nanotubes as electrodes in gas discharge tubes*. Applied Physics Letters, 2000. **76**(13): p. 1668-1670.
37. de Jonge, N., et al., *High brightness electron beam from a multi-walled carbon nanotube*. Nature, 2002. **420**(6914): p. 393-5.
38. Lee, N.S., et al., *Application of carbon nanotubes to field emission displays*. Diamond and Related Materials, 2001. **10**(2): p. 265-270.
39. Choi, Y.S., et al., *A field-emission display with a self-focus cathode electrode*. Applied Physics Letters, 2003. **82**(20): p. 3565-3567.
40. Chung, D.S., et al., *Carbon nanotube electron emitters with a gated structure using backside exposure processes*. Applied Physics Letters, 2002. **80**(21): p. 4045-4047.
41. Nakayama, Y. and S. Akita, *Field-emission device with carbon nanotubes for a flat panel display*. Synthetic Metals, 2001. **117**(1): p. 207-210.
42. Sugie, H., et al., *Carbon nanotubes as electron source in an x-ray tube*. Applied Physics Letters, 2001. **78**(17): p. 2578-2580.
43. Yue, G.Z., et al., *Generation of continuous and pulsed diagnostic imaging x-ray radiation using a carbon-nanotube-based field-emission cathode*. Applied Physics Letters, 2002. **81**(2): p. 355-357.
44. Shiffler, D., et al., *A high-current, large-area, carbon nanotube cathode*. Ieee Transactions on Plasma Science, 2004. **32**(5): p. 2152-2154.
45. Gao, B., et al., *Fabrication and electron field emission properties of carbon nanotube films by electrophoretic deposition*. Advanced Materials, 2001. **13**(23): p. 1770-1773.
46. Zhou, O.Z. and J. Lu, *X-ray generating mechanism using electron field emission cathode*. 2003, The University of North Carolina at Chapel Hill: U. S.

47. *Applied Nanotechnology Laboratory at the University of North Carolina at Chapel Hill.* Available from: <http://research.physics.unc.edu/project/zhou/>.
48. Calderon-Colon, X., et al., *A carbon nanotube field emission cathode with high current density and long-term stability.* Nanotechnology, 2009. **20**(32): p. 325707.
49. Zhou, O., J. Lu, and Q. Qiu, *Large-area individually addressable multi-beam x-ray system and method of forming same.* 2004, Google Patents.
50. Oh, S.J., et al., *Liquid-phase fabrication of patterned carbon nanotube field emission cathodes.* Applied Physics Letters, 2004. **84**(19): p. 3738-3740.
51. Oh, S. and O.Z. Zhou, *Deposition method for nanostructure materials.* 2008, Google Patents.
52. Zhou, O.Z., et al., *Deposition method for nanostructure materials.* 2011, Google Patents.
53. Zhang, J., et al., *Stationary scanning x-ray source based on carbon nanotube field emitters.* Appl. Phys. Lett. , 2005. **86**(18): p. 184104.
54. Lee, Y.Z., et al., *Prospective respiratory gated carbon nanotube micro computed tomography.* Acad Radiol, 2011. **18**(5): p. 588-93.
55. Zhang, J., et al., *A nanotube-based field emission x-ray source for microcomputed tomography.* Review of Scientific Instruments, 2005. **76**(9): p. 094301-094301-4.
56. Cao, G., et al., *A dynamic micro-CT scanner based on a carbon nanotube field emission x-ray source.* Phys Med Biol, 2009. **54**(8): p. 2323-40.
57. Cao, G., et al., *Prospective-gated cardiac micro-CT imaging of free-breathing mice using carbon nanotube field emission x-ray.* Medical Physics, 2010. **37**(10): p. 5306-5312.
58. Bick, U. and F. Diekmann, *Digital mammography.* 2010: Springer Science & Business Media.
59. Markey, M.K., *Physics of mammographic imaging.* 2012: CRC Press.
60. Kopans, D.B., *Breast imaging.* 2007: Lippincott Williams & Wilkins.
61. Qian, X., et al., *Design and Characterization of a Spatially Distributed Multi-Beam Field Emission X-ray Source for Stationary Digital Breast Tomosynthesis* Medical Physics, 2009. **36**(10): p. 4389.
62. Qian, X., et al., *High resolution stationary digital breast tomosynthesis using distributed carbon nanotube x-ray source array.* Medical Physics, 2012. **39**(4): p. 2090-2099.
63. Tucker, A.W., J. Lu, and O. Zhou, *Dependency of image quality on system configuration parameters in a stationary digital breast tomosynthesis system.* Med Phys, 2013. **40**(3): p. 031917.

64. Gidcumb, E., et al., *Carbon nanotube electron field emitters for x-ray imaging of human breast cancer*. *Nanotechnology*, 2014. **25**(24): p. 245704.
65. Shan, J., et al. *Stationary chest tomosynthesis using a CNT x-ray source array*. in *SPIE Medical Imaging Conference*. 2013. Lake Buena Vista (Orlando Area), Florida, USA.
66. Shan, J., et al., *Stationary chest tomosynthesis using a carbon nanotube x-ray source array: a feasibility study*. *Physics in Medicine and Biology*, 2015. **60**(1): p. 81-100.
67. Shan, J., et al., *Stationary intraoral digital tomosynthesis using a carbon nanotube X-ray source array*. *Dentomaxillofacial Radiology*, 2015. **44**(9): p. 20150098.
68. *Comparison of Stationary Breast Tomosynthesis and 2-D Digital Mammography in Patients With Known Breast Lesions*. 2013:
<https://clinicaltrials.gov/ct2/show/NCT01773850>.
69. Tucker, A.W., et al., *Comparison of a Stationary Digital Breast Tomosynthesis System to Magnified 2D Mammography Using Breast Tissue Specimens*. *Academic Radiology*, 2014. **21**(12): p. 1547-1552.
70. Tucker, A.W., et al. *Increased microcalcification visibility in lumpectomy specimens using a stationary digital breast tomosynthesis system*. 2014.
71. *Evaluation of the Lung Nodule Sensitivity of Stationary Chest Tomosynthesis in Patients With Known Lung Nodules*. 2015:
<https://clinicaltrials.gov/ct2/show/NCT02075320?term=Stationary+Chest+Tomosynthesis&rank=1>.
72. Bordelon, D.E., et al., *A nanotube based electron microbeam cellular irradiator for radiobiology research*. *Rev Sci Instrum*, 2008. **79**(12): p. 125102.
73. Chang, S., et al., *Development of a nanotechnology based low-LET multi-microbeam array single cell irradiation system*. *Radiat Prot Dosimetry*, 2006. **122**(1-4): p. 323-6.
74. Wang, S., et al., *A novel high resolution micro-radiotherapy system for small animal irradiation for cancer research*. *Biofactors*, 2007. **30**(4): p. 265-70.
75. Wang, S., et al., *A carbon nanotube field emission multipixel x-ray array source for microradiotherapy application*. *Appl Phys Lett*, 2011. **98**(21): p. 213701.
76. Schreiber, E.C. and S.X. Chang, *Monte carlo simulation of an X-ray pixel beam microirradiation system*. *Radiat Res*, 2009. **171**(3): p. 332-41.

CHAPTER 3: DEVELOPING A COMPACT MICROBEAM IRRADIATOR USING THE CARBON NANOTUBE FIELD EMISSION SOURCE ARRAY

3.1 Overview

As discussed in the previous chapter, the carbon nanotube field emission source array technology affords great flexibility in the source design in terms of the dimension, number of sources, geometric configuration of the individual source, and the mode of operation. This opens up new possibilities in X-ray tube design and novel applications that are not easily achievable using the conventional thermionic cathodes. Particularly, the CNT distributed source array allows for high flux microbeam production by customizing the shape and dimension of the electron beam focal spot on the anode, and therefore enables the development of a compact MRT delivery system [1].

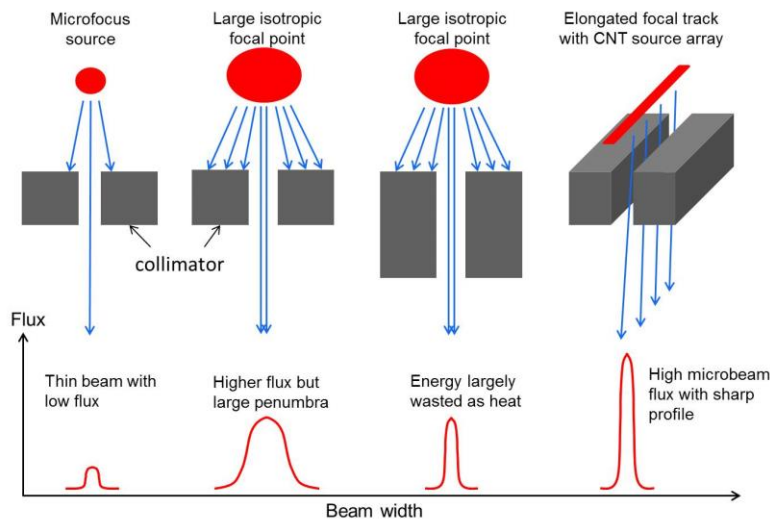


Figure 3.1 Schematic drawing illustrating the difference of point focus and line-focusing X-ray sources, the microbeam collimator needed for each source, and the resultant dose profiles.

The mechanism to produce high dose rate microbeam using CNT source arrays compared to conventional X-ray sources is illustrated in Figure 3.1. An elongated line focus with a large aspect ratio (length/width) can be generated by aligning an array of CNT cathodes in customized shape and applying optimized focusing voltages. It therefore greatly increases the anode area that receives the electron beams which results in a significant increase in the X-ray photon output. Anode melting can be avoided since the total energy is spread into a larger surface area instead of a single focal spot as in conventional high power X-ray tube. Furthermore, as shown in the drawing, a majority of the primary photon beam is blocked by the microbeam collimator and wasted as heat, in conventional X-ray tubes with isotropic oval-shape focal spots. In contrast, the microbeam generating efficiency is significantly improved with the elongated focal track since a larger portion of the photons from the primary beam can contribute to the microbeam production. This is in essence equivalent to assembling a large number of microfocus x-ray tubes and powering them simultaneously, but without the constraint of space, power consumption and beam alignment. Radiation generated from the elongated focal line provides a more uniform dose distribution along the microbeam direction while preserving the spatial resolution (steep dose gradient with a small beam penumbra) in the other direction across the microbeam.

The feasibility of high dose rate microbeams from the CNT source array was confirmed by Monte Carlo simulations and phantom-based pilot experiments, prior to the pursuit of construction of a prototype system. These efforts were previously reported in detail by Schreiber and Chang [2], and by Hadsell, et al. [3, 4] respectively.

The originally proposed concept of design of a CNT-based compact MRT system is illustrated in Figure 3.2, where multiple arrays of microbeams are delivered from different angles and directed toward the treatment target simultaneously. Each array contains several microbeams

that are generated from individually addressable cathode segments. The number of arrays to be used and their distributions can be customized according to different treatment plans. Hence, the weak penetration of orthovoltage radiation and the poor dose uptake in deep-seated target can be mitigated by spatial conformality from multi-directional microbeam arrays that overlap or interlace in the target volume, while the microbeam effects are being preserved from the spatial modulation in each array.

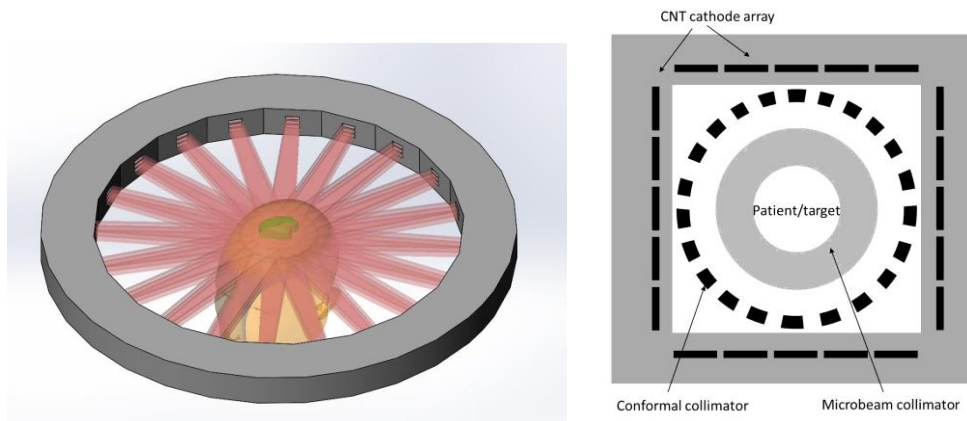


Figure 3.2 Schematic drawings of the design concept of compact high-flux microbeam delivery systems with multiple arrays of CNT generated microbeams arranged in a ring (left) or a square (right) configuration around the target to achieve dose conformality physically. Customized MRT treatment can be delivered by electronically programming the on-and-off status of individual cathode segments.

Considering the complexities and difficulties from engineering perspective involved in building a ring-shaped system, as well as other time and financial constraints, a simplified version was later proposed for preclinical studies with most of the main features resembling the original ring-shaped configuration. Instead of being a full circle, the modified system design contains four banks of vacuum chambers, with each consisting of a linear CNT source array.

After significant amount of simulations and instrumental testing conducted using a testing chamber on the performance of major components [4], the design and assembling of a

first-generation CNT-MRT system was commissioned. This prototype device employed one linear source array in the initial version.

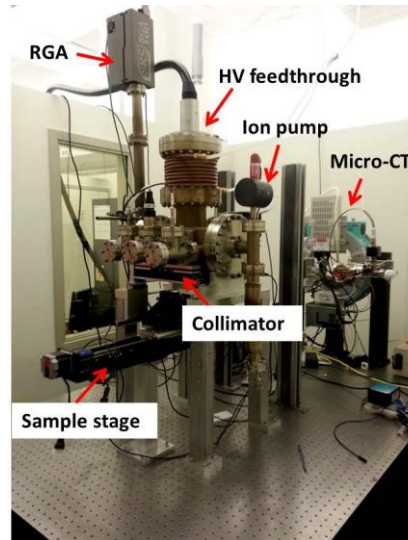


Figure 3.3 A photograph of the CNT-MRT first prototype constructed on an optical table inside a shielded enclosure in our lab at UNC Chapel Hill. Some of the main external components are indicated. Secondary shielding panels are also installed surrounding the MRT tube on the optical table during operation. As can be seen, a CNT-based micro-CT scanner is built on the same optical table to provide image guidance.

3.2 The First-generation Prototype

Thermal behavior in the X-ray chamber were simulated by finite element analysis software ANSYS™ prior to the assembling of the system to determine the technical details of the mechanical design as well as the projected power/specifications in standard operation [5]. Guided by the results from the feasibility studies as well as simulations of the performances of key components, a first-generation CNT source array based compact microbeam irradiator was designed and constructed in our lab in the Department of Physics and Astronomy at the University of North Carolina at Chapel Hill. This first-generation system has been under continuous development, systematic characterization, optimization, and validation for preclinical studies, which is the main subject of this thesis. A photograph of this irradiator is shown in

Figure 3.3, and the main components in the system design and system specifications are described in the following sections.

3.2.1 Main components

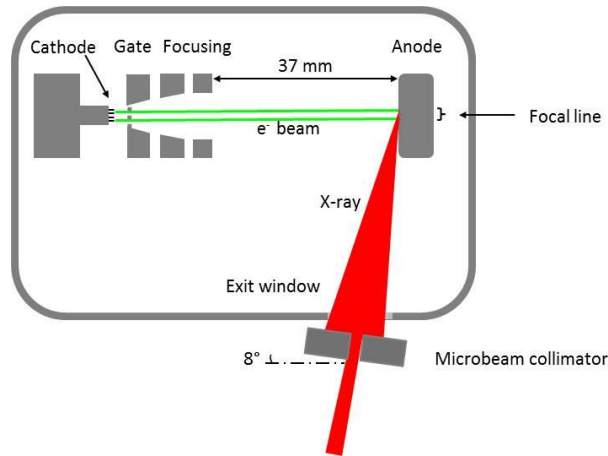


Figure 3.4 Illustration of the main components of the CNT-MRT system including the photon production structures enclosed in the vacuum chamber, and the microbeam collimator underneath the X-ray window.

The main components of the irradiator for photon production consist of the cathodes array, the anode, the gate mesh and two focusing electrodes, all of which are enclosed in a vacuum chamber with an X-ray window embedded for photon exit. The configuration is illustrated in Figure 3.4. Besides, a motorized collimation and alignment system was designed to generate microbeam from the original broad beam. It's a detachable assembly installed outside the vacuum chamber. Other parts include vacuum accessories, high voltage feedthrough, control electronics, a temperature monitoring device, and external heat exchange coils. All major components are assembled together and supported with aluminum chamber stands that affix onto an optical table. A sample positioning and translation stage is also installed on the optical table, which serves between the imaging device and the irradiator. Details of the sample stage will be

described in chapter 4. The standalone irradiator is enclosed in a secondary shielding housing made of 6 mm thick lead panels.

Cathode assembly

The linear source array consists of five individual CNT field emission cathodes. Each cathode is around 2.5 mm × 30 mm in size (effective emitting area), fabricated by depositing CNT emitters on to the molybdenum substrate using the EPD method as described in the previous chapter. Five cathodes are aligned into an array and fastened onto a glass plate from the bottom of the molybdenum substrates. The glass plate is clamped against the bottom of the gate frame with setscrews. The gate mesh is fabricated by etching a row of curved slits out of a flat sheet of stainless steel. Electrons are extracted from the CNT cathodes when a negative voltage is applied to the cathode while the gate mesh is grounded. On the other side of the gate mesh is an Einzel lens structure consisting of two focusing electrodes layered one on top of the other. Simulations on the focusing performance of the Einzel lens was performed using a commercial software package (Opera 3D Vector Fields Software, Cobham Plc, Dorset, UK) previously [6]. A photograph and SolidWorks drawing of the cathode assembly are shown in Figure 3.5.

Anode assembly and X-ray window

The reflection anode is 222 mm × 25 mm × 17 mm in size, with the bulk of it made of molybdenum. The front surface (the side facing the cathode assembly, measuring 222 mm × 25 mm) is uniformly coated with 200 μm thick layer of tungsten-rhenium alloy and is mirror finished for uniform photon production and to prevent arcing events. The anode is held in place by an L-shaped bracket (via two setscrews) which bridges the anode to a cylinder that extends to the bottom of the high voltage feedthrough. The X-ray window is 9 mm × 226 mm × 200 μm (length × width × thickness) in size made of stainless steel. It is embedded into a frame that is 38

mm × 256 mm and welded into the bottom of the X-ray vacuum chamber, as the primary photon beam escaping port as well as a built-in filter.

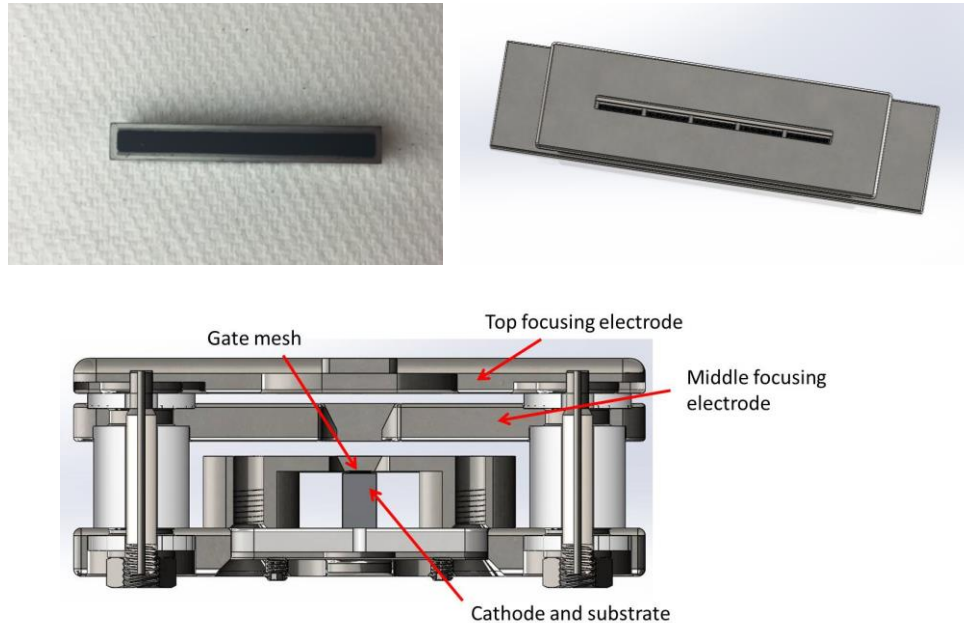


Figure 3.5 Top left: a photograph of the CNT cathode. The area in black is the deposited layer of CNT emitters. Top right: SolidWorks drawings (trimetric view) of the cathode assembly. Bottom: cross-sectional view. Main structures are labeled, including the cathode (CNT emitters deposited on molybdenum substrate), gate mesh, and two focusing electrodes.

The front surface of the anode is positioned parallel to the cathode assembly, in contrast to most X-ray tube designs where the anode is placed at a tilt towards the X-ray window. The main reason for this design is to avoid the anode thermal expansion-induced change in the vertical location of the focal line with respect to the X-ray window. Since both the focal line and the microbeam collimator slit are extremely narrow (which will be discussed below), a small change in the vertical location of the focal line or its shape would significantly affect the alignment of the collimator, and the resultant microbeam profile and dose rate. There are some remaining issues, though, with the current design of the anode assembly which will be discussed later in this chapter.

Vacuum accessories

The above components are enclosed inside a flange-sealed vacuum chamber, with a turbo pump and an ion pump (Agilent Technologies, Santa Clara, CA) incorporated from the rear and the side of the chamber respectively. A Residual Gas Analyzer (RGA) (Stanford Research Systems Inc., Sunnyvale, CA) with a vacuum gauge are also attached to the other side of the chamber for monitoring the total and partial pressures of the gases present in the chamber as well as for diagnosis purposes.

Microbeam collimation and alignment assembly

A motorized microbeam collimation and alignment assembly is attached to the bottom of the vacuum chamber right underneath the X-ray window. It is an add-on to the X-ray chamber and can be removed during conditioning or different mode of operation. A SolidWorks drawing of the collimator assembly is shown in Figure 3.6. This single slit collimator composed of two tungsten carbide blocks (manufactured by KC Precision, India) each measuring 150 mm × 17 mm × 9 mm (length × width × thickness). They are clamped against two glass spacers at both ends of the tungsten carbide blocks to form a uniform slit. The width of the slit is therefore defined by the thickness of the glass spacers, which is 175 μm in the current system, and can be varied by replacing the glass spacers. The design and dimensions of the collimator directly determine the profile of the microbeam coming out of the primary broadbeam, and were simulated and validated using a testing prototype previously [4]. Under standard MRT operation mode, the microbeam collimation assembly is installed at the bottom of the X-ray chamber beneath the X-ray window, with the collimating plane (primary beam entrance surface) positioned at 8° angle with respect to the X-ray window and ~ 65.2 mm away vertically from the anode focal line.

The alignment of the collimator slit to the anode focal line is achieved by three linear translation stages and one rotation stage (Newport Corp., CA) that drive the pair of tungsten blocks with two degrees of freedom. The actuators that motorize the translation and rotation stages are rated with precision of within 2 μm . The collimator alignment procedure will be described in section 3.4.

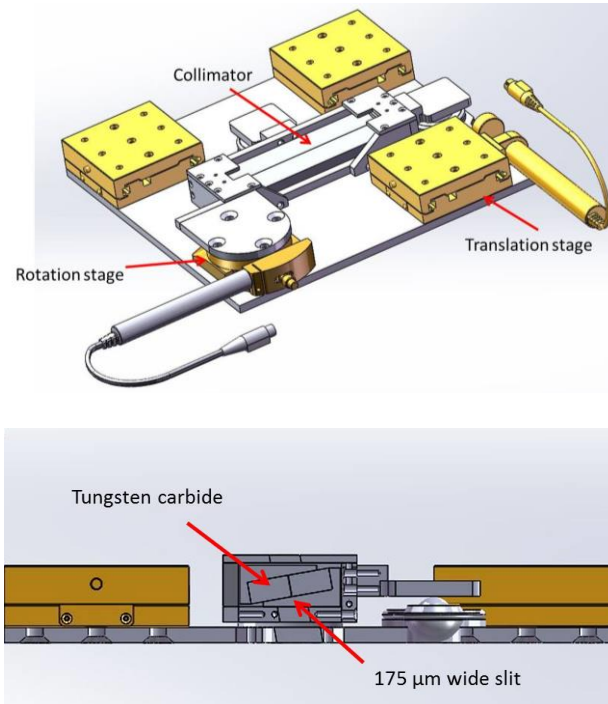


Figure 3.6 SolidWorks drawings of the microbeam collimator assembly.

3.2.2 Source characteristics

During the course of the work discussed in this thesis, the system has gone through several iterations of regular maintenance, as well as modifications regarding several detailed features. Mainly, the original five cathodes used since the completion of system construction in 2010 had degraded after 3 years and were replaced in later 2013. The fresh new cathode set as well as the rest of the main components inside the vacuum chamber have been fully conditioned following the established procedures by the source manufacturer (Xinray Systems Inc., RTP,

NC). The source characteristics and performance described here mainly refer to the system with the new cathodes since 2013.

3.2.2.1 Tube specifications in standard mode of operation (full power)

Table 3.1 Selected parameters for full power operation of the first CNT-MRT prototype

Source specifications of the first-generation CNT-MRT prototype (full power)	
Number of CNT source array	One
Anode Voltage	160 kV
Tube Current (Anode Current)	30 mA
Operation Mode	Pulsed, 8% duty cycle, 500 μ s pulse width
Focal Line Width	< 200 μ m
Heat Management	Air cooled anode, external water cooling available

The operational protocols and system specifications have been determined after detailed simulations and extensive testing, as shown in Table 3.1. To generate stable and high flux microbeam radiation, the system operates at 160 kV constant anode voltage and 30 mA total tube current from all five cathodes simultaneously. The biased extraction field is created by applying a negative electrical voltage to the cathodes while grounding the gate mesh. Emission from individual cathode can be adjusted by tuning the resistance that is connected to each cathode. The transmission rate (TR), namely the ratio of the anode current and the emission current from the corresponding cathode, is determined for each cathode. Current from each of the five cathodes is configured such that a uniformly distributed focal line is achieved on the anode. The electron emission is triggered in the pulsed-mode, with 225 μ m pulse width at 8% duty cycle to achieve the optimal cathode degradation protection and fast heat dissipation from the anode. Since there is no built-in heat exchange coils through the anode in the first prototype, external cooling coils with running chilled water are placed around the anode HV feedthrough where a significant amount of heat transfer takes place during full power operation. Additionally, external

fans and heat sinks are also available during extensive use of the system to further facilitate the heat dissipation.

3.2.2.2 Photon energy spectrum

The photon energy spectrum at 160 kVp was also measured experimentally using the Amptek XR-100T- CdTe X-ray detector with a PX4 multi-channel analyzer (Amptek Inc., Bedford, MA), and a 1 mm pin-hole collimator. The setup was placed directly underneath the bottom of the microbeam collimator plate with the pin-hole collimator positioned at 8° angle, corresponding to the tilt from the microbeam collimator. The electronics from the detector was shielded for protection. Alignment and calibration was first carried out using lower anode energies, as well as the characteristic peaks from the iodine solution. The actual measurement was taken at 160 kVp with a long exposure (~1 hour). Only dark current was used due to the sensitivity and saturation of the detector. The measured photon spectrum and the simulated one from SpekCalc are shown in Figure 3.7. The closely located k edges of tungsten and rhenium (coated layer on the front surface of the anode) are clearly identified from the spectrum in both spectra.

3.2.2.3 Focal line size

The characterization of the focal line in the prototype irradiator has been carried out following the European Standard EN12543-5 the edge method for mini or microfocus X-ray tubes. The original EN12543-5 protocol employs a phantom made of two crossed tungsten wires with a diameter between 0.9 – 1.2 mm, to determine the effective focal spot sizes in both horizontal and vertical directions across the front surface on the anode. Since the focal track in our irradiator has an extremely large aspect ratio (length/width), with the width of the focal line being relevant in most of our studies, our modified protocol uses a single tungsten wire with 1

mm diameter. The geometry of the measurement setup has been described in detailed by Hadsell [4] and is not repeated here. The effective focal line width was measured to be 131 μm , and 175 μm for the original and the new cathodes sets, respectively.

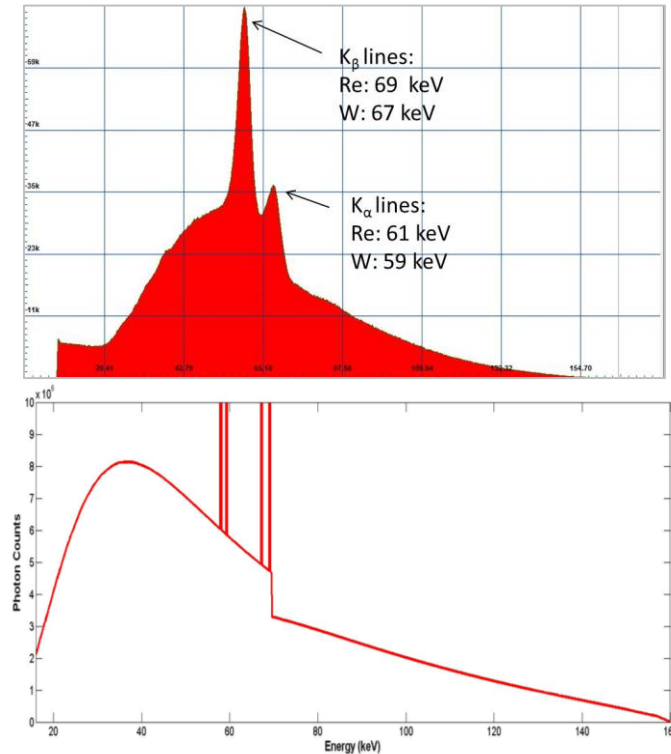


Figure 3.7 The measured photon energy spectrum measured using AmpTek XR-100T-CeTd X-ray detector (top), and the simulated spectrum using SpekCalc (bottom).

3.3 Dosimetric Characteristics

Several reasons make experimental dosimetry in MRT extremely challenging. The photon energy spectrum used in MRT spans over a large range (50-250 keV for synchrotron MRT, 10~160 keV for our first-generation CNT-MRT system). The spatial modulation means that the radiation dose delivered in the peaks can vary by hundreds of grays from that deposited in the valleys. These require the dosimeters to have sensitive and non-energy-dependent response over a large dose range. Besides, ultrahigh spatial resolution is required for the applicable dosimeter due to the submillimeter scale beam size as well as the extremely sharp dose fall-off

between the peaks and the valleys. So far there is no commercially-available dosimeter that meets all the requirements mentioned above. Specially designed high-resolution dosimeters have since then been under development or evaluation for dosimetric measurement in MRT [7, 8]. There are several potential candidates including Gafchromic films (Ashland Advanced Materials, Covington, KY), fluorescence nuclear track detectors (FNTDs) (Landauer Inc. Stillwater, OK), and two-dimensional thermoluminescence dosimetry system [9, 10]. Developing of a silicon-strip detector with the potential to achieve online dose monitoring during treatment is also one of the major focuses in experimental dosimetry in MRT with substantial progress made in the last decade.

Considering the energy and dose range that are relevant to our first-generation system, we have established dedicated dosimetry protocols using Gafchromic EBT2 or EBT3 films to characterize the microbeams. Several other new dosimeters including the nanoparticle-terminated fiber-optic dosimeter have also been investigated for dosimetry characterization of this microbeam irradiator [11].

3.3.1 **Film dosimetry with Gafchromic EBT2/EBT3 films**

Gafchromic EBT2/EBT3 films are radiochromic films that respond to ionizing radiation with color changes without requiring latent post processing such as chemical, optical or thermal development or amplification. The near-instantaneous color changing is due to the irradiation-induced polymerization process of the active film layer, and stabilizes over a short period of time. The darkness of the film after postexposure changes (or self-development) correlates to the amount of absorbed dose, and therefore is used for quantitative dose determination in the clinic [12]. The dynamic dose range for EBT2 or EBT3 films is 1cGy to over 40Gy with no or a weak energy-dependence from 100keV to 18 MeV[13]. EBT2 and EBT3 films can resolve patterns

down to 25 μm and therefore are particularly useful for high spatial resolution dose measurement. They are nearly soft tissue equivalent, water resistant, can be handled in room light. The active layer composition and thickness, as well as the dose response are the same for EBT2 and EBT3 films. For both types of film, a yellow marker dye is incorporated in the active layer that enables non-uniformity correction with multi-channel dosimetry and also decreases UV/visible light sensitivity. As the relatively new generation, EBT3 films have several improvements compared to its predecessor, EBT2 films. The active layer is laminated between two identical polyester layers in EBT3 films in contrast to the asymmetric layer configuration in EBT2 films. This will eliminate the potential errors in the scanning process due to side orientation dependence that could result in false measurements of optical density as reported for EBT2 films [14]. The polyester film substrate with silica treatment in EBT3 can effectively avoid Newton's Rings formation. The layer structures for both EBT2 and EBT3 films are illustrated in Figure 3.8. With all the aforementioned features, Gafchromic EBT2 or EBT3 films are suitable dosimeters for relative dosimetry of the first-generation CNT-MRT system in the relatively low dose range.

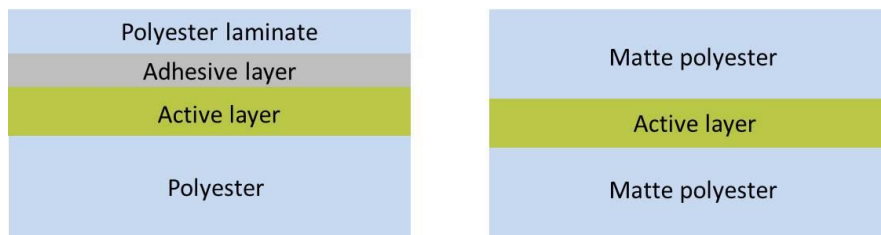


Figure 3.8 Illustration of the different layer configurations of Gafchromic EBT2 (left) and EBT3 (right) films [13].

Initial system dosimetry was carried out with Gafchromic EBT2 films as reported previously [4]. These procedures were followed and optimized in the characterization conducted in December 2013 with Gafchromic EBT3 films (lot number 07221303), and the results

presented later. The system was operating at full power with 160kV anode voltage, 30mA total tube current (anode current), 8% duty cycle with 500 μm pulse width during all dosimetric characterization procedures. No other external beam filter was applied other than the 200 μm thick stainless steel X-ray window. EBT3 films as relative dosimeters were first cross calibrated to an ion chamber in the broad field (without microbeam collimator) to establish the dose response curve, i.e. the mathematical correspondence between radiation exposure versus the pixel value of digitized films. This calibration procedure needs to be carried out with the film and the ion chamber positioned and irradiated in identical conditions, so that the corresponding radiation exposure that the EBT3 film received can be read directly from the ion chamber, as shown in Figure 3.9. The ion chamber used in the experiment was a pre-calibrated farmer-type ion chamber (RadCal 10 \times 6 – 6, from UNC Department of Environment, Health and Safety) together with an electrometer (MDH – 1015 5C). The EBT3 film sheets were cut into rectangular pieces that measured 3 inch \times 4 inch in size, and each piece was handled separately. Film orientation was labeled properly before irradiation exposure. Extra care was taken since the EBT3 films were found to be prone to edge damage from the cutting process. Split edges should be avoided in dose measurement or analysis. For each measurement, a single piece of EBT3 film was placed between two plastic layers that was each 1.09 mm thick. This setup would simulate the environment that the air in the sensitive air cavity of the ion chamber would experience, i.e beam attenuation from the top chamber wall and slight photon backscattering from the chamber wall on the bottom. The effective point of measurement in a cylindrical ion chamber is the geometric center of its sensitive air cavity for kilovoltage measurements [15]. Therefore the film with the plastic supporting layers were placed close to the side of the ion chamber with the height of the film aligned with the central line of the ion chamber, as shown in Figure 3.9. Both

the sandwiched film and the ion chamber were held in air, roughly in the center of the radiation field at a distance of 157 mm downstream from the X-ray window.

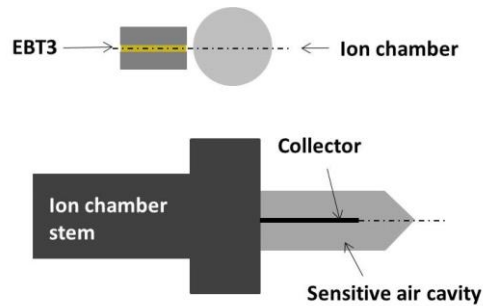


Figure 3.9 Top: Illustration of the side-by-side setup of EBT3 film and an ion chamber in the cross-calibration process. A piece of EBT3 film was placed between two thin layers of plastic, with the plane of EBT3 film aligned with the central plane of the ion chamber. Bottom: Illustration of the sectional view of an ion chamber, with sensitive air cavity and collecting electrode indicated.

A total of thirteen pieces of EBT3 films were irradiated in the setup described above with the tube operating at full power, with the exposure read and recorded from the ion chamber and the exposure time recorded with a timer as well. The measured radiation exposure levels ranged from $0 - 1.0 \times 10^4$ Roentgen (exposure time ranged from 0 to 100.0 min). A constant exposure rate of 100 R/min was confirmed from the first five exposure levels (consistent in repeated experiments), and was thereafter used for longer exposures that were beyond the readout limit of the electrometer which was 1000.0 Roentgen. The ion chamber was found to have a constant background reading of 10.2 mR/min and was subsequently subtracted from each exposure point.

The selected measurements had a denser distribution in the lower exposure level ranges (7 measurements in 0 – 1000.0 R range, 6 measurements from 1000.0 – 10000.0 R). The EBT2/EBT3 calibration curves showed a greater gradient in the lower dose range, and tended to flatten out over high dose range, as reported by the manufacturer and our previous experiments. Therefore an abundance of measurements in the high gradient region would be beneficial for curve fitting afterwards to yield an accurate valley dose definition in our experiments.

The exposed EBT3 films were stored in the dark for at least 24 hrs before digitized. The film scanning process was carried out using an EPSON V700 scanner following the procedures recommended by the manufacture. All three color channels (RGB) were employed and analyzed separately to generate three dose response curves at thirteen exposure levels. When analyzing each film in *ImageJ* (developed by NIH, public domain), a region selection box of 1 × 1 inch size was placed in the center of the exposed region where the dose distribution is uniform, and the averaged pixel value from the selected region was recorded for all three color channels. After converting the exposure to dose using the conversion factor of exposure to absorbed dose in dry air (air kerma) which is 0.0087, the dose response curves for each channel were plotted and shown in Figure 3.10.

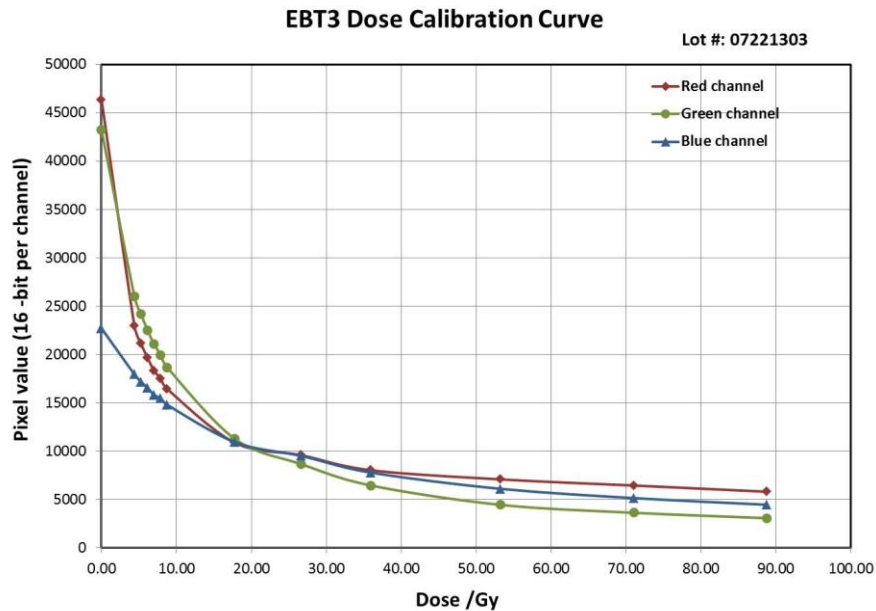


Figure 3.10 Dose responding curves of EBT3 film (lot number 07221303) in three color channels obtained through cross calibration to ion chamber. The system was operating in standard mode at full power, i.e. 160 kVp, 30mA tube current, 500 μm pulse width at 8% duty cycle. Spline-fitted are shown only to guide the eyes.

The discrete points were fitted into continuous curves with polynomial regression for each color channel. This curve fitting method was shown to match closely with rational fit in the

dose range used in our experiments (unpublished data). The data point at 27Gy was determined to be an outlier, and was excluded in the curve fitting and following analysis. Based on the fitted calibration curves, a dose calculation program was developed with *MATLAB* (MathWorks Inc., Natick, MA), which employed multi-channel analysis as recommended by the manufacturer. The red channel was used for low dose reading up till 10 Gy due to its highest sensitivity, while green channel was used for measurements of high dose beyond 10 Gy. This program has been used for the analysis of EBT3 films (lot number 07221303) thereafter.

The microbeam collimation assembly was installed after broad field film calibration. The system dosimetric parameters including half value layer, distance correction curve, dose rate, percentage depth dose, tissue maximum ratio were subsequently quantified following the protocols described by Hadsell [4]. A different procedure was used here compared to those reported by Hadsell in 2013. All measurements were performed with Gafchromic EBT3 films and a custom *MATLAB* program with multi-channel analysis, and the same set of parameters of beam quality were evaluated using Gafchromic EBT2 films and analyzed with FilmQaPro software developed by Ashland Advanced Materials (Covington, KY).

3.3.2 **Half value layer (HVL)**

Half value layer, or HVL, is the parameter that is often used to characterize the spectrum or hardness of a radiation beam. It refers to the thickness of material that attenuates the intensity of radiation entering it by one half. HVL is usually specified in millimeter of aluminum low energy X-ray beams and measured in narrow beam geometry to avoid large amount of scatters generated in aluminum. The first HVL of our CNT-MRT system was measured in microbeam mode where the beam was estimated to be around 300 μm wide, and therefore the narrow filed requirement was met. An aluminum step phantom was made for this measurement, with the

dimensions shown in Figure 3.11. There were a total of 10 identical steps on the aluminum phantom, and the difference in height is 2.54 mm between the adjacent steps. A piece of EBT3 film was sandwiched between two 3 mm thick acrylic layers and placed underneath the aluminum phantom with 3 mm air gap between the bottom of the step phantom and the top layer of acrylic. The air gap prevented an interface effect between the aluminum and the film. The entire setup was placed on top of the translation stage and the measurements were performed in a step-and-shoot mode, with each microbeam irradiating through one of the ten steps on the phantom. The distance between the focal line to the film was 122.10 mm. In calculating the HVL one must recall that the microbeam traveled through the phantom material at 8° degree angle. The results were summarized in Figure 3.12, and the first half value layer was determined to be 7.62 mm in aluminum with the CNT-MRT system operating at 160 kVp, 30 mA tube current.

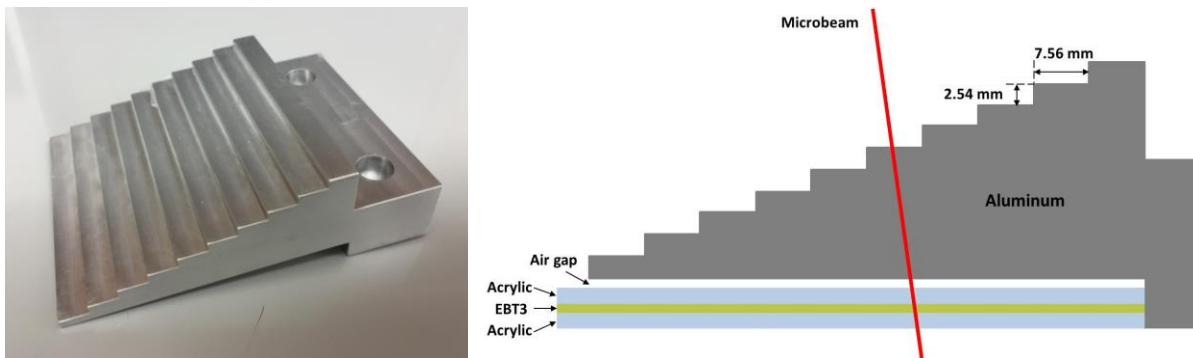


Figure 3.11 A photograph (left) and drawing (right) of the aluminum step phantom for half value layer measurement. The phantom has a total of ten identical steps, with each being 2.54 mm in height and 7.56 mm in width. The direction of microbeam penetrating through the step is indicated. The measurement EBT3 film sandwiched between two thin layers of acrylic was placed underneath the phantom. The dimensions are not drawn to scale.

According to AAPM TG-61 protocol for kilovoltage X-ray beam dosimetry table IV, for first HVL of 7.62 mm aluminum the corresponding factor to convert air kerma to water kerma is 1.043 after linear interpolation [15]. The f-factor is the conversion factor from exposure in air to absorbed dose in tissue or water as defined in equation:

$$D = f \cdot X$$

where D is the tissue absorbed dose in rads, X is the air exposure in Roentgens. Combining the air kerma to water kerma conversion factor together with the conversion of exposure to absorbed dose in dry air (air kerma), the f-factor was thus calculated to be 0.915 rad/R.

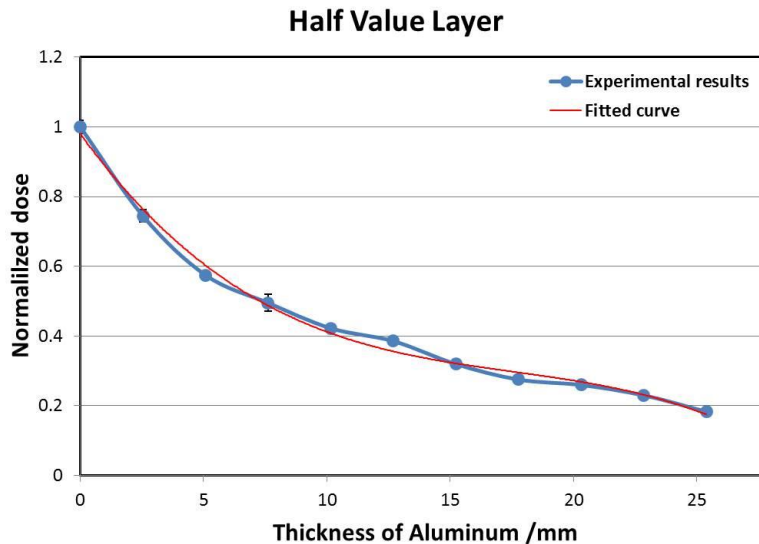


Figure 3.12 Results of HVL determination. Measurements were carried out in step-and-shoot mode with ten microbeam exposures onto each step of the aluminum phantom. The absorbed doses from ten exposures were recorded by a single piece of EBT3 film placed underneath the phantom. The successive exposures were separated horizontally far enough to avoid the effect or scatter from the previous or subsequent exposures.

3.3.3 Dose rate

The average microbeam entrance dose rate (DR) at certain sample heights and the consistency were evaluated. The EBT3 film was sandwiched between acrylic layers in the same way as in the experiments described above, and placed on top of a lab jack, which was 36.99 mm away from the bottom of the collimator. This yielded to a source to axis distance (SAD, focal line to center of the film) of 122.10 mm. Four microbeam exposures were delivered successively with exposure time ranging from 5min to 20min, and the results were shown in Figure 3.13. The average microbeam entrance dose rate was thus determined to be 1.01 ± 0.14 Gy/min at this

sample height, with the system operating at 160 kVp at 30 mA tube current. Radiation was triggered in pulsed-mode at 8% duty cycle and 500 μ s pulse width. The peak microbeam DR corresponds to the in-pulse dose rate. The variation in the dose rate measurements could come from the small fluctuation of cathode current during beam-on time, the variation of film response at different locations due to inhomogeneity, and the uncertainties in the dose/DR response of the EBT3 film. The calculated DR in this measurement only corresponded to the entrance dose rate at this particular sample height. Entrance dose rate at different sample heights or tissue depths shall be calculated with the distance correction, PDD, and TMR results that are described in the following sections.

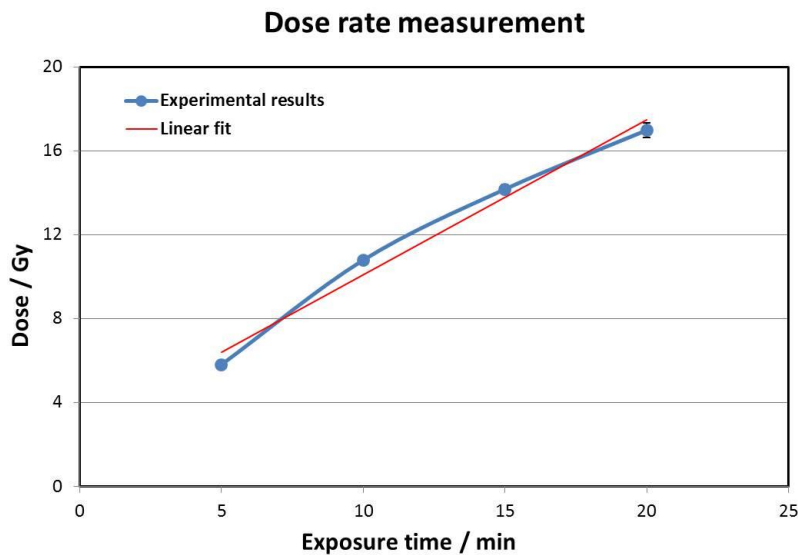


Figure 3.13 Results from the average dose rate measurements that were performed with the system operating at 160 kVp, 30 mA anode current, 8% duty cycle, and 500 μ s pulse width. The film was placed at 122.10 mm down from the focal line.

3.3.4 Distance correction

Due to the uniqueness of our radiation generation mechanism as well as the focal spot geometry in our CNT-MRT system, in-air primary beam flux falloff behavior over certain source-to-surface distance is expected to differ from those in clinical LINAC or conventional

orthovoltage X-ray tubes. In order to characterize such relation properly, a distance correction curve was obtained by taking multiple dose measurements at different distances from the focal line along the microbeam path. A piece of EBT3 film sandwiched in the acrylic layers was placed on top of a specially designed sample stage which was capable of high-precision translation along both vertical and horizontal directions. The system was operating at full power as described above, and eleven irradiations were carried out in the step-and-shoot mode, with the exposure time for each irradiation being identical. The measurements covered the SSD range from 114.48 mm to 139.88 mm, which was the distance window for conducting animal studies discussed in the following chapters. The results were analyzed and summarized in Figure 3.14. As shown on the curve, the microbeam output falloff doesn't follow the inverse square law at such short SSD. As the SSD increases the focal line becomes essentially a finite focal point from the point of measurement, therefore one can expect the flux to drop following more closely to the inverse square relation. Also noticed during the analysis of the film was the slightly increased beamwidth (by about 70 μm) over the distance range in this experiment, which was expected mostly due to the divergence nature of radiation beam generated in this system. The beam profiles acquired with EBT3 films were shown in Figure 3.15.

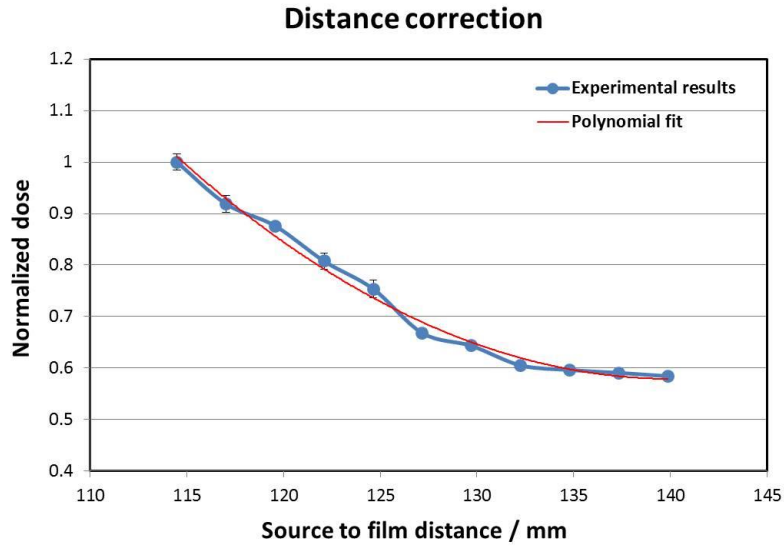


Figure 3.14 The distance correction curve obtained using EBT3 films, for SSD between 114 to 140 mm, with the system operating at 160 kVp, 30 mA tube current, 8% duty cycle, and 500 μ s pulse width.

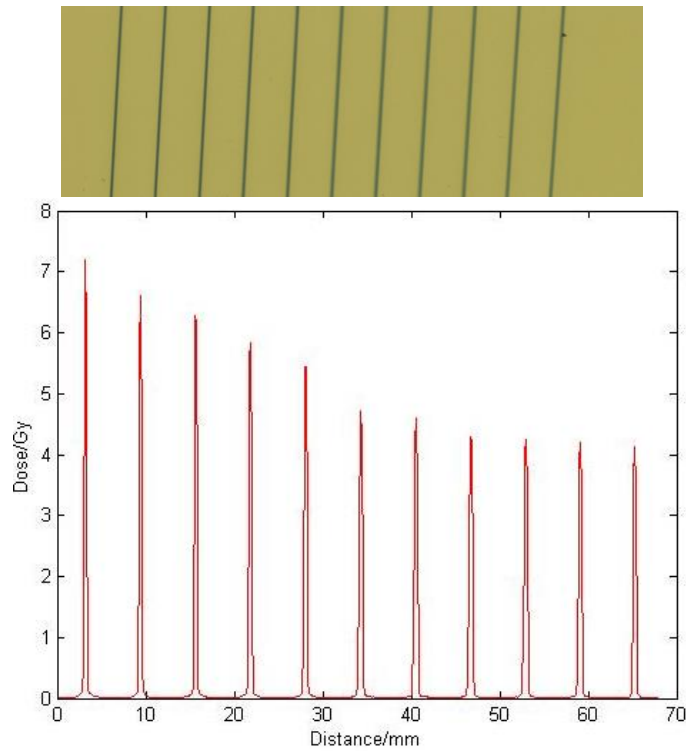


Figure 3.15 Beam profiles (bottom) at different distances recorded by the EBT3 film (top) during the measurement of distance correction curve. The beam center-to-center distance shown in this figure does not correspond to the vertical distance translation, but the horizontal translation distance between two successive exposures on the film

3.3.5 Percentage depth dose (PDD)

The quantification of beam attenuation as it travels in a medium is one of the major steps in reference beam dosimetry. The percentage depth dose (PDD) is one of the quantities that are defined for characterizing the depth dose distribution in tissue along the beam axis. It refers to the relative absorbed dose at a certain depth along the axis of the beam compared to that at the reference depth, as expressed in the following equation:

$$PDD = \frac{D_d}{D_{d_0}} \times 100$$

where d_0 is usually the depth with maximum deposited dose d_{max} , and D_d is the absorbed dose at depth d . For orthovoltage and low-energy X-rays, d_{max} is at the surface of the phantom, i.e.:

$$d_0 = d_{max} = 0 \text{ (surface)}$$

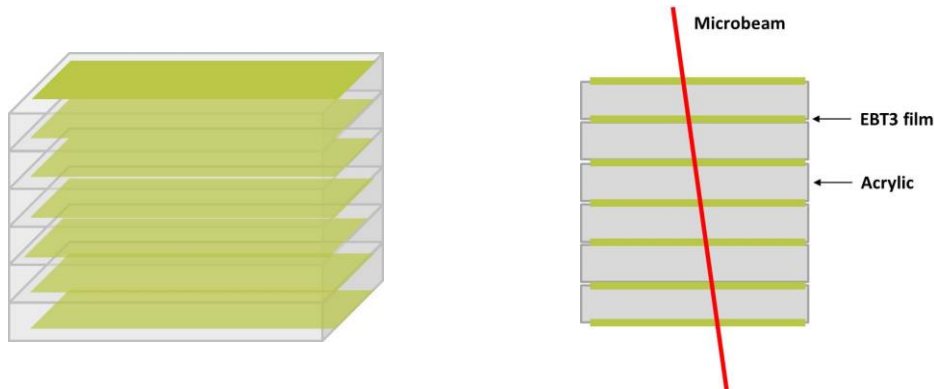


Figure 3.16 Illustration of the acrylic phantom for PDD measurement. Each slab was 2.8 mm thick. Seven pieces of EBT3 films were inserted between adjacent layers. One microbeam irradiation was carried which exposed all seven films simultaneously at 8° angle, as shown in the side view of the phantom on right. The figure is not drawn to scale.

The PDD curve is usually established through numerous measurements in a water equivalent phantom at varying depths along the beam axis with a constant source-to-surface distance (SSD).

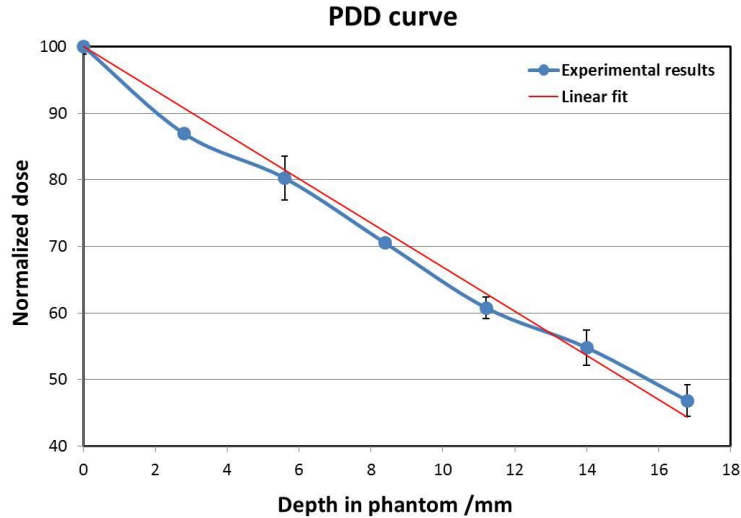


Figure 3.17 Percentage depth dose (PDD) curve taken with EBT3 films and the acrylic phantom placed at 22.19 mm down from the bottom of the collimator.

A PDD phantom was constructed from a stack of six acrylic slabs of same dimensions with a piece EBT3 film placed between two adjacent slabs, as shown in Figure 3.16. The phantom was placed on the lab jack, with the top surface being 20.19 mm downstream from the bottom of the collimator, and a single microbeam exposure of 15 min at full power was delivered. As shown in Figure 3.17, the depth dose distribution obtained through this method presents a near-linear falloff in the acrylic phantom. Another factor to be noted is that, acrylic shows an attenuation coefficient that is a bit higher than water for the beam energy used in our system. Therefore, the actual percentage doses at corresponding depths were underestimated with this method.

3.3.6 Tissue maximum ratio (TMR)

Tissue maximum ratio, or TMR, is another parameter defined to characterize the depth dose distribution in tissue for dose calculation. The main distinction between TMR and PDD is that, the SAD remains constant in the measurement of TMR with the point of interest at varying depth along the beam axis in the phantom, whereas SSD is constant during PDD quantification.

The definition of TMR relates to another depth dose quantification parameter called tissue phantom ratio (TPR) which refers to the dose at a given point in phantom to the dose at the same point at a fixed reference depth. TMR is simply a special case of TPR where the reference depth is the depth of maximum dose, d_{max} , as defined in equation:

$$TMR(d, r_d) = \frac{D_d}{D_{d_{max}}}$$

where r_d is the lateral distance from the central axis of the beam, D_d is the dose deposited at depth d , and $D_{d_{max}}$ is the maximum dose along the central axis. The primary beam attenuation is then represented by:

$$TMR(d, 0) = \frac{D_d}{D_{d_{max}}}$$

where d_{max} is again at the surface of phantom for the kilovoltage X-ray beams.

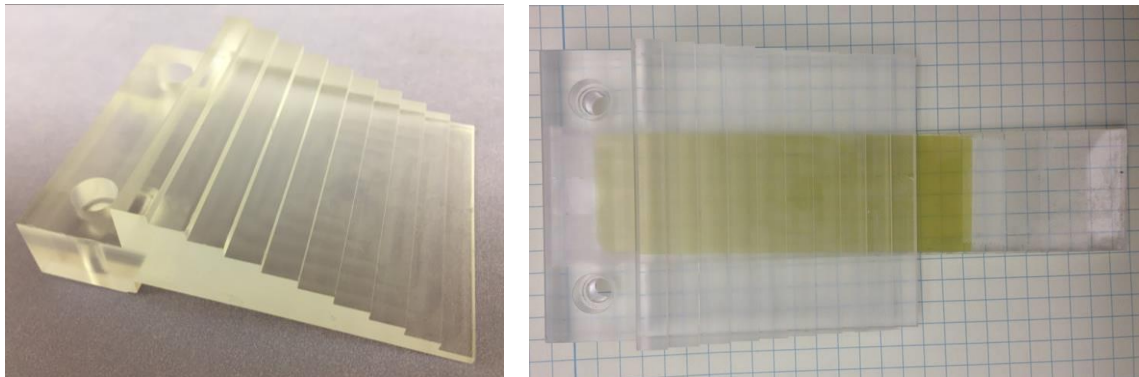


Figure 3.18 Photographs of the acrylic step phantom for the measurement of TMR.

Based on such definition, a step phantom for TMR quantification (as shown in Figure 3.18) was made with acrylic with the same shape and dimensions as HVL aluminum step phantom. A single piece of EBT3 film was placed right beneath the bottom surface of the acrylic phantom with no air gap in between, different from the setup in HVL measurement. Two layers of acrylic were put underneath the EBT3 film and taped tightly to the body of the acrylic step

phantom to secure the entire setup and avoid any air gap or relative displacement. The phantom was positioned on the lab jack with the top surface at a distance of 36.99 mm down from the bottom of the microbeam collimator, which equaled to 122.10 mm from the focal line. Eleven radiation exposures were delivered in the step-and-shoot mode with the system operating at full power. The beam-on time was kept the same for each exposure. The results were analyzed and plotted in Figure 3.19. The curve was fitted with second degree polynomial regression. However, both linear regression and semilogarithm regression could achieve close fit but slightly off from the polynomial regression. The results presented here differed from those reported by Hadsell in the system dosimetry characterization with EBT2 and FilmQaPro in 2012. Suspected sources of uncertainties include the tube current fluctuation especially during longer exposures, slightly unstable tube performance at high temperature after long beam-on time, geometric inconsistencies in the film, and limited number of measurements. The distance range covered in this characterization process was considered sufficient for the purpose of dose calculation in animal studies in the prototype system. However, further work is still desired for a more thorough and consistent dosimetric characterization, including increasing the measurement sample size (reducing the depth step size), for a water or tissue equivalent phantom, and improving the current stability during exposure.

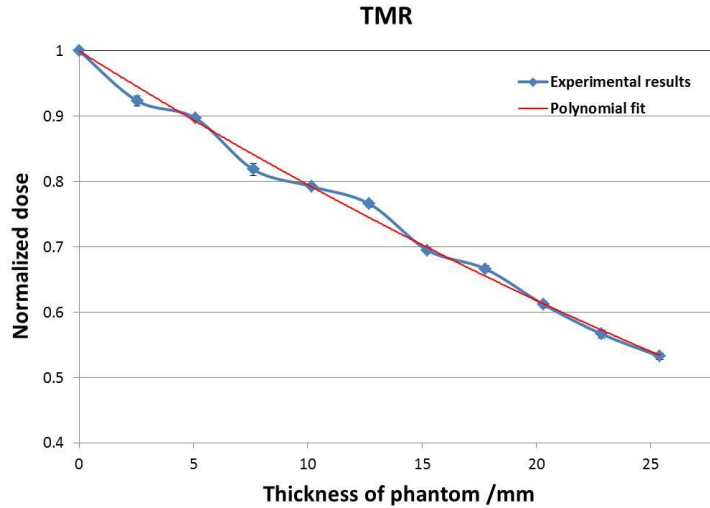


Figure 3.19 The tissue attenuation of the microbeam in acrylic. Data were obtained using EBT3 film placed at 122.10 mm downstream from the focal line.

3.4 Challenges and Remedies

3.4.1 Microbeam collimator alignment

Microbeam radiation is generated by a multi-slit collimator on the relatively wide and quasi-parallel photon beam at a synchrotron beamline. Other than the collimator slit orientation with respect to the polarization of the beam, alignment of the collimator exactly at certain coordinates is usually not an issue and has little effect on the resultant microbeam profiles. Similarly, no particular orientation in the collimator position of a conventional thermionic tube with a large isotropic focal spot was used for microbeam generation. However, due to the unique geometry of the focal track on the anode as well as the extremely narrow widths of the focal line and collimator slit (both within 200 μm in width), it is a critical and challenging task to align the extremely narrow collimator slit exactly with the thin focal track in order to achieve the highest microbeam flux and the smallest microbeam width. This is also essential to obtain a uniform dose distribution along the microbeam long axis. An efficient and accurate alignment method has been developed which takes advantage of the geometry of linearly aligned cathodes array. There

are five cathodes that contribute to the total tube current and photon flux, and the focal tracks created from each of them overlap on the anode. Every cathode geometrically dominates a portion of the focal line and therefore the photon flux in the resultant microbeam. This was confirmed by capturing the beam profiles from each of the five cathodes individually using a flat panel detector and radiochromic film placed downside from the microbeam collimator. The beam profile generated by a single cathode shows a non-uniform dose distribution along the beam with a higher flux appearing at the location corresponding to the geometric location of the emitting cathode in the cathode array. For instance, the microbeam profile along the beam showed a higher dose deposition in the middle than that on the rest on the film when only the third cathode (located at the center of the cathode array) was turned on. In contrast, when the first or fifth cathode (located at either end of the cathode array) was emitting, the deposited dose on microbeam profile appeared to be the highest on the corresponding end, and gradually decreased farther away from the site of the emitting cathode. In the ideal case where the collimator slit is accurately aligned with the anode focal line and the collimator plane positioned at the 8° projection angle, the obtained microbeam should be the sum of microbeams from five cathodes overlapping exactly. In this configuration, the resultant microbeam delivers the maximum flux with uniform dose distribution along the beam, and a symmetric dose profile across the microbeam with the minimal beamwidth. In any case where there was a misalignment between the focal line and the collimator slit, the above microbeam profile would not be achieved.

Based on this fact, a dedicated method for collimator alignment has been developed with a flat panel detector (Hamamatsu C7940DK-02), a partition made of highly attenuating material (lead or tungsten), and a LabVIEW program for real-time camera readout of the beam profile and

photon counts. During the setup, the detector is positioned on the translation stage below the microbeam collimator with the slit roughly aligned with the center line of the active area of the detector ($10 \times 10 \text{ mm}^2$). The lead partition ($3 \times 5 \times 10 \text{ mm}^3$ in size) is placed on top of the detector active area. The standing partition shields against the photons that come at an angle from reaching the other side of the lead. In addition, the vertical height of lead (5 mm) on the microbeam path is sufficient to block almost all photons from reaching the detector region beneath the partition.

Particular caution needs to be taken when using the sensitive flat panel detector under the primary beam path as the high energy and high intensity radiation beam could cause damage to the active area. The alignment is performed with the tube operating at 50 kVp, with less than 1 mA total tube current, and 1% duty cycle. As discussed earlier in this chapter, the collimator has two degrees of freedom, rotation and translation controlled by three linear translation stages and one rotation stage. The alignment procedure usually starts with tuning the rotation of the slit, and proceeds with the translation adjustment afterwards. Firstly, cathodes one and five are turned on simultaneously as illustrated in Figure 3.20 on the left. The recorded profile along the microbeam on the detector appears segmented, and the beam intensity varies on different regions along the beam as shown in Figure 3.20 on the right. The detector area where the lead partition lands is almost completely shielded with minimal to no photon counts. On both sides of the shielded area are the regions that receive photons mainly from one end of the focal line. The two ends of the microbeam receive the highest flux of photons with less influence from the lead partition.

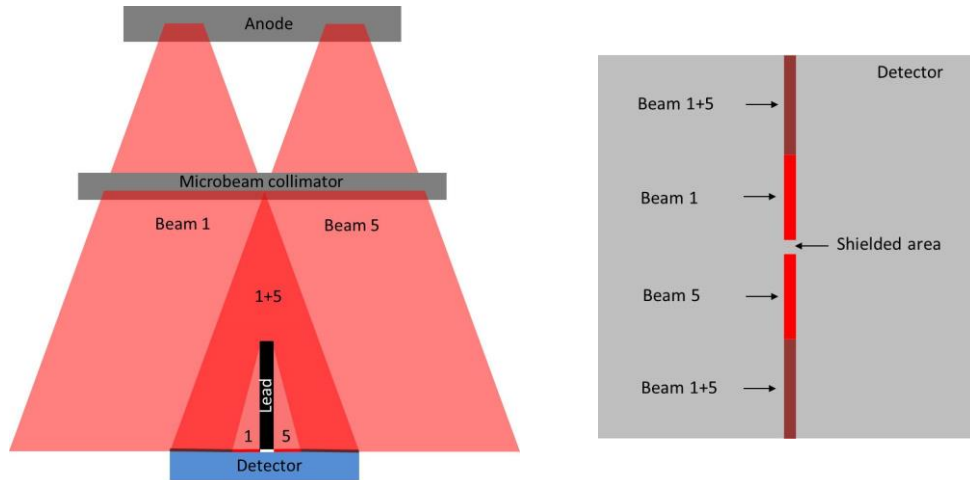


Figure 3.20 Left: Illustration of setup and irradiation configuration for microbeam collimator alignment; right: beam profile recorded on the detector. Dimensions are not drawn to scale.

If the two segments on the detector appear shifted in the lateral direction of the beam, as shown in Figure 3.21 on the left (top), it usually indicates an angular misalignment of the collimator slit with respect to the focal line. This is illustrated on the bottom left in **Figure 3.21** when looking towards the anode focal track through the collimator slit from the bottom of the tube. The angular offset can be corrected by rotation of the stage. The beam profile is updated in real-time to reflect the adjustment, conveniently providing feedback to adjust the direction and the step size in the rotation accordingly. Angular alignment is considered achieved when the two segments on the beam profile are aligned in center as shown in **Figure 3.21** on right. A comparison of beam profiles collected using EBT3 film before and after collimator alignment is illustrated in Figure 3.22.

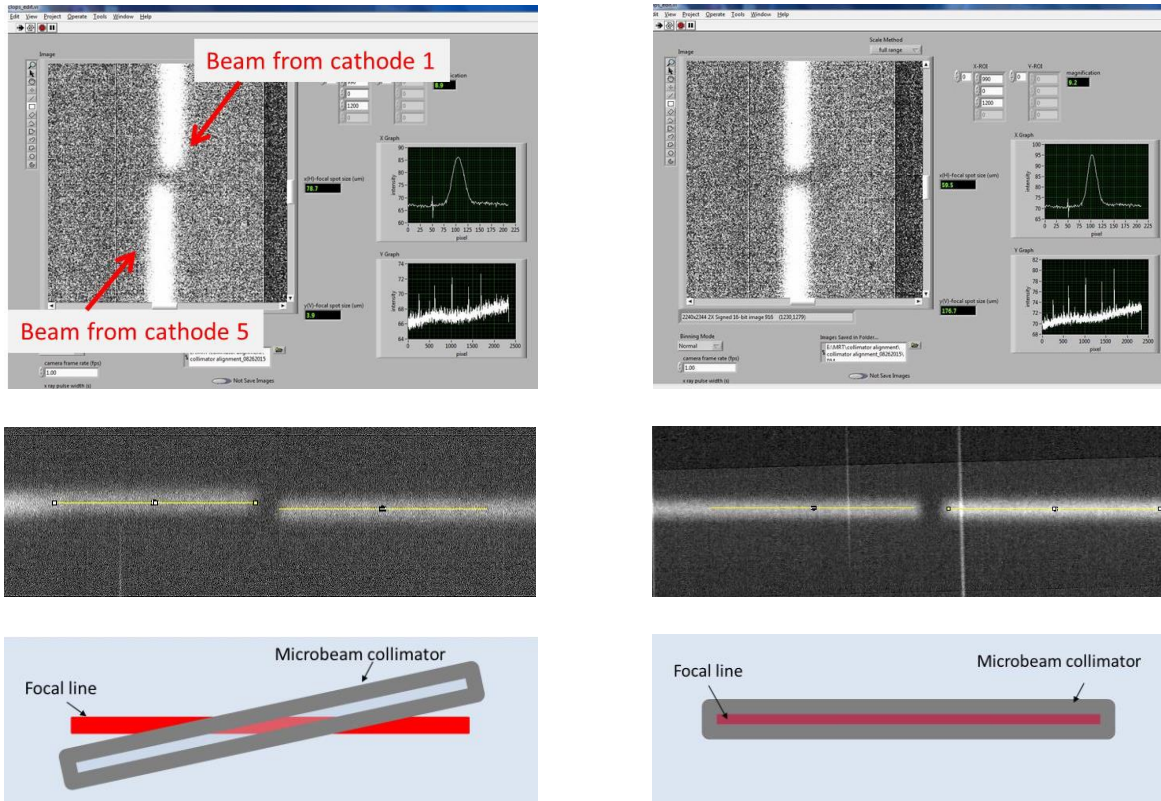


Figure 3.21 Top row: Screenshots of the detector readout of the beam profile and photon flux during the collimator alignment. Two segments appear shifted if the collimator slit is not in parallel position with respect to the focal line on the anode, as shown on the left. The one on the right indicates a parallel-aligned slit and focal track. Middle row: images acquired by the detector shown in ImageJ. Bottom row: illustrations of the relative locations of the collimator slit and the anode focal line when not-aligned (left) and aligned (right) corresponding to the beam profiles as shown in the top and middle row. Dimensions are not drawn to scale.

Horizontal translation follows when the angular alignment is completed. This is usually carried out with all five cathodes on simultaneously but at reduced anode voltage (60 kVp), low current and duty cycle to protect the detector. The averaged cross field microbeam profile is plotted on the right hand side of the user interface reflecting the photon flux in the peak and the shape of the beam. The photon count in the peak changes with the horizontal location of the collimator slit, and reaches the maximum once the slit reaches the desired location where the alignment is achieved as described earlier. Symmetry in the profile is another indicator of proper alignment.

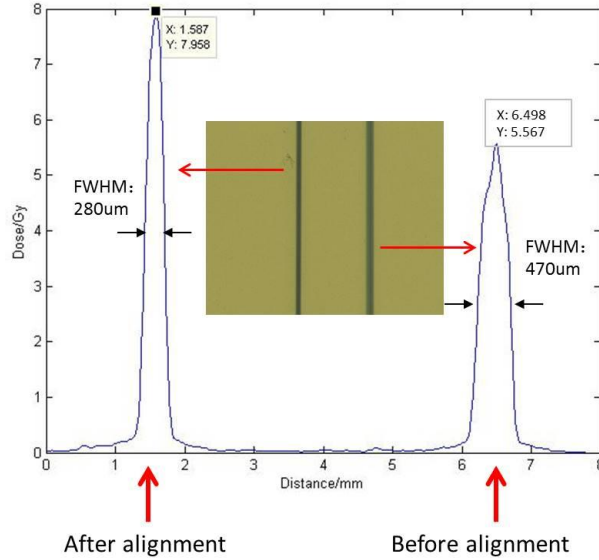


Figure 3.22 Comparison of the beam profiles before (right) and after (left) collimator alignment. Notice the change in the beam shape and peak dose rate.

3.4.2 Anode rotation

As described in section 3.2, the first prototype CNT-MRT system employs a stationary molybdenum anode that is positioned parallel to the cathode assembly with the front surface perpendicular to the X-ray window. The anode is attached to the L-bracket via two M5 setscrews that thread into the bracket through the body of anode from the bottom. This design with a non-tilted anode could largely limit the vertical drift in the relative location of the focal line, which is caused by thermal expansion of the anode material with a tilted anode, comparing to the case with a tilted anode. However, it turned out that the motion of the anode within the horizontal plane was not securely constrained in this design. Any rotation of the anode about the vertical axis would affect the location of the focal line significantly and result in the misalignment of the collimator, as in the lower left in Figure 3.21. This was observed for the first time when a sudden drop of dose rate and a large broadening in the beamwidth was confirmed during an experiment in 2013 after the system had been operating steadily with stable output of microbeam radiation

for over two years, near the end of the lifetime of the first set of cathodes. Realignment of the collimator through rotation was not able to bring the flux back the normal level. The anode was later found rotated about its central axis along the vertical connecting cylinder, as shown in Figure 3.23 on right. Similar incidents took place a year after the repair, when a gradual broadening of the microbeam width and a significant decrease in the dose rate were found during routine beam quality examination using EBT3 films. The extent of rotation was measured to be around 2 to 3 degrees from the initial location.

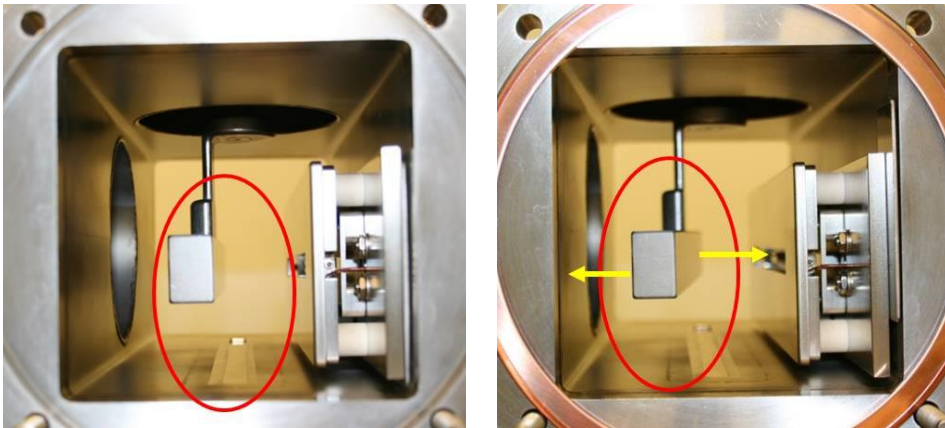


Figure 3.23 Left: Non-tilted (in both vertical and horizontal directions) anode as originally installed. Right: the rotated anode with further end from the plane of the paper drifted towards the cathode assembly, while the closer end moved towards the back wall of the chamber.

After examination, two threaded joints of the cylinder on the anode assembly were suspected the most probable locations where the rotation might have occurred, as indicated in Figure 3.24. Since the cylinder is the main conducting path of heat from the anode to the outside, thermal expansion and contraction during heating cycles could have caused sliding at the threads and resulted in the rotation of the anode as described above. However, this recipe did not prevent the anode motion, which was detected again afterwards. Further investigation pointed to the two setscrews that hold the anode against the L-bracket run into the anode through counter-bored

clear holes from the bottom, as shown in Figure 3.25. These two did not catch our attention during earlier examination since rotation or displacement was relatively unlikely when confined by two setscrews compared to those axes of rotations mentioned above. However, the clearance in the counter-bored holes does allow for relative motion at the interface, which could have been manifested during the temperature rise caused by the difference in the thermal expansion coefficients between stainless steel ($16 \times 10^{-6} \text{ m}/(\text{m}\cdot\text{K})$) and molybdenum ($5 \times 10^{-6} \text{ m}/(\text{m}\cdot\text{K})$).

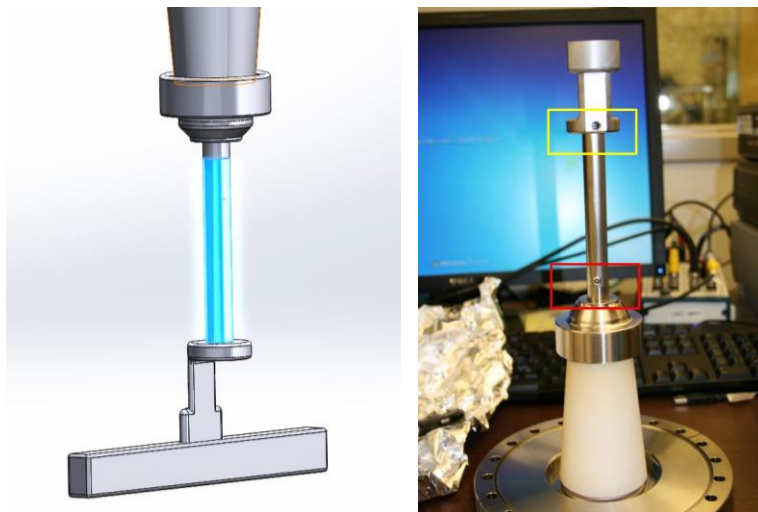


Figure 3.24 Left: SolidWorks drawing highlighting the cylinder that connects the anode to the HV feedthrough with two threaded joints on both ends. Right: two setscrews were added subsequently after the anode rotation was found, to prevent any rotation that might have occurred at the joints on the cylinder from the side towards the back wall of the vacuum chamber.

Furthermore, even though a lot of effort has been made to isolate the chamber from external motion, high frequency vibration from peripheral components of the system still exists which could have been the major cause of the anode rotation at high temperature during irradiation. In particular, the built-in turbo pump connects to a roughing pump through a long bellows. The roughing pump, though stands on the ground, introduces a significant amount of vibration that propagates to the system via the bellows. As the turbo pump hangs off the rear side of the vacuum chamber, such vibration would have a direct impact on the vacuum chamber and

the components inside. A hypothesis is therefore made which states that during the normal operation, a substantial amount of heat was generated while electrons bombarding the anode materials, and caused non-uniform thermal expansions in the anode body, the L-bracket, as well as the setscrews that are made of different materials. After switched off the electron emission, parts started to cool down and gradually contracted, during which small interspace emerged at the contacting surface between different parts during the different linear thermal expansion coefficients as well as the difference in the heat distribution. As a result, the originally tightened setscrews could become loose and therefore give room for anode rotation as induced by the vibration mentioned above.



Figure 3.25 SolidWorks drawing and a photograph (bottom view) of the anode assembly highlighting the two setscrews at the bottom of the anode.

To prevent the rotation from happening, changes were introduced to the design of the anode assembly. A modified L-bracket, (illustrated in Figure 3.26) was added to contact the back of the anode directly. The counter-bored holes were moved from the anode to the base plate on the L-bracket. This not only allowed for more convenient and secure installation of the setscrews, but also removed the potential adverse effect of gravity on the setscrews. However, this design does require tapping the thread hole in molybdenum which is relatively brittle.

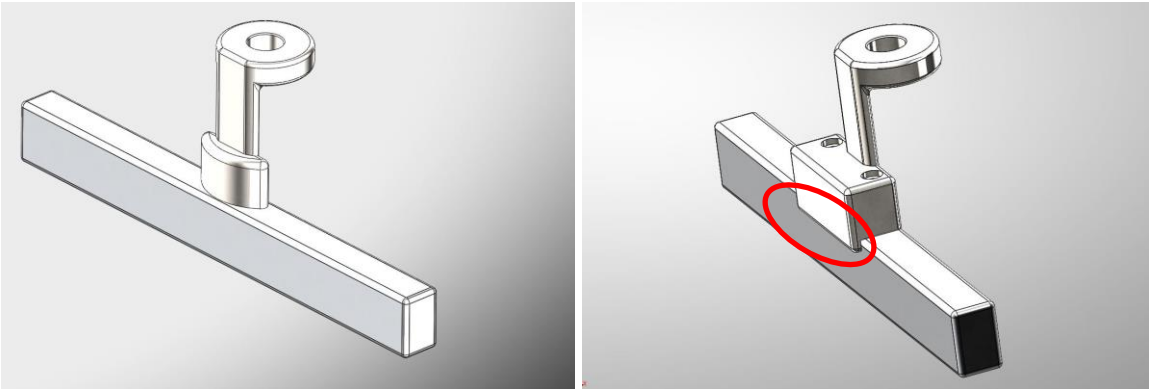


Figure 3.26 Left: original design of the anode assembly. Right: modified design of the L-bracket to avoid anode rotation.

Nevertheless, additional isolation of vibration and any externally introduced motion, as well as more efficient heat dissipation are desirable to ensure stable operation of the system. In the second-generation system *Apollo II*, the anode assembly is equipped with an active oil cooling device which could significantly improve the speed of heat transfer from the anode focal line. Thus the total output power of the system can be increased. The design of *Apollo II* has been detailed in the dissertation of Pavel Chtcheprov, and will be briefly introduced in Chapter 7.

REFERENCES

1. Zhou, O.Z. and S.X. Chang, *Compact microbeam radiation therapy systems and methods for cancer treatment and research*. 2010, A61N 5/10; A61B 6/03; A61B 6/00: U.S.
2. Schreiber, E.C. and S.X. Chang, *Monte Carlo simulation of a compact microbeam radiotherapy system based on carbon nanotube field emission technology*. *Med. Phys.*, 2012. **39**(8): p. 4669-78.
3. Hadsell, M., et al., *Pilot study for compact microbeam radiation therapy using a carbon nanotube field emission micro-CT scanner*. *Medical Physics*, 2014. **41**(6): p. 061710.
4. Hadsell, M., *The development and characterization of a first generation carbon nanotube x-ray based microbeam radiation therapy system*, in *Department of Physics and Astronomy*. 2013, University of North Carolina at Chapel Hill. p. 196-254.
5. Shan, J., O.T. Zhou, and J.P. Lu, *Anode thermal analysis of high power micro-focus CNT X-ray tubes for in-vivo small animal imaging*. *Medical Imaging 2012: Physics of Medical Imaging*, 2012. **8313**.
6. Sultana, S., et al. *Design and characterization of a carbon-nanotube-based micro-focus x-ray tube for small animal imaging*. in *SPIE Medical Imaging*. 2010. International Society for Optics and Photonics.
7. Bräuer-Krisch, E., et al. *Potential high resolution dosimeters for MRT*. in *AIP Conference Proceedings*. 2010.
8. Brauer-Krisch, E., et al., *Medical physics aspects of the synchrotron radiation therapies: Microbeam radiation therapy (MRT) and synchrotron stereotactic radiotherapy (SSRT)*. *Phys Med*, 2015. **31**(6): p. 568-83.
9. Akselrod, G.M., et al., *A novel Al₂O₃ fluorescent nuclear track detector for heavy charged particles and neutrons*. *Nuclear Instruments & Methods in Physics Research Section B-Beam Interactions with Materials and Atoms*, 2006. **247**(2): p. 295-306.
10. Sykora, G.J. and M.S. Akselrod, *Novel fluorescent nuclear track detector technology for mixed neutron-gamma fields*. *Radiation Measurements*, 2010. **45**(3-6): p. 594-598.
11. Belley, M.D., et al., *Fiber-optic detector for real time dosimetry of a micro-planar x-ray beam*. *Med Phys*, 2015. **42**(4): p. 1966-72.
12. Hartmann, B., M. Martisikova, and O. Jakel, *Technical Note: Homogeneity of Gafchromic EBT2 film*. *Med. Phys.*, 2010. **37**(4): p. 1753-1756.
13. *Gafchromic Dosimetry Media, Type EBT-3*. Available from: http://www.ashland.com/Ashland/Content/Documents/ASI/Other-Medical/EBT3_Specifications.pdf.

14. Desroches, J., H. Bouchard, and F. Lacroix, *Technical note: potential errors in optical density measurements due to scanning side in EBT and EBT2 Gafchromic film dosimetry*. Medical physics, 2010. **37**(4): p. 1565-1570.
15. Ma, C.M., et al., *AAPM protocol for 40-300 kV x-ray beam dosimetry in radiotherapy and radiobiology*. Med Phys, 2001. **28**(6): p. 868-93.

CHAPTER 4: IMAGE GUIDANCE FOR MICROBEAM RADIATION THERAPY

4.1 Motivation

The outcome of radiation therapy greatly relies on the conformality and accuracy in radiation dose delivery. In addition to the revolutions in conformal dose delivery techniques, such as intensity-modulated radiation therapy and stereotactic radiosurgery, advances in image guidance have contributed significantly to the evolution of modern radiation therapy. Cutting-edge imaging techniques or tools can reduce the uncertainties in target definition and patient positioning, therefore improve the agreement between treatment planning and actual treatment delivery. The precision and accuracy in treatment delivery can be largely optimized, which in turn reduces the unnecessary exposure of healthy tissue during radiation therapy [1]. On-board image guidance is inevitably essential in preclinical and clinical MRT where extremely high radiation dose is delivered by radiation beam that is in the microscopic range in width.

Previously, image-guided protocols were not implemented in most of synchrotron based MRT preclinical experiments. A large area is typically covered (in the order of $10\text{ mm} \times 10\text{ mm}$) by mechanically scanning the mouse brain through the microbeam arrays, to ensure a complete coverage of the tumor target. In this method, the ratio of tumor volume to the irradiated brain volume was estimated to be only about 6%, and therefore a very large amount of normal brain was unnecessarily enclosed in the irradiation field where the heaviest damage was seen [2]. X-ray radiography was utilized in several recent studies either to identify the tumor cell injection point [3] or to locate specific skull landmarks for homogenous irradiation of brain regions [4].

Direct localization of the target was not achieved due to the limited tumor contrast in planar X-ray imaging without contrast enhancement. Therefore, the normal tissue sparing effect of microbeams is to a great extent compromised and a true evaluation of the overall therapeutic outcome of MRT cannot be readily obtained.

Implementation of on-board imager and dedicated protocols for image-guided microbeam delivery are critical steps in the development of compact image-guided microbeam delivery system, and these must be completed before the system can be fully commissioned for preclinical studies on small animal models. A great amount of effort has been made to fulfill this goal including physical component design and integration, methodological development, and performance validation. These efforts are described in this and the following chapter.

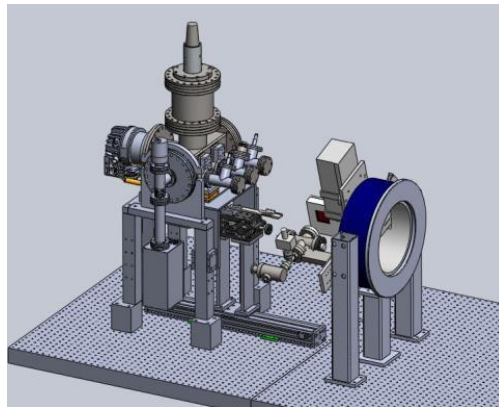


Figure 4.1 SolidWorks design of a compact system for micro-CT guided microbeam radiation therapy.

4.2 Implementing Image Guidance for Microbeam Delivery

4.2.1 Construction of the imaging system

Planar X-ray radiography and high-resolution CT are the two most frequently used imaging modalities in IGRT in the clinic due to the high accuracy and precision in beam positioning, as well as high compatibility with the treatment machine (little or no field interference). Our lab has previously demonstrated the technology of developing micro-CT

scanner with a CNT field emission source. A plan to integrate a micro-focused CT scanner with the microbeam irradiator was therefore made to employ the clinical practice as well as the established technology readily available in our lab. The design of concept is illustrated in Figure 4.1.

Table 4.1 Characteristics of the three cathodes in the micro-focused tube of the CT scanner

Parameters	Cathode 1	Cathode 2	Cathode 3
Cathode size (mm)	2.35×0.5	1.18×0.25	2.35×0.5
Optimized focal spot size (μm)	81×112	65×64	98×113
Highest anode current (mA)	2.00	0.33	2.00
Transmission rate (TR)	54%	44%	54%

The CNT-based micro-CT scanner followed the main features of design with a stationary sample, reported previously by Cao et al [5]. The core of the scanner is a micro-focused X-ray tube (body dimension $300 \text{ mm} \times 200 \text{ mm} \times 70 \text{ mm}$) based on CNT field emission sources (XinRay Systems Inc., NC, USA). Three pairs of CNT cathodes and tungsten targets are incorporated in this scanner for producing different focal spot sizes and flux. The tube was originally built with a 1 mm thick aluminum window which was later replaced with a 0.2 mm thick beryllium window due to vacuum issues. The characteristics of the cathodes are listed in Table 4.1. A miniature ion pump was attached to the micro-focused tube from the back via a CF flange. The X-ray tube is mounted on a rotary gantry (One-circle goniometer, model 430, HUBER, Germany). The image sensor used in the scanner is a CMOS based flat panel detector (model C7921CA-02, Hamamatsu Photonics K.K., NJ) with a $5 \text{ cm} \times 5 \text{ cm}$ active area and a pixel size of $50 \mu\text{m} \times 50 \mu\text{m}$. The X-ray tube and detector are mounted on opposite sides of the goniometer with the detector surface in parallel to the X-ray window. Other parts that are fixed

on the gantry include the anode HV power supply, the ion pump controller, and two focusing power supplies. These components are mounted so that the weight distribution on the goniometer is well balanced. Minor modifications have been made to the original designs mainly in the base plates for mounting the X-ray tube and the detector to the goniometer. The gantry is mounted on the optical table on the side of the microbeam irradiator, facing the rear side of the turbo pump. Other control electronics for the micro-CT are organized on a rack located outside the shielded enclosure. Photographs of the micro-CT scanner and the control console are shown in Figure 4.2. This cone-beam micro-CT scanner operates at 50 kVp and up to 2 mA tube current. Objects are placed on a stationary sample holder that is positioned in the radiation field, and the gantry rotates the source-detector pair around the stationary object to collect images in a step-and-shoot fashion. High resolution CT images of hearts or lungs in free-breathing animals can be obtained through respiratory and cardiac gated imaging, as demonstrated previously [5, 6].

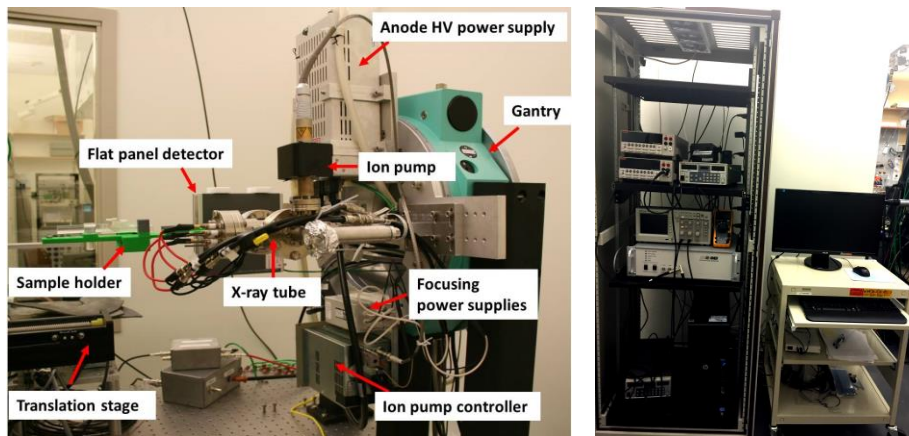


Figure 4.2 Left: A photograph of the micro-CT scanner built on the side of the microbeam irradiator, with key components indicated with red arrows. The gantry stands on top of the optical table, facing the back side of the turbo pump on the microbeam irradiator. Right: control console for the micro-CT outside the shielded enclosure.

The direct transport of patient (animal/sample) between the imaging system and the microbeam irradiator is achieved by a high-precision translation stage (96.5 mm travel range, 76 μm line accuracy, motor-drive BiSlides, Velmex Inc., NY) that connects both systems. A sample

stage has been designed and built to attach on top of the translation stage. Samples holders or animal positioning devices are fixed on the sample stage before imaging and treatment.

4.2.2 Integration of the IGMRT system

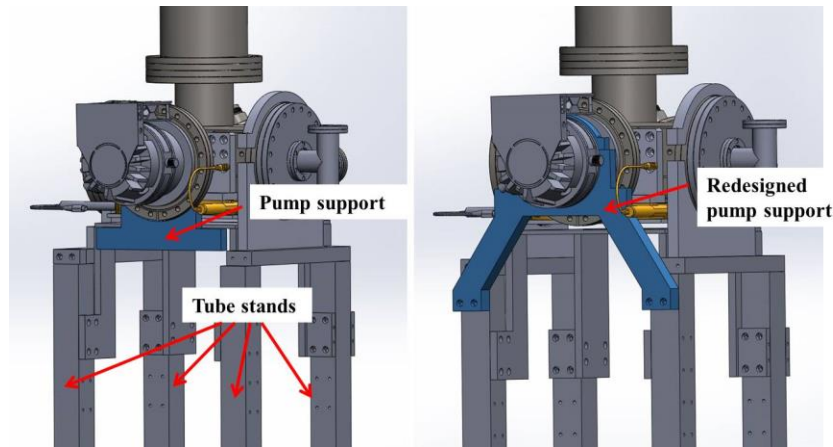


Figure 4.3 Illustration of the changes made to the turbo pump support (highlighted in blue color) in the microbeam irradiator, and the extended tube stand. Drawing on the left is the original design, while the one on the right demonstrates the modification.

After the construction of the micro-CT scanner was completed, a detailed examination and calculation were performed mainly in the designs and dimensions of the microbeam irradiator and the micro-CT scanner. The purpose was to identify and remove potential barriers or incompatibilities (conflicts) for the two systems to operate and execute collaboratively after integration, with additional consideration of the feasibility and simplicity of the workflow. Main changes that were made mostly to the designs of two parts in the microbeam irradiator after the thorough evaluation. First of all, the tube stands (as indicated in Figure 4.3) were extended in length so the entire vacuum chamber and the attached components were elevated by 8 mm. This change allowed for more space in animal handling and adjustment in the radiation field underneath the collimator. More importantly, it raised the height of irradiation entrance surface to be comparable with the imaging field of view (lined up with the axis of rotation in the CT

scan). Therefore, no major adjustment in the sample height would be needed between imaging and radiation treatment. In order to ensure steady translation of the sample between the imager and the irradiator, the turbo pump support in the back of the vacuum chamber was redesigned as shown in Figure 4.3. The benefits with the new design are two-fold. Firstly, more clearance has been created for the translation of sample stage between the two systems which has been proved critical in the animal experiments. Secondly, the newly designed pump support contains two parts that are clamped together around the turbo pump, and therefore holds the turbo pump in a steadier way. It can reduce the stress imposed on the connection to the vacuum chamber substantially, and it can limit the vibration transmitted from the turbo pump to the vacuum chamber.

In addition, the relative position between the imaging system and the irradiator was adjusted so that the axis of rotation of the rotary gantry was approximately aligned with the mid-line of the microbeam. Separation between the two systems was determined mainly to provide sufficient space for animal positioning and loading, within the travel of the translation stage.

4.2.3 Design of the animal positioning device

Patient immobilization is a key step in image-guided radiation therapy and to a great extent determines the accuracy in dose delivery. Proper and secure positioning is even more critical and challenging as body motions and displacement of internal organs are more common and severe in small animal models such as mice and rats. Dedicated animal positioning devices have been developed for different purposes of studies, and for accommodating different types and sizes of animals. Shown in Figure 4.4 (left) is the customized mouse holder particularly for brain irradiations, designed based on the anatomy of the young adult mice. This device is assembled with two separate parts, i.e. the base plate and the nosecone housing. The base plate

provides support of the mouse body, and fixation to the head through ear bars. Accommodation for the pressure sensor is also included on the base plate, for monitoring the respiration during imaging and treatment. Attached to the top is the housing for anesthesia delivery nosecone as shown in Figure 4.4 on right. A looped nylon wire is attached to the front of the nosecone as teeth clamp. Isoflurane from the gas vaporizer (outside the shielding enclosure) is fed in from the top, while excess gases are removed through the wider tubing that is attached to the rear end of the nosecone and absorbed by the gas filter canister (Omnicon F/Air). As illustrated in Figure 4.5, the mouse is typically placed in the prone position on the base plate. The ear bars, nosecone and the teeth clamp altogether provide 3-point immobilization and stereotactic placement of the mouse head. The position of the nosecone is adjustable along both x and y-axis, to ensure a steady and conformable positioning of the mouse head. Setscrews are installed after proper immobilization is completed. The pressure sensor is placed underneath the abdomen of the mouse. Additional tapes and gauze are used as needed.

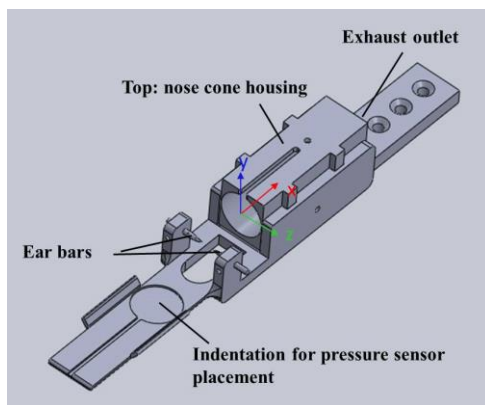


Figure 4.4 SolidWorks drawing of the home-made mouse holder. The design includes two parts, i.e. the main body of the holder and a nosecone holder attached on top. [7].

The mouse holder assembly including the ear bars and setscrews were fabricated out of ABS plastic through 3D printing. The main design has been modified for different imaging and

irradiation purposes. Figure 4.6 on the left demonstrates the drawing of the modified holder for positioning mouse pups during brain irradiation. The ear bars are replaced with a neck support in this design. Two small holes are drilled on both sides of the neck support to feed the rubber band that is used for fixing the mouse head in place.

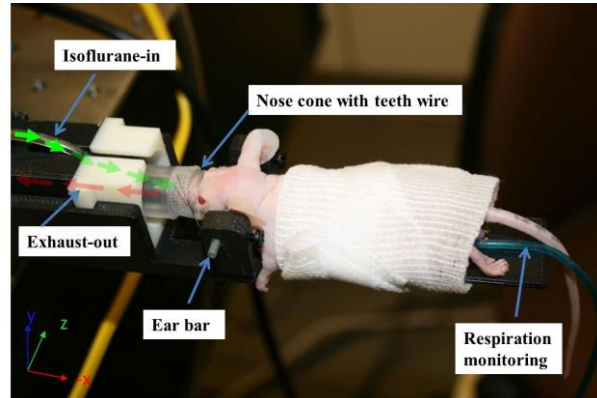


Figure 4.5 A photo of a nude mouse positioned on the mouse holder under anesthesia.

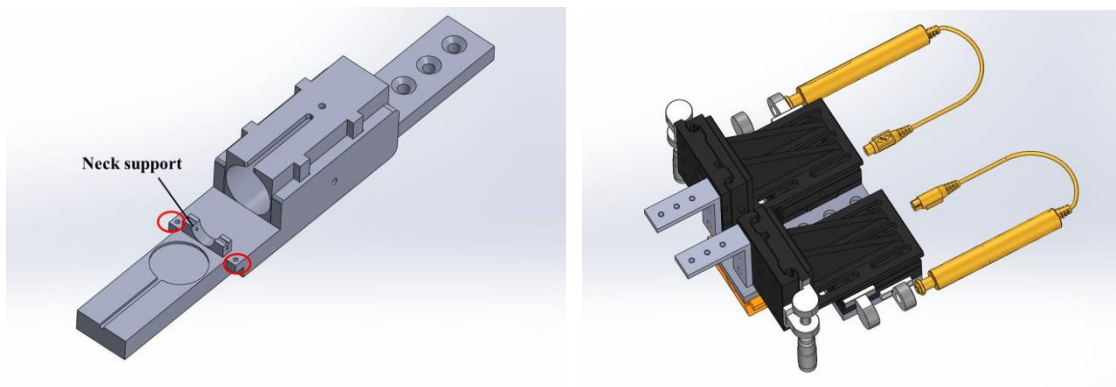


Figure 4.6 SolidWorks drawings of the modified mouse holder for P12 mouse pups (left); and the double-stage (right).

Animal positioning and immobilization are usually performed on the optical table. Afterwards, the mouse holder can be loaded and fixed on the sample stage as mentioned above. The sample stage has two vernier micrometers (0 – 25 mm measuring range) installed to allow for manual adjustment along both z and y axes. Adjustment along x-axis is made by the

motorized BiSlide translation stage. A special double-stage (Figure 4.6) has also been designed and constructed later for positioning of two mouse holders side by side in the double-mouse image-guided MRT studies, as detailed in chapter 5.

4.2.4 Peripheral components

The respiration rate recorded by the pressure sensor is monitored through *Biovet* (m2m Imaging Corp., HO) user interface installed on the control PC of the micro-CT. Another monitor has been installed inside the shielded chamber for parallel monitoring during the animal handling process. *Biovet* also allows for ECG monitoring in parallel with the respiration monitoring.

A complete setup for animal anesthesia and monitoring are installed including two vaporizers (SurgiVet®, Smiths Medical, MA), an induction chamber (SurgiVet®), compressed oxygen (medical grade, Airgas National), and bottled isoflurane (Phoenix™), tubings and anesthesia gas filter canister (Omnicon F/Air). Annual calibration of the vaporizers has been routinely performed.

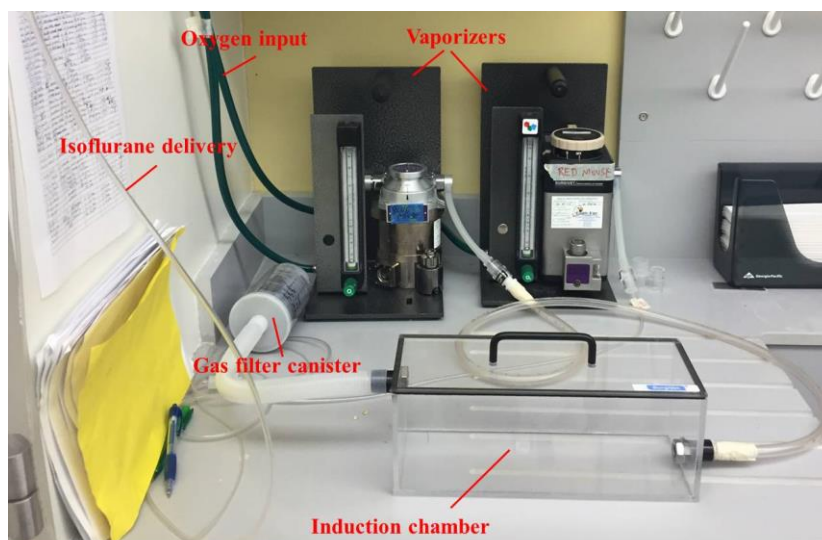


Figure 4.7 A photo of the anesthesia setup equipped to the CNT-MRT system for small animal studies. A high speed computer workstation is also used for image processing and image reconstruction. A MATLAB program based on the Feldkamp algorithm and a commercial

software package COBRA (EXXIM Computing Corp., CA) are used for CT image reconstruction [5, 8].

4.2.5 System calibration and testing

Complete calibration procedures for the microbeam irradiator were described in the previous chapter. The micro-CT scanner was also fully conditioned and characterized. The X-ray tube to detector distance was determined based on the dimension of the mouse positioning setup, and the imaging geometry was fully calculated and calibrated using a two-ball phantom following the procedure outlined by Noo et al [9]. Up till this point, the development of the physical components for the compact IGMRT system was completed. The entire setup includes a CNT-based micro-CT scanner, a CNT-based microbeam irradiator, dedicated patient (animal) positioning and translation system, anesthesia equipment, and respiration monitoring devices. Photographs of the IGMRT system built on the optical table and the control units outside the shielding chamber are shown in Figure 4.8.

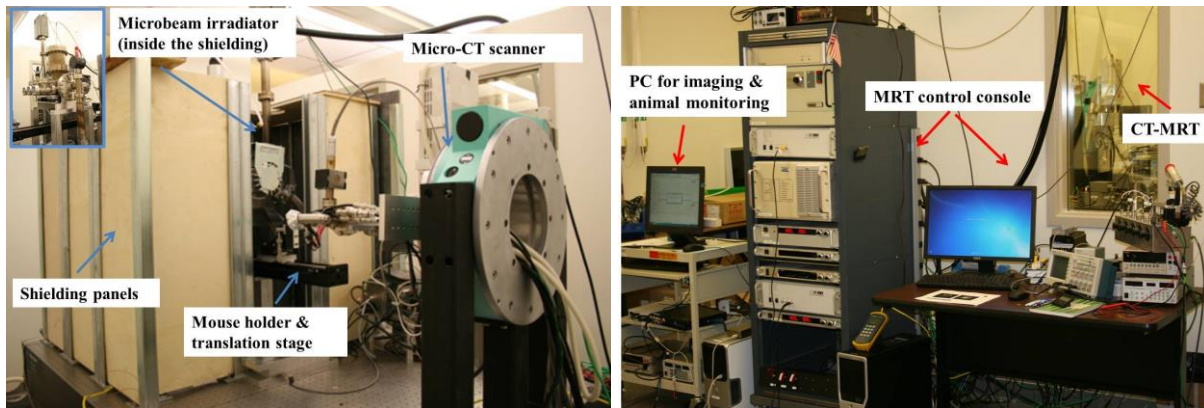


Figure 4.8 A photograph of the CNT-based image-guided microbeam radiation therapy system constructed on an optical table in our lab at the University of North Carolina at Chapel Hill.

REFERENCES

1. Xing, L., et al., *Overview of image-guided radiation therapy*. Medical Dosimetry, 2006. **31**(2): p. 91-112.
2. Laissue, J.A., et al., *Neuropathology of ablation of rat gliosarcomas and contiguous brain tissues using a microplanar beam of synchrotron-wiggler-generated X rays*. Int. J. Cancer, 1998. **78**(5): p. 654-660.
3. Romanelli, P., et al., *Synchrotron-generated microbeam sensorimotor cortex transections induce seizure control without disruption of neurological functions*. PLoS One, 2013. **8**(1): p. e53549.
4. Serduc, R., et al., *In vivo pink-beam imaging and fast alignment procedure for rat brain lesion microbeam radiation therapy*. J. Synchrotron Radiat., 2010. **17**(3): p. 325-31.
5. Cao, G., et al., *Prospective-gated cardiac micro-CT imaging of free-breathing mice using carbon nanotube field emission x-ray*. Medical Physics, 2010. **37**(10): p. 5306-5312.
6. Lee, Y.Z., et al., *Prospective respiratory gated carbon nanotube micro computed tomography*. Acad Radiol, 2011. **18**(5): p. 588-93.
7. Hadsell, M., *The development and characterization of a first generation carbon nanotube x-ray based microbeam radiation therapy system*, in *Department of Physics and Astronomy*. 2013, University of North Carolina at Chapel Hill. p. 196-254.
8. Feldkamp, L., L. Davis, and J. Kress, *Practical cone-beam algorithm*. JOSA A, 1984. **1**(6): p. 612-619.
9. Frédéric, N., et al., *Analytic method based on identification of ellipse parameters for scanner calibration in cone-beam tomography*. Physics in Medicine and Biology, 2000. **45**(11): p. 3489.

CHAPTER 5: IMAGE-GUIDED MICROBEAM DELIVERY IN SMALL ANIMALS

5.1 Motivation

Upon completion of system construction, planning for small animal studies was initiated in order to evaluate the performance of the compact image-guided MRT system as a preclinical tool for microbeam radiobiological effect for brain cancer treatment, as well as to investigate the feasibility to translate the CNT source array technology for MRT clinical applications.

Comprehensive methods and protocols that address each critical step including tumor identification, animal immobilization, and beam positioning were to be established and validated. The accuracy and uncertainties had to be determined, before animal studies could be conducted to correlate any radiobiological responses with the treatment parameters.

The majority of work presented in this part was to establish an efficient and accurate method for targeted delivery of microbeam radiation in treating brain tumor bearing mice. Considering the size of the animal, the fine structures in its anatomy, and the limited size of the brain tumor, it is technically challenging to accurately align the narrow microplanar beams with the tumor target. Planar X-ray imaging or CT can quickly capture bone structures but are not ideal for brain tumor imaging due to the low soft tissue contrast. A considerable dose of contrast agent is often required, which on the other hand causes nephrotoxicity and complicates the treatment outcome. Magnetic resonance imaging (MRI) provides excellent tumor contrast non-invasively, and therefore is often used as the gold standard in brain tumor diagnosis. Hence the feasibility of combined MRI and X-ray imaging for MRT treatment guidance dedicated for brain

tumor bearing mice was investigated. Tumor diagnosis and delineation was performed with MRI, while skull structures and landmarks were identified with the micro-CT scanner. The radiation beam delivery was planned afterwards based on the registered image of these two modalities.

For the image-guided microbeam irradiator, the feasibility of microbeam irradiation in different treatment configurations was evaluated, i.e. delivery of radiation from a unidirectional microbeam array to a mouse brain tumor and multi-array microbeam irradiation of a mouse brain tumor. Both of these two delivery methods rely on precise target delineation and accurate beam positioning with variations in certain procedures including animal re-positioning and additional imaging requirement. Dedicated protocols, validated which employed multi-modality image registration either in 2D or 3D space, were developed. With 2D registration, planar images of MR scan and X-ray radiographs from the same orientation were obtained for target identification and beam planning. This method allows for a quick capture of targeted features in unidirectional beam delivery, and allow for irradiating two mice simultaneously using a double-mouse setup to improve the experimental throughput. In contrast, more detailed target localization with a higher accuracy is desired in multi-directional microbeam delivery. This requires at least two-view planar X-ray imaging and MRI with 2D registration, or complete scans of 3D MRI and CT and 3D image registration. Detailed procedures and the evaluation of the accuracy and consistency of each method are presented in the following sections.

Parts of the main results for the 2D image-guided MRT has been published in as “Image-guided microbeam irradiation to brain tumor bearing mice using a carbon nanotube X-ray source array” in *Physics in Medicine and Biology* [1]. Methods and protocols of image-guided microbeam radiation therapy (IGMRT) discussed in this chapter have been used for subsequent preclinical studies, including those described in chapter 6.

5.2 Delivery of Single Array Microbeams in Mouse Brain with 2D Image Guidance

As described in Chapter 3, the microbeam radiation field is around 300 μm wide, and over 160 mm long without conformal collimation in the long axis. An array of microbeams would transverse the entire brain as it passing through the tumor target as illustrated in Figure 5.1. Unnecessary dose to the rest of the mouse body should be avoided by delivering the beams from the top as the mouse is positioned in prone posture on the mouse holder. In the treatment space defined by the Cartesian coordinate system as indicated in Figure 5.1 the relative location of the tumor target with respect to the radiation beam needs to be determined prior to beam delivery. Since the z coordinate of the tumor location becomes irrelevant in beam targeting using such radiation configuration, a single projection in the sagittal view registered from a planar MR image and an X-ray radiograph would be sufficient to define the x and y coordinates of the tumor target.

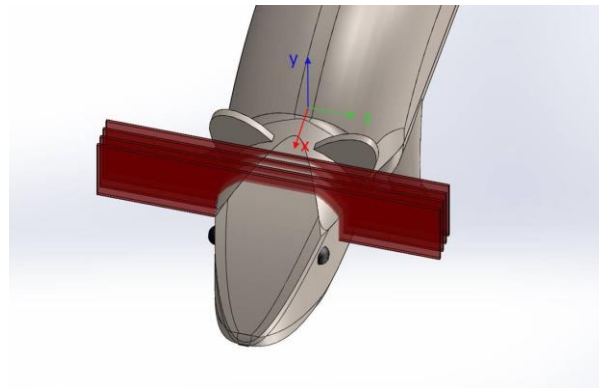


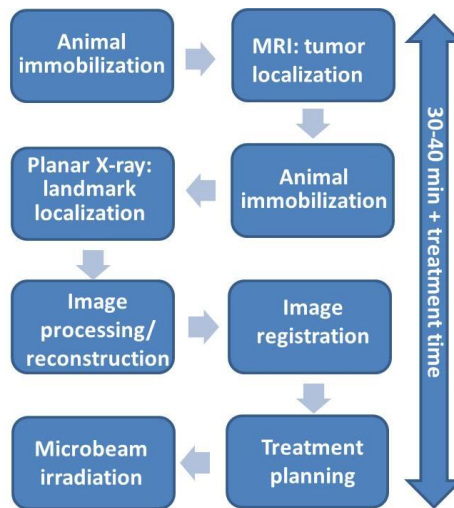
Figure 5.1 Illustration of a single array of microbeams irradiating the mouse brain. The relative locations of target, landmarks, and radiation field are defined by a Cartesian coordinate system as indicated.

5.2.1 Methods

The overall workflow is outlined in Table 5.1. Firstly, animals undergo MRI scans (9.4T MR scanner, Bruker BioSpin Corp., MA, USA) the day prior to MRT for tumor diagnosis and delineation. X-ray imaging is performed prior to treatment to capture the bone structures and

landmarks on the mouse bed. Animals are anesthetized and immobilized the same way on a customized mouse bed for both MRI and X-ray imaging. MR images and x-ray radiographs are registered using a 2D rigid-body method to present the tumor location relative to the skull and landmarks. With the landmarks pre-calibrated as a reference to the microbeam location, the registered images provide the tumor coordinates in the microbeam treatment space, and enable accurate delivery of microbeams to the tumor target. This entire procedure was first evaluated using acrylic phantoms. However a more thorough evaluation of the accuracy and consistency of the method was still required for brain tumor bearing mice. Therefore a feasibility study of the image-guided microbeam delivery to mouse brain tumors was conducted under the approval from the Institutional Animal Care and Use Committee at our the University of North Carolina.

Table 5.1 A flow chart illustrating the procedure of multi-modality image-guided microbeam radiation therapy in brain tumor bearing mouse models.



5.2.1.1 Tumor cell and animal preparation

Fourteen young adult (4 - 6 weeks old), male, athymic nude mice were used in this study. U87MG human glioma tumor cells were kindly provided by Dr. Ryan Miller's lab at UNC Department of Pathology. The tumor cells were cultured in Dulbecco's Modified Eagle's Medium

(DMEM) plus 1% Fetal Bovine Serum (FBS) before being collected for injection. Three weeks before irradiation, and with stereotactical guidance, 2×10^5 cells in 5 μ l serum-free medium were injected intracranially into the right forebrain — 1mm anterior, 2.5 mm lateral, and 4 mm down to the bregma — to induce brain tumor growth in the mouse. The cell preparation and tumor inoculation were carried out by the Biomedical Research Imaging Center (BRIC) at UNC.

5.2.1.2 Imaging and beam planning

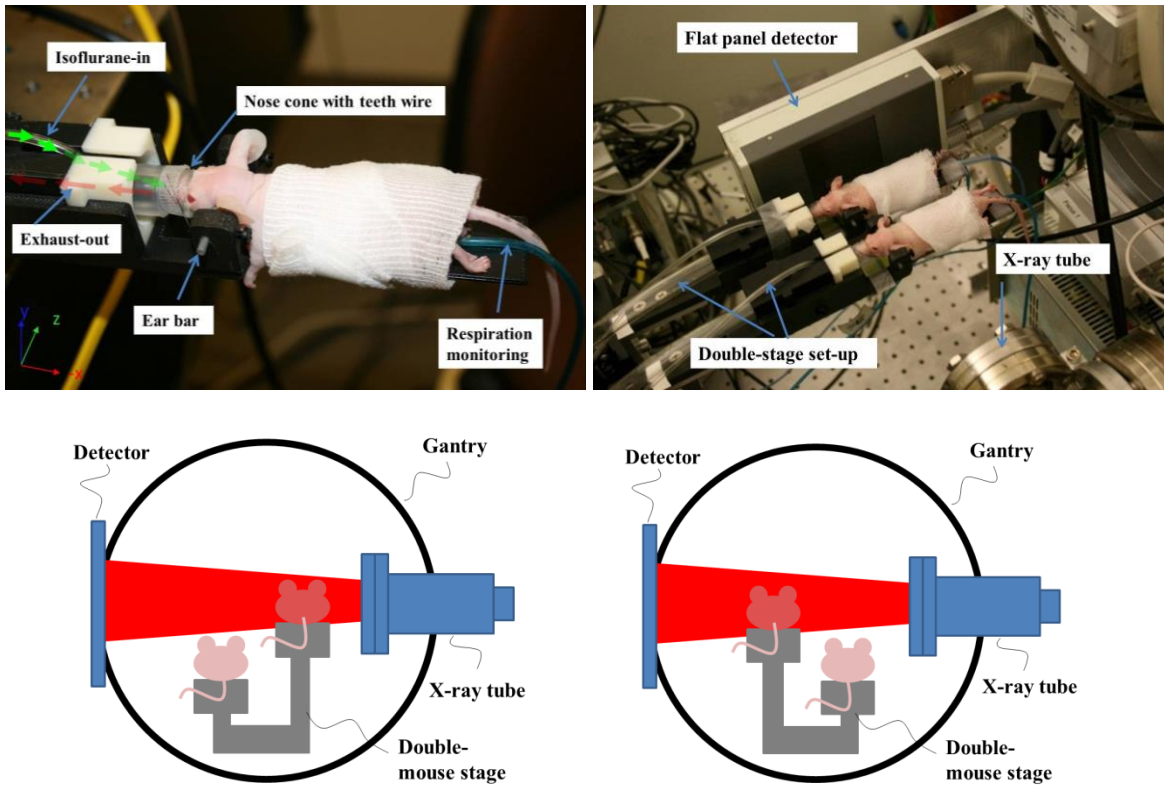


Figure 5.2 Top row: on the left is a picture of animal immobilized on the customized mouse holder under anesthesia, while on the right is a picture showing the setup of double-mouse imaging. Bottom row: illustrations of two mice imaged by the micro-CT scanner one after the other, in the image-and-shift manner. Pictures are reprinted with permission from Zhang *et al. Physics in Medicine and Biology* 59, 1283-1303 (2014) [1].

The animals were housed with care for about three weeks after cell injection to allow for tumor development until the average tumor size reaches about 1.5 – 3 mm in diameter. Mice were transported to the small animal imaging facility at BRIC for MR imaging. This was

performed using a 9.4 Tesla MR scanner (Bruker BioSpin, Inc. Billerica, MA). T2-weighted images were acquired using a Rapid Acquisition with Refocused Echoes (RARE) sequence with an echo spacing-to-recovery time ratio (TE/TR) of 22/3406, 256×256 matrix size, 0.5 mm slice thickness, and 100 micron sagittal and coronal in-plane resolution. The tumors were delineated in T2w images with hyper-intense signal. The MR images used for registration were created from the sagittal images. The central three slices near the brain midline were averaged to form a sagittal projection image. This projection was later used to align with the sagittal X-ray projection of the same mouse. The tumor location was projected to the center slice. For all imaging and MRT treatment procedures, the mice were anesthetized with 1% - 2.5% isoflurane in medical-grade oxygen at 0.8 or 1 L/min flow rate.

After MRI, the mice were transported to the MRT lab on the day of irradiation. While under anesthesia, the mice were first immobilized in the prone position on the customized holders (Figure 5.2). The ear bars, nose cone and the teeth clamping altogether ensured immobility of the sedated mice. Two mice were immobilized on two separate mouse beds, which were then mounted side by side on the double-stage within the micro-CT imaging field, as shown in Figure 5.2. Planar X-ray images of the two mice were taken using the micro-CT scanner at 45 kVp and 0.024 mAs per projection. Imaging of the mice was performed one at a time in an image-and-shift manner, as illustrated on the top row in Figure 5.2. The actuator and micrometer attached to the mouse bed positioned the head of the mouse being imaged at the center of the detector field of view, while the other mouse was kept outside of the X-ray beam pathway. X-ray projections were acquired from the same orientation (sagittal view) as that in the MRI, with the animals positioned in the same way as well with the same immobilizing device as described earlier in this chapter. Afterwards the mouse imaged first was shifted out from the field of view;

the other was moved in, and imaged in the same manner. The projections were corrected with dark and blank images using a *MATLAB* (MathWorks Inc., Natick, Massachusetts, US) program. For X-ray imaging, the ear bars on the mouse holder were used as the fiducial landmarks because they were easily calibrated to both the microbeam position and the brain structures of the mouse.

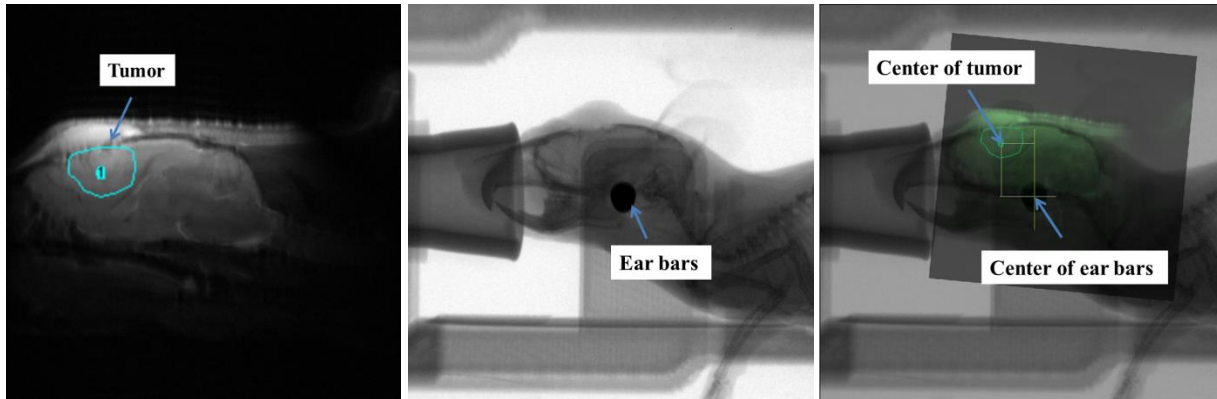


Figure 5.3 Left: MR image of the mouse brain with the targeted tumour circled. Middle: X-ray projection of the same animal showing the landmark ear bars and skull features. Right: X-ray projection registered with MR image showing the relative position of the tumour and ear bars. Pictures are reprinted with permission from Zhang *et al. Physics in Medicine and Biology* 59, 1283-1303 (2014) [1].

5.2.1.3 Image processing and registration

Planar X-ray images were firstly processed for background subtraction, and then calibrated in size with the MR images before registration could be performed. The sagittal MR images and corrected X-ray images were then aligned manually through rigid-body registration methods with a commercial image processing software (*Photoshop*, Adobe Systems Inc., San Jose, California U.S.) and *ImageJ* (Public Domain, Developed by Wayner Rasband, NIH). Alignment was performed based on the anatomy of the mouse brain [2]. Features including the bregma and cerebellum were used as major references for registration. The registration process is illustrated in Figure 5.3. Once the images were registered, the coordinates of the tumor with respect to the skull and landmarks on the mouse bed can be directly visualized and determined. The distance from the tumor center to the ear bars, Δx_1 , was measured from the registered images in both anterior-posterior and superior-inferior directions, as shown in Figure 5.4. Since the two

ear bars may not be concentric in the projection images depending on their location in the image and the differences in magnification, the midpoints of two ear bars were averaged and used as the ‘center of ear bar’.

5.2.1.4 Microbeam alignment and irradiation

Figure 5.4 shows the geometrical parameters that need to be determined in order to deliver the microbeam to the tumor accurately. Since the planar microbeams are delivered in the y-z plane and no conformal collimation is used in the current setup, only the relative distances in the x direction are needed. The beam position, i.e. the microbeam entrance position with respect to the ear bars, has to be calibrated on a daily basis. To do this, first Δx_2 was recorded, with *Gafchromic* film placed on top of the mouse holder. A low dose single microbeam was delivered to the film for calibration purposes. The distance between the center of the microbeam and Δx_3 , the center of ear bars, was measured with calipers. With the tumor location relative to the ear bars, Δx_1 , determined from registration, the distance between the tumor and the microbeam entrance point for the mice pair was therefore calculated by the summation of Δx_1 , Δx_2 , and Δx_3 , with the signs assigned accordingly.

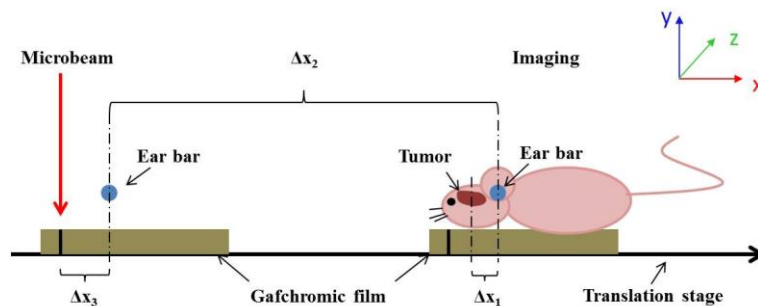


Figure 5.4 Diagram showing the geometric relations between the targeted tumor, landmark, and microbeam locations. The z-direction is perpendicular to the paper plane. The microbeam plane is in the y-z plane. Δx_1 is the distance from the tumor to the ear bars measured in the registered image, Δx_2 is the distance of translation from the MRT chamber to the micro-CT, and Δx_3 is the distance between the center of the ear bar and the alignment microbeam track measured during microbeam alignment. The mouse holder with the *Gafchromic* film was first irradiated for beam alignment, as shown on the left, and then translated to the right, followed by mouse positioning and X-ray imaging. Pictures are reprinted with permission from Zhang *et al. Physics in Medicine and Biology* 59, 1283-1303 (2014) [1].

Once plans for microbeam delivery were determined, the mice were translated from the imaging location to the irradiation site, ready for treatment. The number of microbeams, beam pitch, and the beam delivery locations on the tumor site, were decided based on the registered image and tumor size (as illustrated in Figure 5.5 on left). For this targeting study, we chose various dose levels and different numbers of microbeams for the animals (as assigned below), which was also investigated in another study for cellular responses. The microbeam irradiator was running at a constant anode voltage of 160 kV, producing a microbeam of 280 μm full-width-half-maximum (FWHM) at the animal head entrance plane. The average dose rate at the entrance plane was 1.16 Gy/min, determined as noted before. In total, fourteen tumor bearing mice were irradiated in seven groups, two mice at a time following the procedures described above, as shown in Figure 5.5 on right.

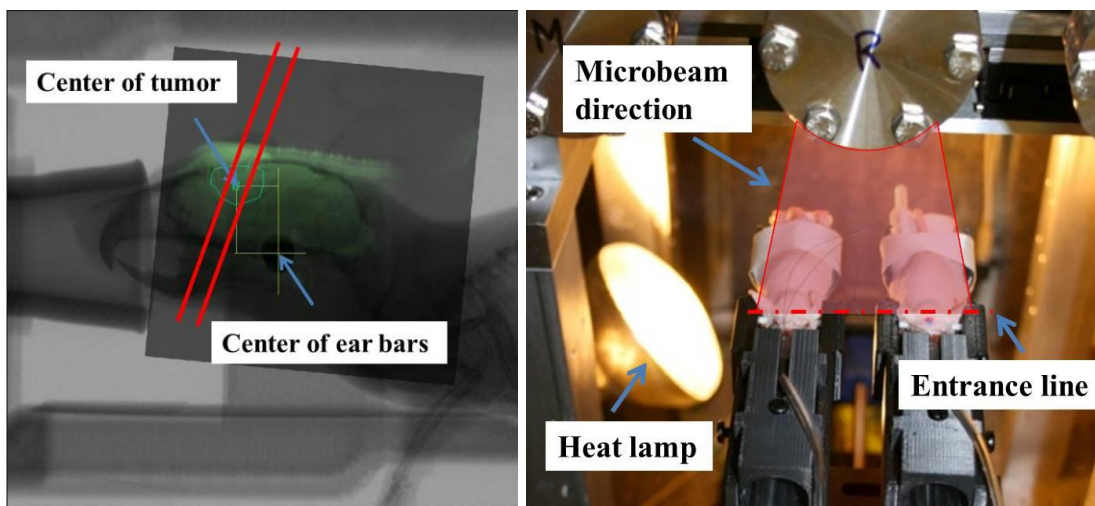


Figure 5.5 Left: illustration of the beam planning procedure based on the size and location of the tumor from the registered image. Regions in green color are from the MR layer showing soft tissue contrast, while bony structures and the mouse bed presented in the planar X-ray images are overlapped on top. The red lines indicate the microbeams penetrating through the tumor target (outlined in darker green). Microbeams project at an 8° angle from collimator tile as described in Chapter 3. Right: a picture of the double-mouse setup in the microbeam irradiator, ready for treatment. The pink plane indicates the microbeam entrance plane. Also noticeable is the heat lamp placed inside the lead chamber. The heat lamp switch is controlled electronically to maintain a proper body temperature in the mice. Pictures are reprinted with permission from Zhang *et al. Physics in Medicine and Biology* 59, 1283-1303 (2014) [1].

The first pair of mice was irradiated by a single microbeam of 138 Gy entrance dose, targeted at the center of the tumor. The second pair of mice was irradiated by two parallel

microbeams with center-to-center distance of 900 μm . A 900 μm center-to-center distance was chosen to maintain a relatively high PVDR with 280 μm beamwidth, and to achieve good coverage of the tumor area. The prescribed entrance dose for each microbeam was about 108 Gy. Between the two microbeams, the first was targeted at the center of the tumor while the second was targeted 900 μm away. The remaining 5 pairs of mice were irradiated by three microbeams, with a 900 μm pitch, delivering 48 Gy at the entrance of each microbeam.

5.2.1.5 **Beam verification using immunohistological staining**

To evaluate the targeting accuracy and the tumor cell response, $\gamma\text{-H2AX}$ immunofluorescence staining was used as a quantitative biomarker of radiation-induced DNA double-strand breaks (DSB). This process confirms the delivery of microbeams through the tumor tissue sections post irradiation. The mice were euthanized at various time points (1 hr, 4 hrs, 24 hrs, 48 hrs, and 7 days) post-MRT. Their brains were collected and fixed in formalin. The fixed brains were cut in half along the midline and embedded in paraffin. Before tissue sectioning, the distance between the center midline to the targeted tumor plane in the sagittal view that was used for treatment planning was first measured from both coronal and sagittal MR images. This distance was then used in sectioning to determine the tumor location on the paraffin-embedded brain hemisphere, taking into account a 20% shrinkage rate from the dehydration process [3]. Ten slices of tissue each 5 μm thick were collected in the sagittal plane, perpendicular to the microbeams, near the target locations. One of the tissue slices was used for $\gamma\text{-H2AX}$ staining. The staining procedures followed the published protocol [4]. Briefly, the tissue section was de-paraffinated, rehydrated, antigen-demasked by citrate buffer, and then incubated with the primary antibody (Phosphohistone H2AX Rabbit anti-mouse antibody, Cell Signaling Technology Inc.) for 60 min. This was followed by incubation with the secondary antibody with

Cy5 Tyramide and DAPI counter-staining on the nuclei. The section was then scanned with a fluorescence slide scanner system (Scanscope FL scanner, Aperio Inc., Vista, CA) to obtain a whole brain slide image.

5.2.2 Results

5.2.2.1 Dose verification

Gafchromic EBT2 films were used throughout this study for qualitative verification of dose delivery. Films were placed after imaging and prior to treatment, at the entrance and exit planes of mouse head, as well as on the side wall of the ear bar pillars.



Figure 5.6 Pictures of the recovering animal on the mouse holders. As shown here, Gafchromic films were placed at the beam entrance, exit, as well as on the side of the mouse bed, to verify the delivered radiation dose and beam patterns.

Figure 5.6 showed the film positions and the recorded beam patterns after the MRT. All films were scanned in 48-bit color and at 2400 dpi using the V700 scanner following the handling procedures recommended by Ashland, Inc. Number of beams and c-t-c distances were confirmed in all films to be consistent with the prescription. The films irradiated by planned doses that fell into 0 - 60 Gy dose range were analyzed using triple channel dosimetry in *FilmQAPro*. The films from a tumor mouse treated with three microbeams with dose of 48 Gy/beam are shown in Figure 5.7. The FWHM of the dose profile was measured to be 280 μm at the entrance plane, which was consistent with our tube calibration results. The beam width

broadened to 380 μm at the exit plane underneath the mouse skull. The measured peak dose of each beam was consistent with the prescribed value as well. The PVDR was calculated from the following equation:

$$\text{PVDR} = \frac{D_{\text{peak}}}{D_{\text{valley}}}$$

D_{peak} and D_{valley} are the average doses measured at the center of peak, and the center of valley respectively. The average PVDR was calculated to be 16 ± 1 at the entrance plane, and reduced to 14 ± 1 at the exit plane.

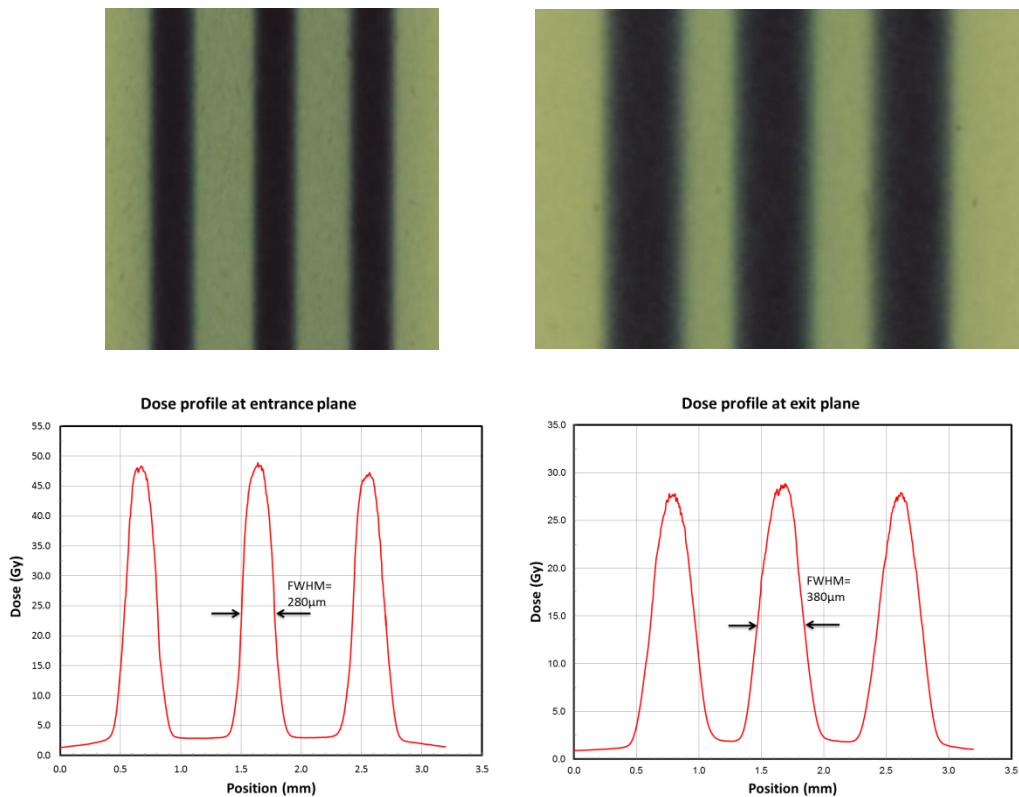


Figure 5.7 Beam patterns recorded by Gafchromic EBT2 films at the entrance (top left) and exit (top right) planes on the mouse head, and corresponding dose profiles (bottom) analyzed by FilmQAPro program (using multi-channel dosimetry). The beam width at the entrance plane is about 280 microns, and 380 microns at the exit plane. The PVDRs recorded for this animal were roughly 16 at the entrance plane, and 15 at the exit plane. Pictures are reprinted with permission from Zhang *et al. Physics in Medicine and Biology* 59, 1283-1303 (2014) [1].

5.2.2.2 Immunohistological staining

Figure 5.8 and Figure 5.9 showed the γ -H2AX stained images of the brain tissues from the irradiated animals. The γ -H2AX foci-positive cells shown as pink strips were clearly visible in the stained sections indicating radiation-induced DNA double-strand breaks. These patterns corresponded to the microbeam path through the tumor and normal tissues. The geometric center-to-center distance between two adjacent tracks was measured to be 800 μm , which matches with the prescribed beam pitch of 900 μm when taking into account the average 20% anisotropic shrinkage rate [3] of the paraffin embedded slice.

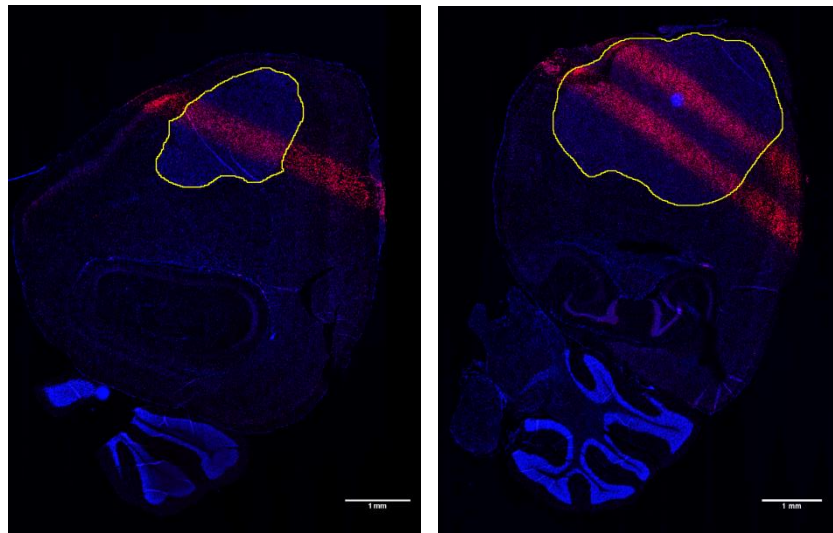


Figure 5.8 Fluorescence images of γ -H2AX stained mouse brain tissue slices after microbeam irradiation. The γ -H2AX foci-positive cells, shown as pink strips, correspond to the microbeam pattern. Areas circled in yellow are tumour targets. The images correspond to animal ID 1087 (left) that was treated with two microbeams with 109 Gy/beam, and 1089 (right) which received a single microbeam radiation with 138 Gy entrance dose. In both cases, microbeams were delivered right on target as planned.

Pictures are reprinted with permission from Zhang *et al. Physics in Medicine and Biology* 59, 1283-1303 (2014) [1].

The targeting error was first evaluated directly from the stained sagittal sections by measuring the horizontal displacement, Δx , from the center of the microbeam to the center of the tumor. Out of the 14 animals in this study, one was excluded due to cutting and staining mistakes. The average horizontal displacement Δx of the remaining 13 mice was approximately 454 μm . The values measured via this manner are listed in column 2 of

Table 5.2.

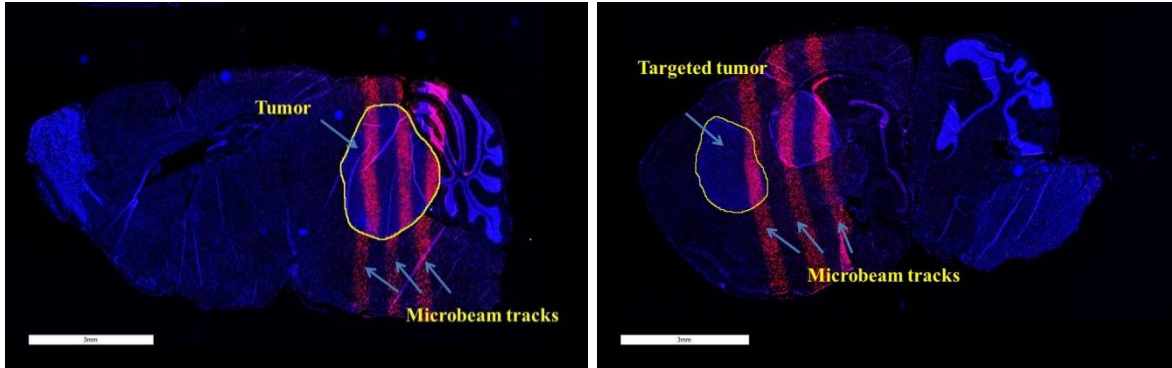


Figure 5.9 Comparison of the γ -H2AX stained mouse brain tissue slices from animal ID 1152 and ID 1149 both treated with three microbeams with 48 Gy/beam entrance dose. As labeled in the images, three planned microbeams were delivered on target for the case on left, while for the one right, two out of the planned three microbeams were delivered off-target. Pictures are reprinted with permission from Zhang *et al. Physics in Medicine and Biology* 59, 1283-1303 (2014) [1].

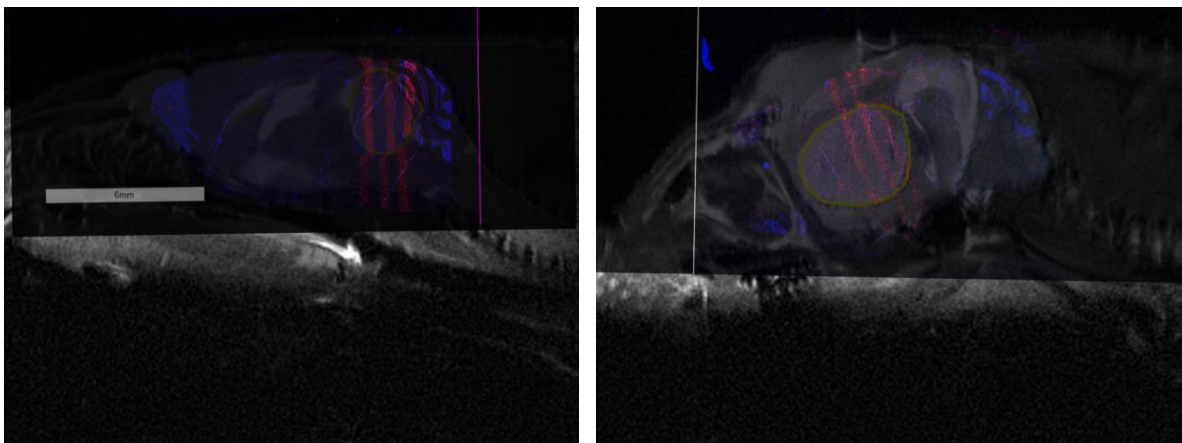


Figure 5.10 γ -H2AX stained, sagittal image registered with MR projection for the same slice of tissue, from two animals (Left: ID 1152 and right: ID 1145) irradiated with three microbeams of 48 Gy/beam. Microbeam tracks are the pink strips through the higher contrast tumour region, demarcated by the yellow circle. The targeting error was measured from the microbeam location to the targeted tumour center. Pictures are reprinted with permission from Zhang *et al. Physics in Medicine and Biology* 59, 1283-1303 (2014) [1].

Since the MR images were taken the day before MRT and the animals were euthanized at different time points post MRT, there might have been anisotropic tumor growth between the MRI and euthanization. This created difficulties in identifying the original target center in the stained section. The targeting accuracy was also evaluated by manually registering γ -H2AX stained image back to the corresponding pre-treatment MR sagittal images, as shown in Figure

5.10. The γ -H2AX stained image recorded the microbeams' positions while the MR sagittal image showed the original targeted tumor center. This alignment method is similar to the X-ray/MR image registration mentioned previously in this paper, except that here we used features in the brain and cerebellum instead of skull contour for alignment. The targeting errors Δx measured in this way are listed in column 3 of

Table 5.2.

Table 5.2 Summary of the uncertainties in beam targeting using the 2D image-guided MRT protocol. Pictures are reprinted with permission from Zhang *et al. Physics in Medicine and Biology* 59, 1283-1303 (2014) [1].

Animal ID	Dx from staining-only (mm)	Dx from registered histological images (mm)	Number of MBs with peak entrance dose per beam
1087	290	390	Two beams, 108 Gy/beam
1086	800	1000	Single beam, 138 Gy/beam
1089	10	50	Single beam, 138 Gy/beam
1123	100	100	Three beams, 48 Gy/beam
1122	80	330	Three beams, 48 Gy/beam
1141	830	660	Three beams, 48 Gy/beam
1140	300	440	Three beams, 48 Gy/beam
1145	660	790	Three beams, 48 Gy/beam
1151	100	100	Three beams, 48 Gy/beam
1150	1130	1600	Three beams, 48 Gy/beam
1153	90	100	Three beams, 48 Gy/beam
1152	230	140	Three beams, 48 Gy/beam
1149	1280	1280	Three beams, 48 Gy/beam
Average	454	537	--
Standard Deviation	417	482	--

5.2.3 Discussion

In total, 14 animals were irradiated using the combined X-ray/MRI image-guided MRT protocol described above. Due to tissue sectioning and staining errors, one mouse was excluded from the analysis. The histology data showed that 11 out of the remaining 13 animals

successfully received all of the prescribed number of microbeams on the targeted tumors. The other two mice received one out of the three planned microbeams at the primary tumour site while the other 2 microbeams were delivered outside the targeted tumour location. One of these two mice with misplaced microbeams had a relatively small tumour size (<1.4 mm) along the beam array direction, considering the center-to-center spacing used in this study was $900\ \mu\text{m}$. It is noticed that one of the two mice (Animal ID 1086), which was irradiated with a single high dose microbeam, showed a relatively high error (in both error calculation methods) compared to the rest of the mice. The respiratory pattern recorded by the *Biovet* monitoring program indicated that this animal experienced multiple substantial gasps during the irradiation. This could have caused body movement or loosening of the ear bars, leading to the reduced targeting accuracy for this specific animal. Regardless, the results for these two mice were included in the estimation of the targeting error.

There are several potential sources of error in the present procedure including uncertainties in the registration of MR and X-ray images, and consistency in positioning the mouse. First of all, since MR and X-ray images were taken at different facilities, there were transportation and re-positioning of animal from one facility to another. Even though immobilized using the same type of mouse holders and imaged from the same direction, the animals were not positioned exactly the same for MR and X-ray imaging. The variations in orientation of the mouse eventually led to variations in the images. Secondly, the features used for image matching were not perfectly sharp and the images were collected at a finite resolution, both of which contributed to the targeting error observed in this study. Besides, the large tissue shrinkage and deformation not only made it hard to align the stained tissue section manually to the MR image, but it also degraded the accuracy of any measurement on the stained slice.

Another source of uncertainty comes from the mouse head immobilization and anesthesia during irradiation. In our customized mouse holder design, the teeth clamping wire, nose cone, and the ear bars altogether should provide sufficient immobility during irradiation providing that the animals were put under anesthesia. However, if the animal experienced substantial gasping during RT, such as what has happened to mouse ID 1086, drastic body motion or even loosening of the ear bars and teeth clamp could lead to animal dislocation, and hence, the microbeam being off-target.

The microbeam delivery accuracy obtained in the present study is comparable with the targeting accuracy reported in the literature for image-guided small animal irradiators [5]. Matinfar *et al.* showed an error of 0.2 mm in beam alignment when irradiating a radio-opaque marker in a rigid phantom using an in-house small animal radiation research platform (SARRP) [6], and an average displacement in mouse repositioning of 0.8 ± 0.49 mm with this system was reported in a separate study [7]. Another commercially available small animal irradiation device, X-Rad 225Cx (PXI, North Branford, CT) claimed an image-guidance accuracy of no larger than 0.5 mm, and the study on this device by Clarkson *et al.* concluded a consistent accuracy on the order of 0.2 mm in targeting the center of a metal BB fixed to radiochromic film [8]. The small animal research system adapted from a micro-CT at Stanford University achieved 0.1 mm accuracy in each direction using a solid water phantom containing a metal sphere [9]. A distinction must be made when comparing the image-guidance performance of our system to other small animal IGRT systems is the target objects used in the evaluation. In this study, the accuracy level was quantified *in vivo* – targeting the mouse brain tumour, which usually has no well-defined structure and no sharp, clear edges, whereas in other systems it was evaluated with rigid phantoms with unambiguous margins. In addition to the higher requirement in image

quality for brain tumour visualization, the respiration-induced brain motion in the animal during imaging and irradiation posed more challenges for our evaluations compared to rigid phantom studies. On the other hand, all other preclinical IGRT systems generally operate at too large of a field size with large beam penumbras, making them not suitable for MRT. For example, the smallest field size that the SARRP can produce is 500 μm , at which the system can only provide a dose rate of up to 22 cGy/min at 1 cm depth in water [10]. And even then, the 20-80% penumbra is almost 0.2 mm on each side [10]. So far, the system presented in this study is the only one capable of generating microbeams of relevantly high dose rate for small animal studies [5], with a PVDR well within the range of Synchrotron MRT [11].

The results reported here demonstrate that targeted delivery of microbeam radiation in mouse brain tumors is feasible with a MRI/X-ray combined image guidance procedure. The 2D image guidance protocol described in the previous section provides a feasible and efficient way to deliver a single exposure of microbeam array to two mice simultaneously. Nevertheless, there remains much room for improvement in this protocol, i.e. the microbeam alignment, animal fixation, image registration and staining procedures, which would all contribute to a better targeting accuracy. An affine registration algorithm for the brain histology section and MR image alignment can potentially be implemented to provide more accurate evaluation of the targeting errors. Besides, if one mouse is irradiated at a time instead of two, CT images of the mouse can be collected with the on-board micro-CT scanner for 3D registration with the MRI to improve the registration accuracy, which will be introduced in the following section.

5.3 Multi-array Microbeam Irradiation in Brain Tumor Bearing Mice

Multi-directional delivery of microbeams could alleviate skin tissue toxicity caused by the high entrance dose in the peak regions, and at the same it could improve tumor volume

coverage and dose conformity. Several studies have demonstrated the favorable effect of multiple arrays with the potential to improve the tumoricidal effect [12-16]. Radiation beam energy and the entrance dose both need to be increased from the currently used values in small animal studies when it comes to treatment in larger animals and in human. Skin tolerance to the orthovoltage radiation becomes the limiting factor, where multi-port treatment may be the ultimate solution in order to deliver the extremely high dose microbeam radiation to deep seated tumor targets. Preliminary results from the ESRF pet trials demonstrated severe normal tissue damage when a high dose microbeam radiation was delivered in a single array (personal communication).

To investigate the feasibility and efficacy of delivering multi-array MRT from various different directions using the compact microbeam irradiator, the exploration started from the simple and most straightforward case where two arrays are delivered at a right angle, i.e. cross-beam configuration as illustrated in Figure 5.11.

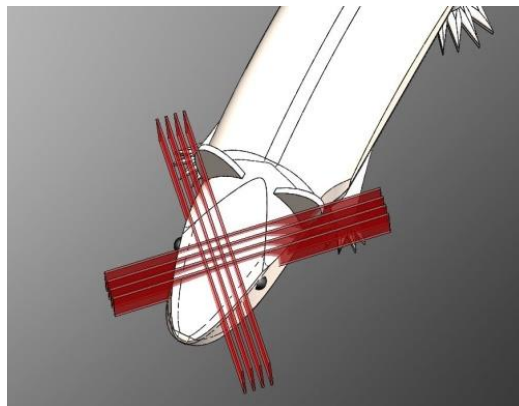


Figure 5.11 Illustration of two orthogonal arrays of microbeams traversing through the mouse brain.

5.3.1 Upgrade in animal positioning device

As the radiation field is fixed in place, the animal positioning setup had to be customized in order to vary the beam entrance location on the mouse head. A new sample stage for the

purpose of cross-beam irradiation has been designed and machined as shown in Figure 5.12. This upgraded device included three mounting plates that are engraved with customized hole patterns to allow for sample positioning at three different angles, i.e. 0° position (L0) which is normal to microbeam entrance line (L), and another two positions at 45° (L1) and -45° (L2) angle relative to L0. Position L0 is for imaging, and is the same as in single array MRT setup. Position L1 and L2 are dedicated for microbeam irradiation with different beam entrance orientations. During the experiment, the animal together with the mouse holder was first mounted on the center plate for imaging at position L0. The two are then removed from the center plate after imaging, and mounted on one of the two side plates for treatment at L1 position. Re-mounting is required for treatment at L2 after the first array is delivered at L1. The design shown in Figure 5.12 employed two side plates with mirrored patterns of mounting holes, and two side blocks for alignment purposes. This design was to accommodate the long mouse stage within the narrow space underneath the microbeam collimator, and also assured that the tumor target fell in the central portion of the radiation field where the flux was the maximum and uniformly distributed. However, a large positioning error was found using this crossbeam stage and the long mouse holder. Modifications were made to both the mouse holder and the sample stage as shown in Figure 5.13. The new mouse bed (base plate) has a reduced length, and also incorporates a close-fit pin hole for extra precision in positioning. Two narrow slots were added on either side as film holders. The new sample stage is a mounting plate with mounting holes for positioning the mouse bed at all three locations (L0, L1 and L2).

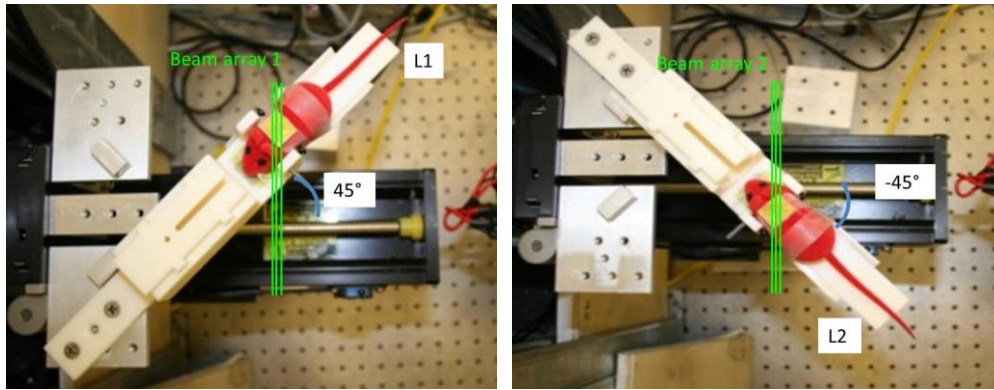


Figure 5.12 Photographs of the setup for delivery two perpendicular arrays of microbeams in the cross-beam configuration. A mouse phantom is placed on the mouse holder, and the green lines demonstrate the microbeam entrance location on the mouse head.

Ideally, switching between mounting positions can be realized by rotation of the mouse holder about a single pin on the sample stage if a wider radiation field in z direction is used. In that case, errors involved in sample repositioning procedures can be largely reduced.

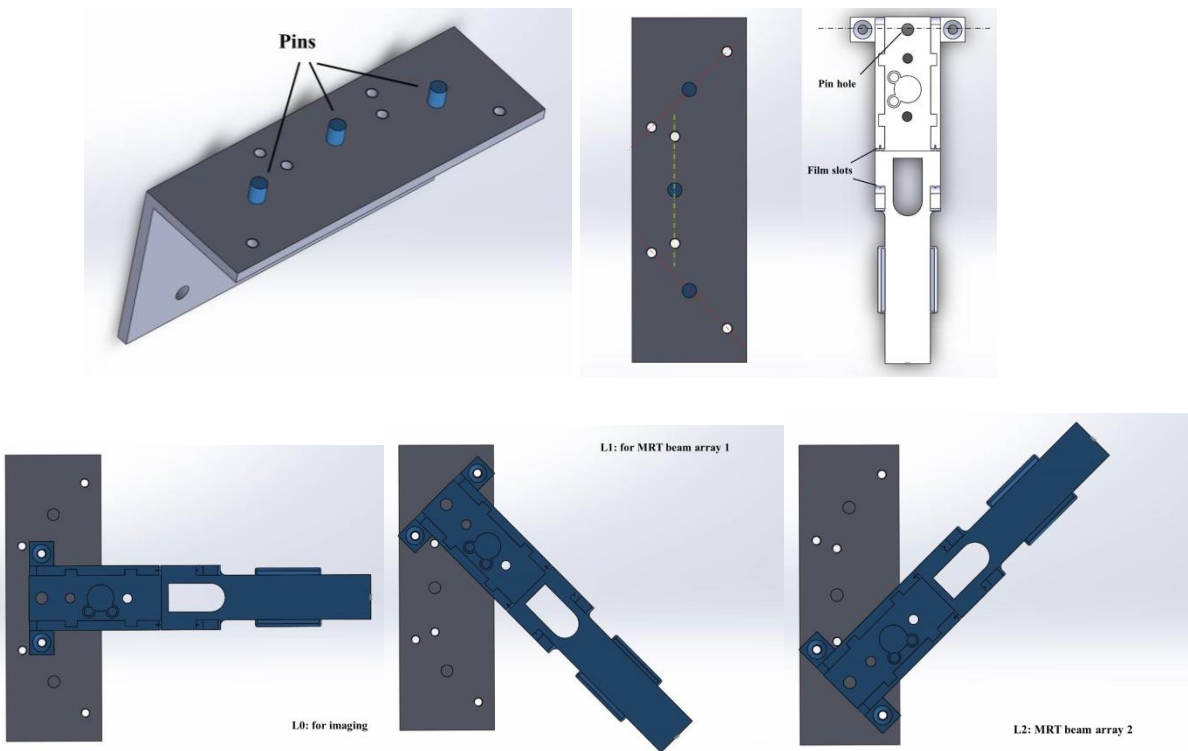


Figure 5.13 SolidWorks drawings of the modified sample stage and mouse holder. The three mounting positions are indicated with dash lines (top right), and illustrated on the bottom row.

5.3.2 Image guidance protocols

In order to deliver multi-directional microbeam arrays to mouse brain tumors, a high accuracy is required in the target identification and beam targeting to avoid false delivery of ‘hot spots’, i.e. regions with augmented doses where the beams overlap, outside the target volume. As opposed to the axially deliver single array MRT where the tumor depth in z direction is not required for beam planning, three-dimensional coordinates of the target need to be fully determined in order to calculate the beam entrance locations for beam arrays from different directions. Therefore image guidance procedures had to be optimized accordingly in order to obtain the stereotactic localization of tumor in the treatment space. The first attempt was made to upgrade the current single planar image guidance method with two-view projections. Afterwards, MRI/CT guidance with 3D registration aided by a clinical treatment planning software was evaluated.

5.3.2.1 Two-view planar image guidance with 2D image registration

This method mostly followed the procedures described in section 1.2 for single array microbeam delivery, except that two projects were collected from coronal view and sagittal view for both MRI and X-ray imaging and that only one animal was imaged and treated at a time. U87MG human glioma bearing nude mouse underwent MRI on Day one for tumor delineation at BRIC small animal imaging facility. The MR imaging protocol used was the same as described earlier in section 1.2.1 with the 9.4 Tesla Bruker BioSpin MR scanner. T2-weighted images were acquired using a Rapid Acquisition with Refocused Echoes (RARE) sequence with an echo spacing-to-recovery time ratio (TE/TR) of 22/3406, 256×256 matrix size, 0.5 mm slice thickness, and 100 micron sagittal and coronal in-plane resolution. Tumor contours were delineated with hyper-intense signal on each slice. Slices with the largest tumor cross-section

(through the center of the tumor volume) in both coronal and sagittal views were used for registration with X-ray projections taken in the corresponding plane. The Animal was then transported to our facility on the next day. Two X-ray projections in coronal view and sagittal view were acquired while the animal was immobilized on the mouse holder under anesthesia (the same protocol as for MR imaging). X-ray projections were taken at 50 kV anode voltage and 0.4 mA anode current with 100 ms pulse width per projection. Afterwards, the MR images and contrast corrected X-ray radiographs were registered in coronal view and sagittal view respectively, as shown in Figure 5.14. Tumor location with respect to the ear bar center (the landmark) in the treatment coordinate system (along x, y and z axis) was determined from the registered images. Since microbeam location with respect to the ear bar center was recorded beforehand, the relative distance between the microbeam entrance and the center of the tumor target can be thus calculated. Instead of direct translation as in unidirectional MRT, rotation of the sample stage was involved after imaging and in between subsequent radiation deliveries. Therefore angular offset as well as the 8° beam tilt needed to be included in the beam targeting calculation for the arrays at both L1 and L2 position as illustrated in Figure 5.12.

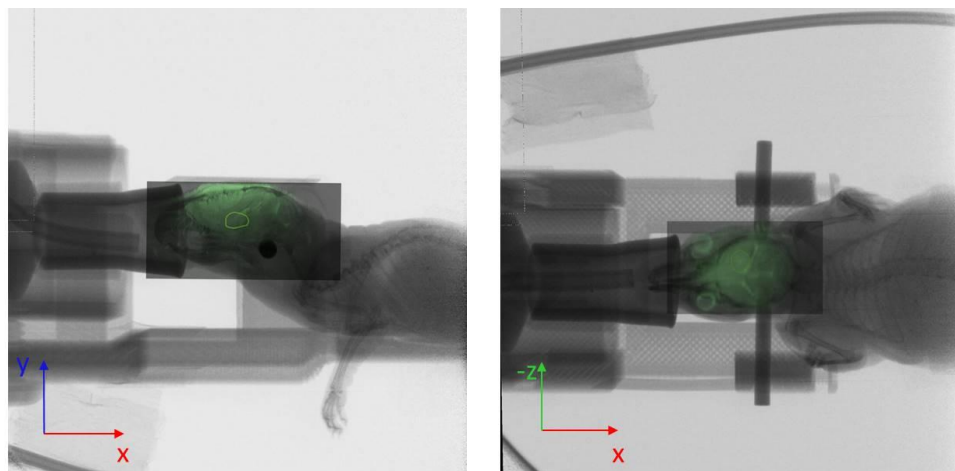


Figure 5.14 Registered MR/X-ray projections in sagittal view (left) and coronal view (right) for the same animal. The tumor target was circled out in green line. The tumor measured $1.5 \times 2 \text{ mm}^2$ in the sagittal plane, and $2 \times 2 \text{ mm}^2$ in the coronal plane.

Two arrays of microbeams were delivered in two fractions to tumor target at position L1 and L2. Within each array four microbeams were delivered in the step-and-shoot manner at 900 μm beam separation (center-to-center distance), with the center of each beam array targeting at the center of the tumor volume. For beam targeting verification purpose, only five minutes short exposure was delivered per microbeam. Animal with the mouse holder was repositioned for the second fraction immediately after the irradiation for the first array was completed. Gafchromic EBT3 films were used for dose verification at the beam entrance, exit locations as well as on the side walls of the mouse holder, as shown in Figure 5.15 on left. The animal was afterwards transferred back to the animal facility and euthanized 4 hours after the radiation as completed. Brain tissue was collected and fixed in formalin. A number of 5 μm thick tissue slices were collected in the coronal plane across the tumor location as determined from the MRI. Tissue slices were sent for $\gamma\text{-H2AX}$ staining at the UNC Translational Pathology Laboratories using the same protocol as described in section 1.2.1.

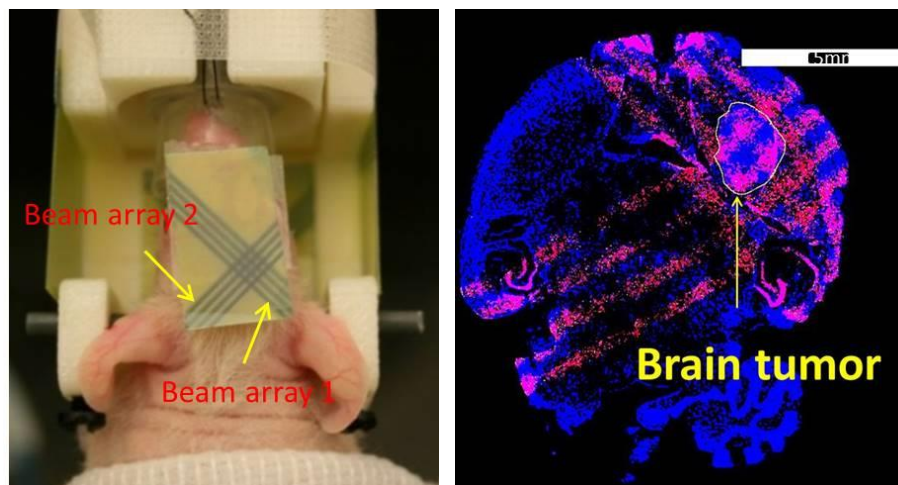


Figure 5.15 Left: A photograph of the U87MG human glioma bearing mouse after treatment of two orthogonal arrays of microbeams. As shown in the Gafchromic EBT3 films, each array consisted four 300 μm wide microbeams at equal spacing (900 μm c-t-c distance). Right: an image of $\gamma\text{-H2AX}$ stained mouse brain tissue (sliced in coronal plane) from the same animal, capturing the microbeam patterns (pink lines) and the covered tumor target (~ 2 mm in diameter). Animal euthanization was performed 4 hours after radiation was completed for tissue collection and fixation.

A fluorescence image from the tissue slide at the tumor center is shown in Figure 5.15 on right. The histology image is presented with the tissue slice positioned in correspondence to the brain position shown on left. The strong γ -H2AX positive signals, shown as pink strips, indicated the DNA double strand breaks caused by microbeam irradiation. The tumor target, shown as a hyper contrast region compared to surrounding normal tissue, is outlined in yellow line. As can be visualized directly from the histology, beam array 2 was delivered precisely on target as originally planned (center of the array aligned with the center of the tumor region), whereas beam array 1 was delivered slightly off-center by 900 μm . The main sources of error probably were the sample stage repositioning, small motion of the mouse head, as well as from the 2D image registration that's subject to the operator's judgment. Besides, the hardware has intrinsic tolerance which could also contribute to the systematic uncertainties in the beam targeting.

5.3.2.2 MRI/CT guidance with 3D image registration

Eventually, the feasibility 3D image-guided microbeam delivery with 3D MRI/CT registration was evaluated through the in-house radiation treatment planning software *PLUNC* (or *PLanUNC*) developed at UNC Department of Radiation Oncology. 3D reconstructed images from CT scan provides better in-plane resolution compared to the 2D projection images due to the removal of overlapping tissue/bone structures. Besides, accurate scale calibration is challenging in planar X-ray images due to the difference in source-to-object distances and viewing angles of different features overlapped in the projection, which results in errors in image registration to MR slice. Such errors can be therefore eliminated with CT images instead.

PLUNC is an adaptable and extensible software system for external beam radiation treatment planning (photon and electron) [17]. It incorporates various features including graphical tools for contouring anatomical structures, virtual simulation, dose calculation and

analysis, and IMRT planning etc. It also allows for manual rigid-body based registration of two sets of 3D images from the same or different imaging modalities. Given the main purpose of the study and operating platform, a special edition of PLUNC was prepared with the aid of the PLUNC developing team and installed on the imaging control desktop computer in our lab.

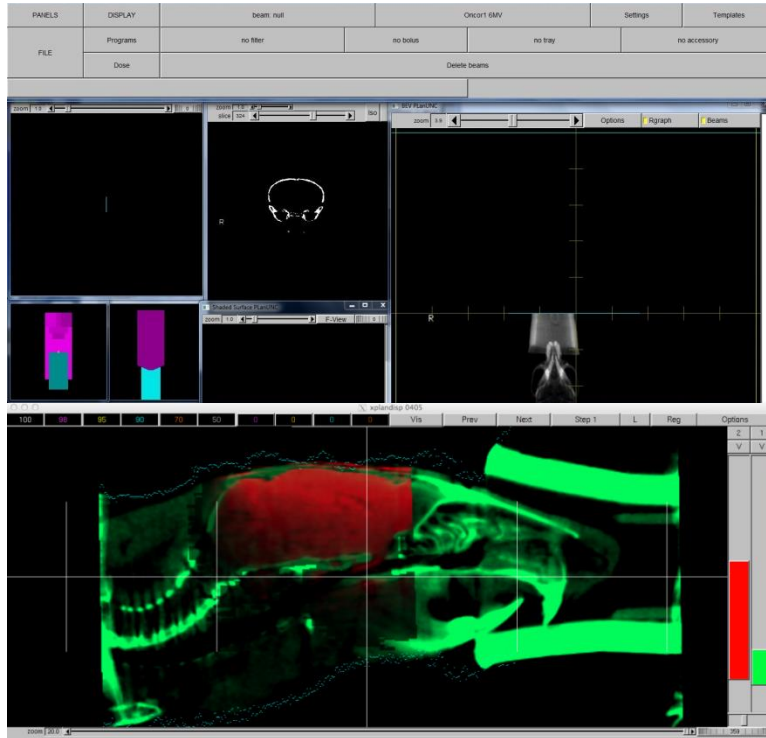


Figure 5.16 Top: screenshot of the user interface of *PLUNC*, clinical treatment planning software developed at UNC Department of Radiation Oncology. A special edition was installed on the desktop computer for micro-CT operation. Bottom: a screenshot showing 3D registration (sagittal view) of a MR scan and CT scan of a mouse in *PLUNC*. Soft tissue contrast in MR image (shown in red) and the contrast in bony structures presented in CT (shown in green) can be adjusted individually. Translation and rotation are performed in three anatomical planes (coronal, sagittal, and axial).

MR imaging protocol remains the same as previous studies. However, instead of selecting a certain image slice, the full stack of DICOM images from the MR scan (2D coronal acquisition), which contained the 3D information of the entire mouse brain, was used for registration afterwards. A small metal ball bearing (made of aluminum, 0.79 mm in diameter) was glued on top of one ear bar pillar as the landmark for image registration as well as for

treatment beam location calibration. CT imaging was performed using the micro-CT scanner at 50 kVp with 1.2 mA anode current. A total of 400 projections were collected at 0.5° angular step. Exposure time was 40 ms for each projection. After corrections with blank and dark images, the projection images were reconstructed at 76 μm isotropic voxel size with COBRA.

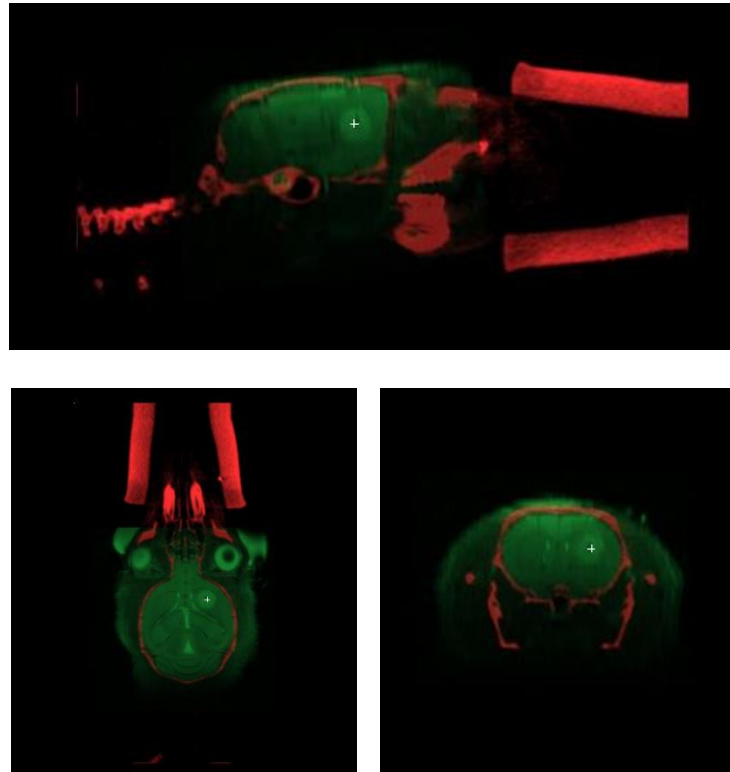


Figure 5.17 Image registration in three anatomical planes using PLUNC. Tumor target is shown with hyper-intense signal from MR images (in green) with the center of volume indicated with a cross mark.

During image registration, the DICOM images from both MRI and CT were first converted to the designated format with Command Prompt before launching PLUNC. The graphical user interface of PLUNC is illustrated in Figure 5.16. Image registration was performed manually in the Dose window. CT and MR images were assigned with different colors. The contrast and intensity window were adjusted respectively for each image set. In

‘Register Images’ mode, the relative location of the CT and MR images were adjusted with one image fixed while the other was translated and rotated into alignment. Adjustment was incremental, and usually started in one of the three anatomical planes and was repeated in the other two orientations to minimize the matching errors. The alignment of the two images was verified in all slices from each orientation. Once the alignment was accomplished in all three orientations, the relative location of the two image sets was fixed, and the 3D coordinates of any feature in the registered image space could be calculated for any point of interest.

Figure 5.17 shows the registered MR and CT of a brain tumor bearing mouse from sagittal (top), coronal (bottom left) and axial (bottom right) view in PLUNC. The tumor volume can be clearly delineated. A cross mark (p1) was placed at the center of the tumor volume (confirmed in three orientations). The metal BB (landmark) on the mouse holder was also identified in the registered images (not shown here) and its center was marked with p2. The aligned images were saved, and the 3D coordinates of p1 and p2 were calculated and recorded. Translation required for beam arrays were calculated based on the calibration of the microbeam entrance location to the center of the landmark (p2).

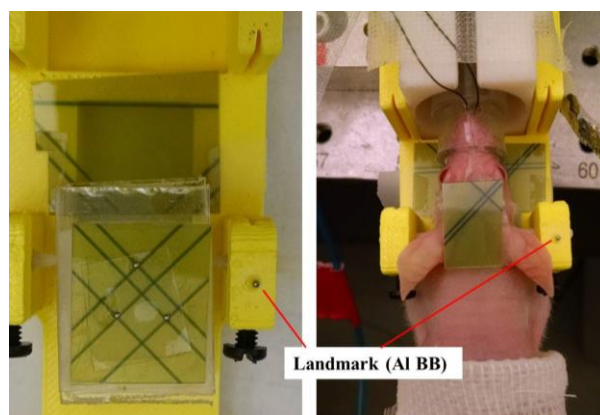


Figure 5.18 Photographs of the new mouse holder designed for crossbeam MRT. A metal bb (Aluminum, 0.79 mm in diameter) is embedded on the ear bar pillar as indicated. The picture on left is from a phantom study to test the reposition consistency of the sample stage, and the picture on right is from U87 bearing mouse irradiated with crossbeam MRT.

The feasibility of this method to guide the delivery of cross-beam MRT was evaluated in five U87MG human glioma bearing mice (average tumor size 1~ 1.5 mm in diameter). Each array contained one to three microbeams depending on the shape and volume of the tumor target. Seven minute exposure was delivered per beam with the microbeam irradiator operating at full power. Animals were sacrificed 4 hours after radiation treatment, and the brains were collected and fixed in formalin for 48 hours. Twelve or fifteen slices of brain tissue were collected around the tumor target at different locations/depths based on the MR images. Each slice is 5 μm thick. The tissue slices were stained with $\gamma\text{-H2AX}$ following the same protocol as in the previous studies. Figure 5.18 on right shows a photo of the animal after crossbeam irradiation. The results from the histological staining are summarized in Table 5.3.

Table 5.3 Summary of the results from the MRI/CT image guided MRT delivered in orthogonal arrays.

Date	Animal ID	Tumor size (mm ²)	MRT protocol	Histology (r-H2AX)
6/30/2015	1294	1.3 x 1.1	10 Gy/beam, crossbeam, 1 beam/array,	Wrong tissue slicing location*
6/30/2015	1300	1.5 x 1.0	10 Gy/beam, crossbeam, 2 beams/array,	Array one delivered on center; Array two delivered off-center by 900 μm .
7/1/2015	1293	2.2 x 2.0	10 Gy/beam, crossbeam, 2 beams/array,	Array one delivered on center; Array two off-center by 350 μm .
7/2/2015	1295	2.0 x 1.0	10 Gy/beam, crossbeam 1 beam on array 1, 2 beams on array 2.	Wrong tissue slicing location*
7/2/2015	1298	2.4 x 1.7	10 Gy/beam, crossbeam, 2 beams on array 1, 3 beams on array 2.	Wrong tissue slicing location*

*Tissue slices were collected at the incorrect depth, possibly due to tissue shrinkage and/or deformation

Figure 5.19 shows the MR image and the stained tissue slices for two mice (ID 1293 and ID 1300) treated with 2×2 (two arrays, two microbeams/array) crossbeam MRT. For both animals, one out of the two arrays (array 1) was delivered accurately on tumor target while the other array (array 2) was delivered off target. The targeting errors in array 2 for these two

animals were about 350 μm and 900 μm , respectively. A systematic error was suspected to be involved in the dose delivery since targeting errors were identified consistently in array 2. In the other three animals, the planned microbeam patterns were shown clearly in the stained tissue slices as shown in Figure 5.20. However, the tumor targets were not present in these stained tissue slices. As mentioned earlier, shrinkage and distortion could be up to 20% during the tissue processing, making it challenging to determine the true target location for tissue collection. Besides, the average tumor size at the time of treatment was merely about 1.5 mm in diameter. Therefore, false slicing depths and insufficient tissue collection resulted in the issues shown in Figure 5.20.

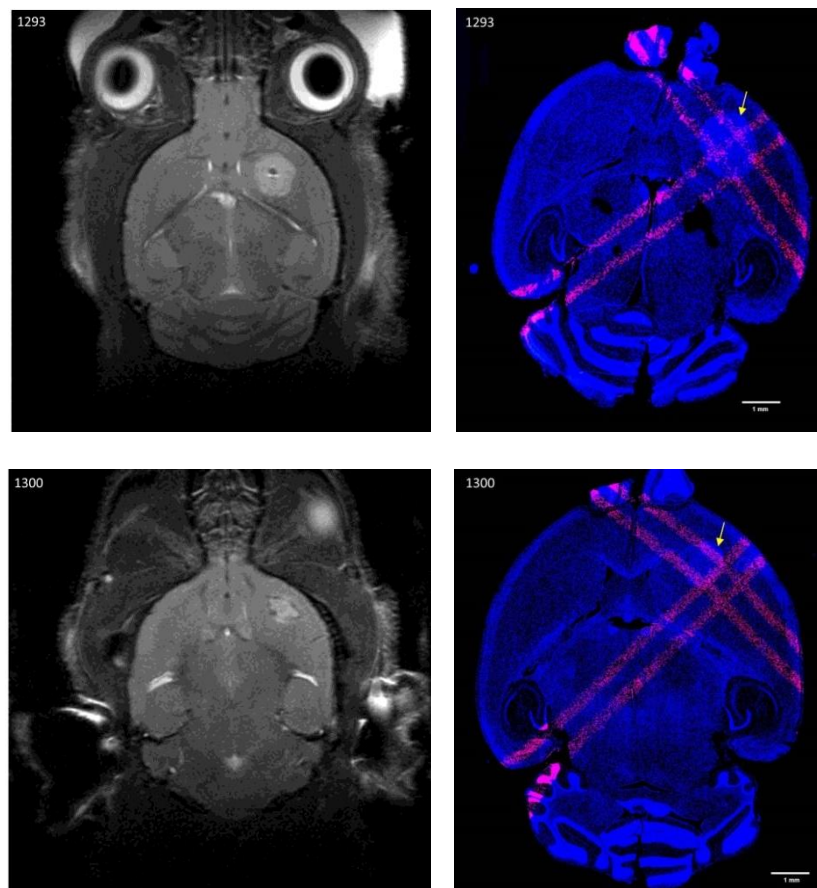


Figure 5.19 γ -H2AX stained tissue slices and the corresponding MR slices from animal ID 1293 (top row) and 1300 (bottom row). Tumor targets are indicated with yellow arrows in the histology slices. For both animals, one out of the two microbeam arrays was delivered accurately on tumor target. Beam array 2 was delivered off-center by about 350 μm for animal ID 1293, and 900 μm for animal ID 1300.

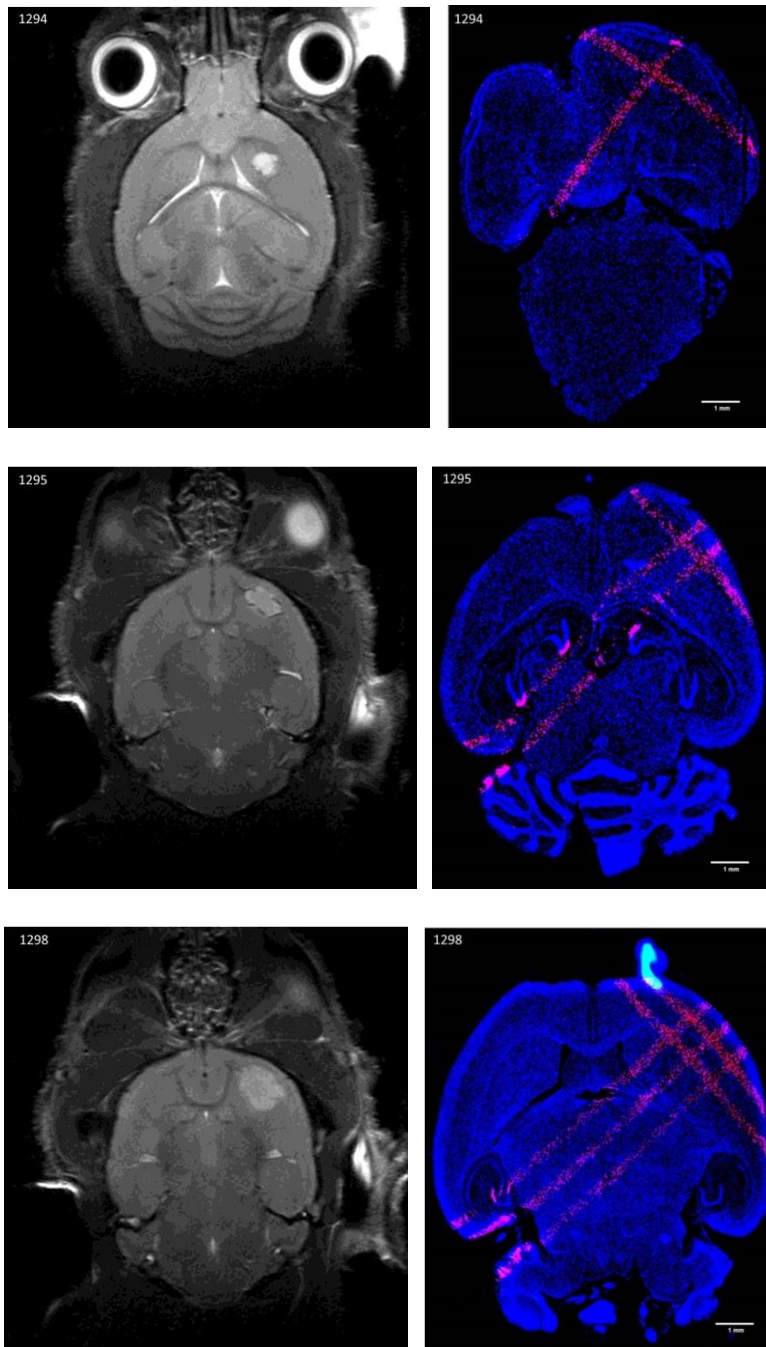


Figure 5.20 γ -H2AX stained tissue slices and the corresponding MR images for the other three animals with ID 1294, 1295 and 1298.

Rigid-body based registration relies largely on animal positioning in both imaging modalities. Since the registration is based on the skull structures where the brain tumor is secured inside, the variation in positioning is expected to have relatively little effect on the alignment. Two main limiting factors of the targeting accuracy in the current method are MR image resolution and the size of the labeling cross mark in PLUNC. In the above feasibility studies, MR images were acquired using a rapid acquisition protocol with 100 μm in-plane resolution and 500 μm slice thickness. The relatively large voxel size in MR dicom would degrade the capability to resolve fine structures for registration, especially in the direction perpendicular to the image plane. A full 3D MR scan of the mouse brain would be desired for an improved image resolution, although the procedure would be rather time consuming. On the other hand, the smallest cross mark available in PLUNC is 0.2 mm in diameter which would be more than enough for clinical applications. However, considering the fine anatomical features and the extremely narrow beam sizes ($\sim 280 - 300 \mu\text{m}$), such large reference points would not provide sufficient precision for determining the exact location of the target with respect to the treatment landmark. Optimization in the PLUNC program would be desired to allow for ultra-fine reference points placement in future experiments.

Although the beam targeting accuracy and consistency remains to be evaluated with further experiments and considerable statistics, the 3D image-guidance offers the potential with enhanced dose delivery accuracy.

REFERENCES

1. Zhang, L., et al., *Image-guided microbeam irradiation to brain tumour bearing mice using a carbon nanotube x-ray source array*. *Physics in Medicine and Biology*, 2014. **59**(5): p. 1283.
2. Paxinos, G. and K.B. Franklin, *The mouse brain in stereotaxic coordinates*. 2004: Gulf Professional Publishing.
3. Winsor, L., *Tissue processing*, in *Laboratory Histopathology*, A.E. Woods and R.C. Ellis, Editors. 1994, Churchill Livingstone: New York p. 4.2-1-4.2-39.
4. Crosbie, J.C., et al., *Tumor cell response to synchrotron microbeam radiation therapy differs markedly from cells in normal tissues*. *Int. J. Radiat. Oncol. Biol. Phys.*, 2010. **77**(3): p. 886-94.
5. Verhaegen, F., P. Granton, and E. Tryggestad, *Small animal radiotherapy research platforms*. *Phys. Med. Biol.*, 2011. **56**(12): p. R55-83.
6. Matinfar, M., et al., *Image-guided small animal radiation research platform: calibration of treatment beam alignment*. *Phys. Med. Biol.*, 2009. **54**(4): p. 891-905.
7. Armour, M., et al., *CT guidance is needed to achieve reproducible positioning of the mouse head for repeat precision cranial irradiation*. *Radiat. Res.*, 2010. **173**(1): p. 119-23.
8. Clarkson, R., et al., *Characterization of image quality and image-guidance performance of a preclinical microirradiator*. *Med. Phys.*, 2011. **38**(2): p. 845-56.
9. Zhou, H., et al., *Development of a micro-computed tomography-based image-guided conformal radiotherapy system for small animals*. *Int J Radiat Oncol Biol Phys*, 2010. **78**(1): p. 297-305.
10. Wong, J., et al., *High-resolution, small animal radiation research platform with x-ray tomographic guidance capabilities*. *Int J Radiat Oncol Biol Phys*, 2008. **71**(5): p. 1591-9.
11. Ansel, D.J., A. Bravin, and P. Romanelli, *Microbeam radiosurgery using synchrotron-generated submillimetric beams: a new tool for the treatment of brain disorders*. *Neurosurg. Rev.*, 2010. **34**(2): p. 133-42.
12. Bräuer-Krisch, E., et al., *New irradiation geometry for microbeam radiation therapy*. *Phys. Med. Biol.*, 2005. **50**(13): p. 3103-11.
13. Dilmanian, F.A., et al., *Interlaced x-ray microplanar beams: a radiosurgery approach with clinical potential*. *Proc. Natl. Acad. Sci. USA*, 2006. **103**(25): p. 9709-14.
14. Dilmanian, F.A., et al., *Murine EMT-6 carcinoma: high therapeutic efficacy of microbeam radiation therapy*. *Radiat. Res.*, 2003. **159**(5): p. 632-41.

15. Serduc, R., et al., *First trial of spatial and temporal fractionations of the delivered dose using synchrotron microbeam radiation therapy*. J. Synchrotron Radiat., 2009. **16**(Pt 4): p. 587-90.
16. Bouchet, A., et al., *Preferential effect of synchrotron microbeam radiation therapy on intracerebral 9L gliosarcoma vascular networks*. Int. J. Radiat. Oncol. Biol. Phys., 2010. **78**(5): p. 1503-12.
17. <http://planunc.radonc.unc.edu/>.

CHAPTER 6: PRECLINICAL EVALUATION OF MRT THERAPEUTIC EFFICACY USING THE COMPACT IRRADIATOR

6.1 Introduction

The development of the compact microbeam radiation therapy system is a long-term continuing effort with iterative system optimization, which requires comprehensive characterization in source and radiation beam quality, dosimetric parameters, as well as extensive preclinical and clinical validation. Preclinical study on small animal models not only stands as a critical step in the therapeutic efficacy evaluation of a new RT modality, but also provides valuable feedback of the system performance. It was finally made possible after the development of physical components and methodologies was achieved as described in previous chapters in this thesis and those completed previously [1]. This chapter presents the initial effort of biological assessment carried out using the prototype image-guided MRT system over the course of three years. These preliminary results from animal studies not only validated the treatment efficacy of the unique dosimetric characteristics generated by the prototype microbeam irradiator, but also demonstrated the potential of the compact system as an efficient and effective tool for MRT radiobiological studies both preclinically and clinically.

The majority of this work was conducted as an effort of collaboration with Dr. Hong Yuan at UNC Biomedical Research Imaging Center. The method of image-guided delivery of single array microbeams was introduced in Chapter 5, and the detailed procedures were published in Zhang *et al.* in *Physics in Medicine and Biology* [2]. The main biological results from the single array MRT experiments were published in “Treating brain tumor with

microbeam radiation generated by a compact carbon-nanotube-based irradiator: initial radiation efficacy study” by Yuan *et al.* in *Radiation Research* 184, 322 – 333 (2015) [3]. Part of the preliminary results from the crossbeam microbeam irradiation was published in “Nanotube x-ray for cancer therapy: a compact microbeam radiation therapy system for brain tumor treatment” by Zhang *et al.* in *Expert Review of Anticancer Therapy* 14 (12), 1411 – 1418 (2014) [4].

6.2 Methods and Materials

Biological effects of microbeam radiation therapy were evaluated in terms of tumor local control, and cellular responses in both tumor and normal tissues. A total number of 76 human brain tumor bearing mice and six normal mice were included in the investigation. Animals were grouped for different treatments as summarized in Table 6.1.

Table 6.1 Summary of the biological studies carried out with the CNT-MRT system

Group	Type of animals	Number of animals	Treatment	Prescribed dose	Follow-up
1	U87 mice	19	Sham (Isoflurane only)	None	
2	U87 mice	19	Low-dose MRT	48Gy/beam, 3 beams	
3	U87 mice	4	High-dose MRT	72Gy/beam, 2 beams	Survival & Tumor progression analysis
4	U87 mice	9	BRT	10 Gy	
5	U87 mice	2	Crossbeam MRT	50 Gy/beam, 4 beams/array, 2 arrays	
6	U87 mice	15	low-dose MRT	48Gy/beam, 3 beams	
7	U87 mice	8	BRT	10 Gy	Histological examination (γ -H2AX, cleaved caspase-3, Ki-67, F4/80)
8	Normal mice	6	Low-dose MRT	48Gy/beam, 3 beams	

6.2.1 Brain tumor bearing mouse model

All animal handling and experimental procedures in the study were approved by the Institutional Animal Care and Use Committee at University of North Carolina. Male athymic nude mice (4 – 6 weeks old) were used for brain tumor inoculation. U87MG human glioblastoma tumor cells were obtained from Dr. Ryan Miller’s lab at UNC Department of Pathology and

maintained in the laboratory at BRIC. About 23,105 cells in 5 μ l culture media mixed with 5% methylcellulose were injected into the forebrain of mice using the stereotaxic technique at 1 mm anterior, 2 mm lateral to the bregma and 4 mm deep from the surface to form the orthotopic xenograft glioblastoma mouse model. Three weeks after tumor cell injection, the mice were brought to the Imaging Core Facility for MRI and subsequent radiation treatment.

6.2.2 Image guidance

6.2.2.1 Unidirectional microbeam array

Single view X-ray/MR image guidance, described in Chapter 5.1.2 was employed for delivering a single array microbeams in the survival and immunohistological studies [2]. Briefly, mice were first imaged at BRIC small animal imaging core facility for tumor delineation, and then transported to our lab at the Department of Physics and Astronomy the next day for X-ray imaging, beam planning, and MRT. Animals were transferred back to BRIC for euthanization, or housed at UNC Division of Laboratory Animal Medicine for further investigation. During all imaging and radiation procedures, the animals were anesthetized with isoflurane (1.5%) mixed with 100% oxygen. The respiration signals were monitored with a pressure sensor that's placed underneath the abdomen and presented via Biovet user interface.

Mice were initially imaged at 3 weeks after tumor cell inoculation for tumor localization and volume measurement. MRIs were performed on a small animal 9.4 Tesla MRI system (Bruker Inc., Billerica, MA). T2-weighted images were acquired in rapid acquisition with refocused echoes (RARE) sequence with the following parameters: TE/TR = 22/3,400 ms, 256 \times 256 matrix size, 0.5 mm slice thickness and 100 μ m in-plane resolutions. Tumor volume was measured manually on each MRI slice with ImageJ.

X-ray projections were taken at 50 kV anode voltage and 0.4 mA anode current with 100 ms pulse width. Projection images were then corrected with blank and dark images, and were registered manually to MR images in *photoshop*. Thereby the tumor location (center) with respect to the ear bar center (the landmark) in the treatment coordinate system (along x and y axis) was determined from the registered images. Animals were translated to the microbeam irradiator accordingly and irradiated with a single array of microbeams.

6.2.2.2 Crossbeam MRT

The orthogonal array MRT was delivered following the two-view planar MR/X-ray image guidance protocol with 2D image registration as described in chapter 5 section 1.3.2. The detailed procedure is not repeated here for the purpose of simplicity.

6.2.3 Radiation treatment

6.2.3.1 Microbeam radiation therapy

Fifty-nine tumor-bearing mice and six normal mice were treated with MRT for survival and immunostaining studies. In the survival study, 42 tumor bearing mice were distributed into three groups, and the average tumor size of each group was not statistically different from the other groups before treatment. The three groups included a non-irradiated control group (isoflurane only, no irradiation, n = 19), a low-dose MRT group (48 Gy/microbeam, n = 19) and a high-dose MRT group (72 Gy/microbeam, n = 4). Two U87 bearing mice with relatively large tumor volume received crossbeam MRT (50 Gy/microbeam, 2 arrays) in two days. Another batch of U87 tumor-bearing mice (n = 15) and normal mice (n = 6) were used for immunostaining studies.

The source-to-surface distance (focal line to mouse head) during the microbeam irradiation was kept at ~124 mm. The average dose rate at the entrance plane was measured to be

1.2 Gy/min. Peak dose of 48 or 72 Gy was used for the low- or high-dose MRT group, respectively. Each microbeam was 280 μm wide and 160 mm long, spaced at 900 μm center-to-center distance. Three microbeams of radiation were delivered unidirectionally across the mouse brain in the low-dose MRT group, while two microbeams were delivered in the high-dose MRT group, so that the total integrated doses remained the same in the two MRT groups.

For the crossbeam MRT group, two arrays of microbeams were delivered successively in two days with the crossing regions targeted to the tumor volume. Each array has four microbeams with 50 Gy/beam peak entrance dose. Beam separation was 900 μm to maintain a valley dose at no more than 3 Gy. Microbeam profiles were verified by Gafchromic films placed at the entrance and exit plane of the mouse head.

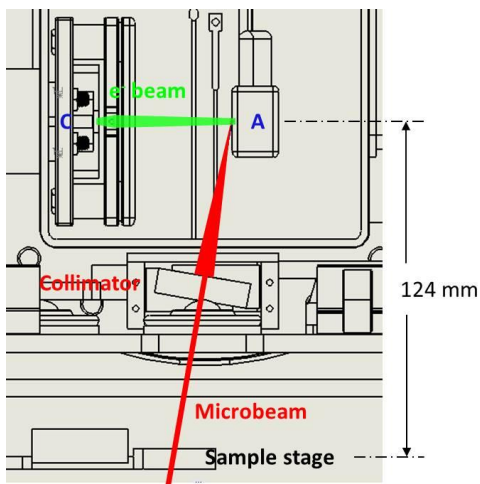


Figure 6.1 Illustration of the configuration of a mouse being irradiated in the head using the microbeam generated by the CNT-based microbeam radiation therapy system. The source-to-surface distance was kept at 124 mm for all treated animals.

6.2.3.2 Broad-beam radiation treatment

A separate group of U87MG tumor-bearing mice ($n = 17$) was treated with conventional broad-beam radiation (BRT) as a comparison group. Mice were anesthetized with isoflurane inhalation method and immobilized with the same mouse holder. Conventional radiation of 10

Gy was delivered to the mouse brain from a clinical linear accelerator (Siemens Primus, 6 MV photon beam). The radiation field is 1 cm × 1 cm centered on the mouse brain covering the tumor target. The treatment dose was computed with in-house clinical treatment planning software PLUNC. After irradiation, one group of mice (n = 9) was used for survival time investigation. The remaining eight animals were used for histological analysis. Brain tissue samples were collected at 24 h (n = 4) and 48 h (n = 4) after irradiation.

6.2.4 Survival & statistical analysis

After irradiation, mice were imaged with MRI (same protocol as for image guidance) weekly for two weeks after MRT to monitor changes in tumor volume. The monitoring period terminated when the last animal was euthanized due to tumor progression. The survival time (in days) individual animal was recorded, and the survival curves for each group were generated using Kaplan-Meier method (GraphPad Prism software; GraphPad Software Inc., LaJolla, CA). The median survival time (MST) and the percentage of extended life span were reported. The extended life span is defined as the ratio of the MST extension of the treated group to the MST of the control group (sham group). Survival curves were compared using the logrank test between each group. Data on expression level of γ -H2AX, caspase-3 and Ki-67 were presented as mean \pm standard error of the mean (SEM). Differences between expression level on tumor and normal tissue at different time points after MRT were compared using t test. $P < 0.05$ was considered statistically significant.

6.2.5 Immunohistological analysis

Tumor-bearing mice were euthanized at 1, 4, 24, 48 h and day 7 after low-dose MRT or at 24 and 48 h after BRT. Brains were collected and fixed in formalin for 48 h. The fixed brains were then dehydrated, embedded in paraffin and cut into 5 μ m brain sections in sagittal plane

perpendicular to the microbeam direction near tumor location. The cutting location was determined from MR images. Three consecutive brain sections were stained with antibodies to phosphorylated histone γ -H2AX (rabbit anti-mouse γ -H2AX antibody; Cell Signaling Technology®, Danvers, MA), cleaved caspase-3 (Biocare Medical Inc., Concord, CA) and Ki-67 protein (BD Pharmingen, San Diego, CA) to assess DNA double strand breaks, apoptosis and cell proliferation, which have been well documented in the literature [5, 6]. All immunostaining procedures were conducted in the Tissue Pathology Core Facility (UNC Lineberger Comprehensive Cancer Center) with standardized staining protocol for all the tissue slides and positive/negative slides. For staining, tissue sections were deparaffinized followed by antigen retrieval with citrate buffer, and incubated with primary antibodies to one of the three proteins following the protocols: γ -H2AX, 1:1,000 dilution, 8 h incubation; cleaved caspase-3, 1:400 dilution, 4 h incubation; and Ki-67, 1:500 dilution, 4 h incubation. The sections were then incubated with an appropriate secondary antibody followed with tyramide Cy5 amplification (PerkinElmert Inc., Boston, MA). To stain nuclei and preserve the fluorescent signals, ProLong® Gold antifade reagent containing 4, 6-diamidino-2-phenylindole (DAPI) was used (Molecular Probes®, Eugene, OR) on stained sections. The section was then scanned in the DAPI and Cy5 channels using a high-resolution (20 × objectives) fluorescence slide scanner system (ScanScope FL scanner, Aperio®, Vista, CA). Immunostaining of γ -H2AX, caspase-3 and F4/80 (microglia and macrophage marker) was conducted on normal mouse brain tissues at 24 h and at day 30 after irradiation to assess both acute and chronic damage on normal tissue from microbeam radiation.

6.2.5.1 Characterize DNA damage with γ -H2AX staining

The γ -H2AX quantification method was based on a previously published study [7] where the positively stained γ -H2AX fluorescence signal in nuclei was confirmed to be correlated with the expressed γ -H2AX protein level measured by Western blot. To quantify the γ -H2AX signal, cell nucleus region was first extracted from the DAPI nuclei counterstaining channel and masked to the γ -H2AX Cy5 fluorescence channel. Since γ -H2AX foci were present solely in cell nuclei, only signals inside the cell nuclei were measured. This method prevented the possibility of bias caused by different cell density in tumor and normal brain tissue. Five regions were defined based on the γ -H2AX staining images: radiation beam passing regions on the tumor tissue (tumor peak region) and on the contralateral normal brain tissue (normal peak region), beam valley regions on the tumor tissue (tumor valley region) and normal brain tissue (normal valley region) and regions away from the MRT field as normal tissue background (normal tissue region). Average fluorescence signal on the masked nuclei area was measured as mean γ -H2AX signal for the five regions.

6.2.5.2 Characterize cell apoptosis using cleaved caspase-3

Apoptosis was detected using cleaved caspase-3 staining. The caspase-3 images were first aligned with the γ -H2AX images from the neighboring section with ImageJ, and the five tissue regions defined in the γ -H2AX images were mapped to the caspase-3 images. Numbers of positively stained cells in peak and valley regions were counted in tumor and normal tissue. The number of positively caspase-3 stained cells per mm^2 was calculated as a quantitative measure of the apoptosis level after irradiation.

6.2.5.3 Characterize cell proliferation using Ki-67 immunofluorescence staining

Cell proliferation in irradiated brain tissue was quantified using Ki-67 immunofluorescence staining. One tumor section from a sham-irradiated mouse was always included as a positive control. Area fraction of positive Ki-67 staining on the nuclei area was measured in the tumor peak and tumor valley regions. The ratio between irradiated tumor tissue and non-irradiated positive control was reported as the proliferation ratio. In the contralateral normal brain tissue, the number of positively stained cells on the irradiated region in the middle of striatum of MRT mice and the same sized region of BRT mice was measured as the parameter to quantify normal tissue proliferation.

6.3 Results

6.3.1 Verification of dose delivery

The radiation delivery was verified using Gafchromic EBT2 films placed at the entrance and exit planes of the mouse head. Films in this study were analyzed with FilmQaPro. The beamwidth (FWHM) was measured to be 280 μm at the entrance plane on the top of the mouse brain and 380 μm at the exit plane at the bottom of the head. The PVDR was 16 at the entrance plane and decreased to 14 at the exit plane as shown in Figure 6.2 top row. The positive expression of $\gamma\text{-H2AX}$, shown as pink strips, correspond to the tracks of microbeam radiation dose deposition which induced DNA double strand breaks in both normal and tumor cells (Figure 6.2 middle and bottom row). The center-to-center distance between two adjacent tracks in the $\gamma\text{-H2AX}$ image was measured to be 782.2 μm on average, close to the prescribed 900 μm beam separation when taking the 20% tissue shrinkage during histology processing into consideration [8]. The FWHM of the beam track was 343.4 μm measured from the $\gamma\text{-H2AX}$ staining images, slightly wider than the radiation beamwidth at the exit plane after taking the

tissue shrinkage into consideration. This was possibly due to the nonlinear response between radiation dose and γ -H2AX expression at doses above 10 Gy [9].

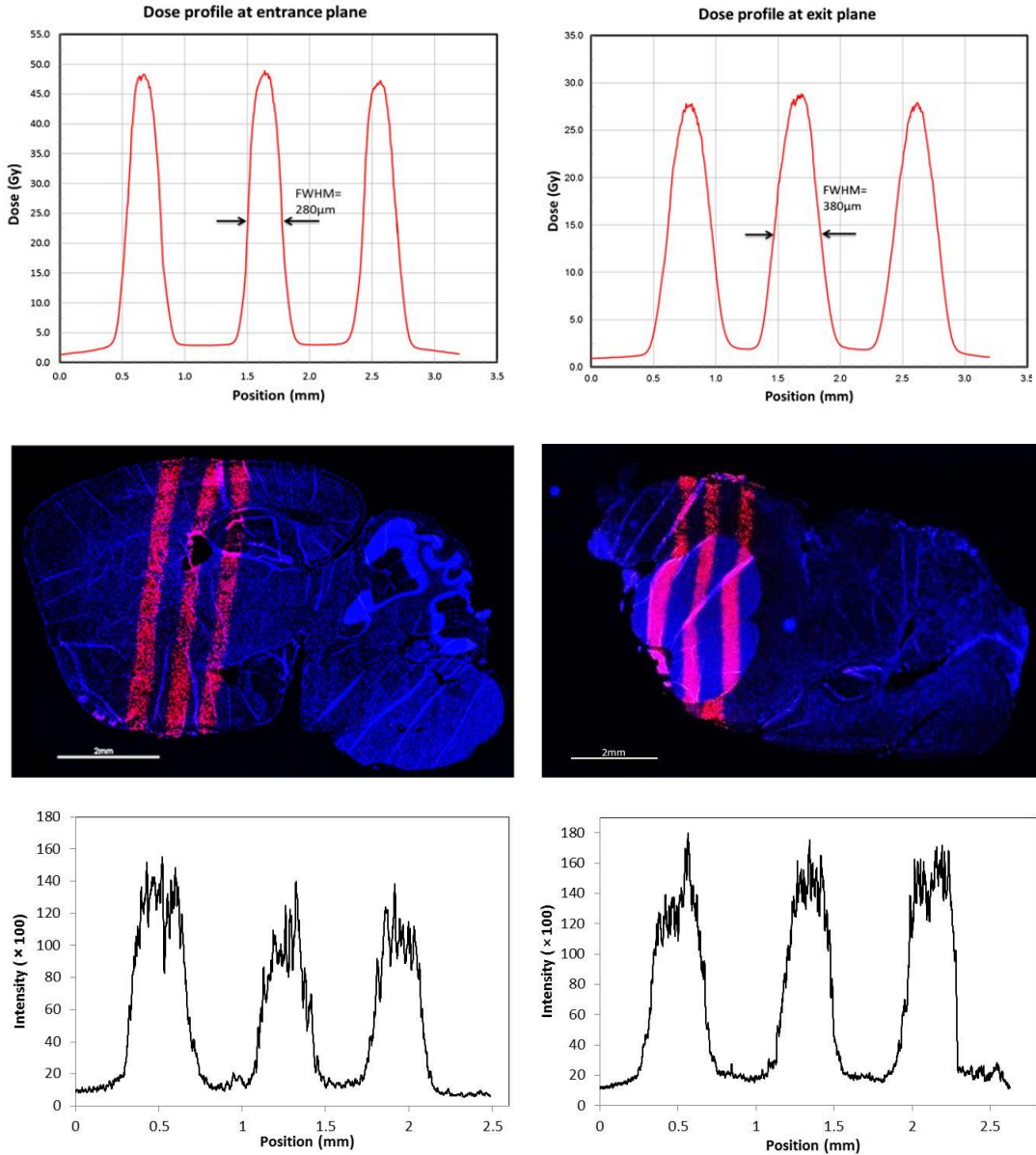


Figure 6.2 Top row: microbeam profiles recorded by Gafchromic EBT2 films placed at the radiation entrance (left) and exit (right) planes on the mouse head. Middle row: images of γ -H2AX stained brain tissue from a normal mouse (left) and a brain tumor bearing mouse (right). The positive expression of γ -H2AX, shown as pink strips, correspond to the tracks of microbeam radiation dose deposition, which induced DNA double strand breaks in both normal and tumor cells. Bottom row: the beam profiles drawn from the histology slices. Reprinted with permission from Yuan *et al. Radiation Research* 184, 322-333 (2015) [3].

6.3.2 Microbeam effects on the mean survival time

The survival curves of four experimental groups are summarized in Figure 6.3. The median survival time for the non-irradiated control group was 35 days after tumor inoculation [95% Confidence Interval = (34.4, 35.6)]. The MST for animals treated with low-dose MRT, high-dose MRT and BRT was 46 (43.2, 48.8) days, 52 (40.8, 63.2) days and 52 (50.9, 53.1) days (values shown in parentheses are 95% confidence interval) respectively. The life spans of animals treated with high- and low-dose MRT were significantly extended by 31.4 and 48.5% ($P < 0.001$,) respectively, compared to the control group. The extended life span for the BRT group was 48.5%. There was no significant difference among the BRT group and the two MRT groups in terms of median survival time ($P > 0.05$,).

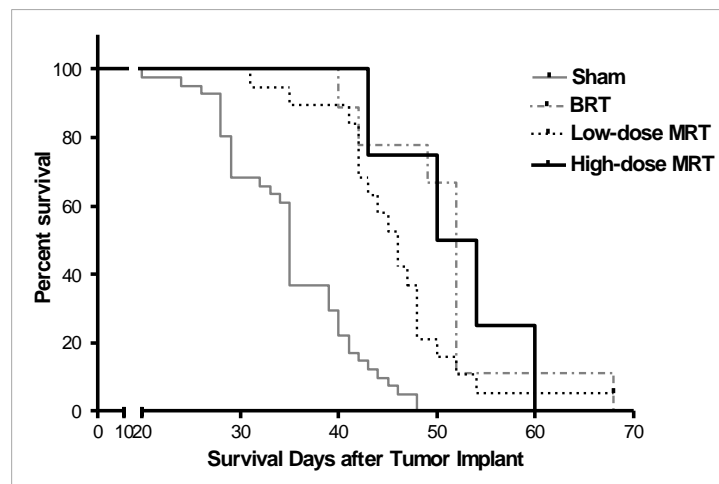


Figure 6.3 Survival curves of U87MG bearing mice with different treatments. Animals in the sham group were anesthetized with isoflurane without any radiation treatment. BRT group was treated with 10 Gy conventional radiation with a 1 cm × 1 cm field size, using a clinical linear accelerator. Radiation doses were 48 Gy/microbeam and 72 Gy/microbeam for low-dose MRT and high-dose MRT groups, respectively. Reprinted with permission from Yuan *et al. Radiation Research* 184, 322-333 (2015) [3].

6.3.3 Microbeam effects on tumor local control

Tumor volumes in all animals were monitored with MRI scans before and after radiation treatment. Figure 6.4A shows typical T2 weighted MR images from each group at different time

points. Absolute tumor volume measurement for each group is shown in Figure 6.4B. The relative volume change is defined in the following equation:

$$\frac{V_t - V_0}{V_0}$$

Where V_t is the volume at time t , and V_0 represents the initial tumor volume at the day before treatment. Such relative tumor volume change was calculated for individual animals and plotted in Figure 6.4C. At one week after MRT, the control group had 10.0 ± 2.1 fold of increase in tumor volume, while the low-dose and high-dose MRT groups had only 4.1 ± 1.1 fold and 1.5 ± 0.8 fold of volume increase, respectively, demonstrating significant inhibition of tumor growth after MRT ($P < 0.01$ for both MRT groups and the control group). At day 14 after MRT, tumor volume was 51.7 ± 16.0 , 37.0 ± 9.4 and 14.3 ± 4.1 fold of increase in the sham-irradiated, low-dose and high-dose MRT groups, respectively. Tumor growth was continuously suppressed (>10 times) by the high-dose MRT at a significant level ($P = 0.04$), while only a trend of inhibition was observed with low-dose MRT ($P = 0.21$).

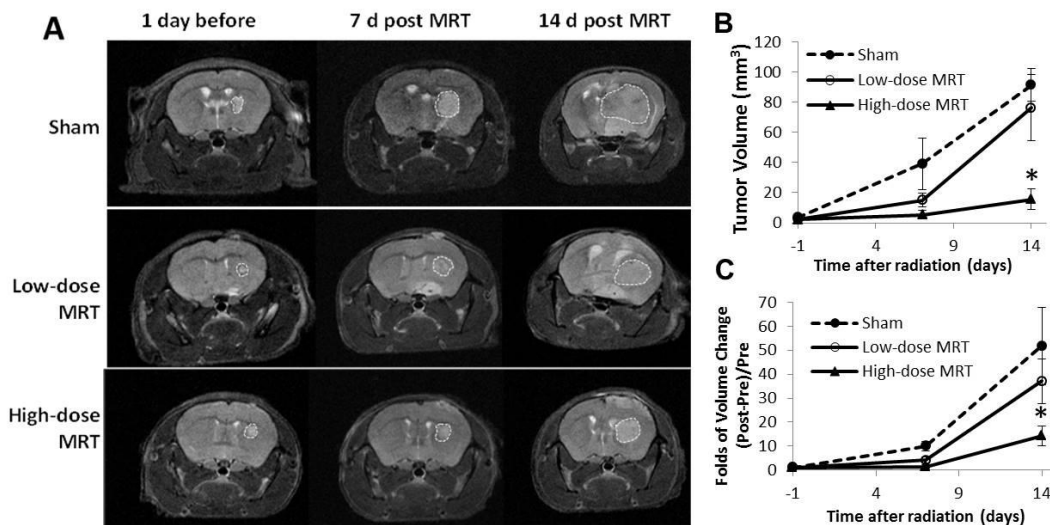


Figure 6.4 A: T2 weighted MR images of the mouse brains before and after different treatment. Tumor targets were contoured with white dash lines. B and C: absolute and relative tumor volumes growth calculated from the MR images. Reprinted with permission from Yuan *et al. Radiation Research* 184, 322-333 (2015) [3].

6.3.4 Microbeam radiation induced DNA damage and its dynamics

Expression of γ -H2AX was measured at 1, 4, 24, 48 h and day 7 after MRT. Figure 6.5 shows γ -H2AX staining on both tumor and normal tissue in the contralateral hemisphere. Strong expression was observed as early as 1 h post-irradiation on both tumor and normal tissue on the radiation beam passing regions, indicating radiation-induced DNA DSBs. The expression reduced over time from 1 h to day 7 after irradiation on both tumor and normal tissue, which suggests ongoing repair process in response to DNA damage. Seven days after irradiation, the γ -H2AX signal in the normal valley region dropped to background level, which was not the case in the tumor tissue. Average γ -H2AX signal in nuclei was quantified in the five regions, as defined in the Materials and Methods section. In the irradiated region, there was a trend of higher γ -H2AX level in tumor (tumor peak) compared to that in the normal brain tissue (normal peak) at all time points, but it was not statistically significant, possibly due to high variation. In the radiation valley region, the γ -H2AX signal was initially similar between the tumor valley and normal valley regions, but showed significantly higher in tumor valley region starting at 24 h post-irradiation. The signal in the tumor valley was 1.38-, 1.61- and 1.92-fold higher than that in the normal valley region at 24 and 48 h and day 7 after irradiation ($P = 0.045$, 0.038 and $P < 0.001$, respectively). More interestingly, the γ -H2AX signal differences between peak and valley regions in tumor reduced dramatically at 48 h and almost diminished (ceased?) at day 7. The signal ratio between peak and valley regions in tumor changed from 5.2 at 1 h after MRT to 2.3 at 48 h and 1.1 at day 7 after MRT. Figure 6.5A shows that the γ -H2AX foci were more dispersed from the beam tracks to the overall tumor region at 48 h and day 7 after irradiation. In contrast, there were still clear separations between peak and valley regions at 48 h and day 7 after MRT in normal tissue, although the signal was quite weak at the 7-day time point. The

spreading of γ -H2AX signal in the tumor might be caused by tumor cell migration and possible bystander effect.

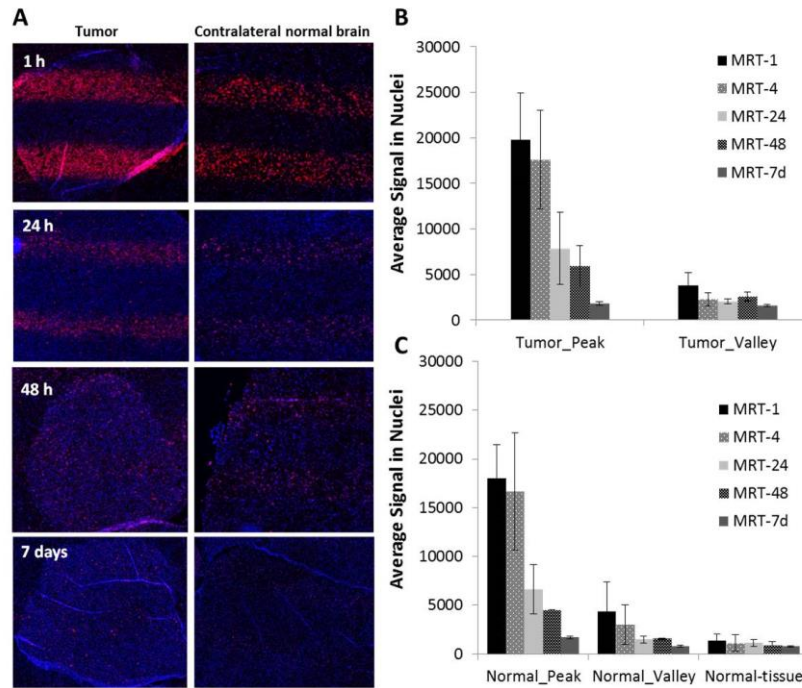


Figure 6.5 γ -H2AX stained normal mouse brain tissue and brain tumor tissue after microbeam treatment. A: changes of γ -H2AX positive signal at different times post-irradiation. Microbeam paths were clearly distinguishable from the background in both tumor region and normal tissue at 1h and 24h post-irradiation. The beam tracks blurred out in tumor at 48h and 7 days after radiation, which was not observed in normal tissue in contrast. B and C: quantification of the γ -H2AX expression. The expression decreased over time after treatment, indicating the cell repair process. Reprinted with permission from Yuan *et al. Radiation Research* 184, 322-333 (2015) [3].

6.3.5 Microbeam effects on apoptosis and cell proliferation

Figure 6.6 shows the results of caspase-3 staining on tumor and normal brain tissue. In the tumor tissue, positive cleaved caspase-3 signal was initially low, but increased over time in both the tumor peak and tumor valley regions Figure 6.6 (A-C). Interestingly, the difference in apoptosis level between the peak and valley regions in the tumor decreased significantly at 48 h and at day 7 after irradiation. The ratio of apoptotic cells in the peak to that in the valley region was 2.3 at 4 h, dropping to 1.1 at day 7 after MRT Figure 6.6C. The number of apoptotic cells

was $(59 \pm 12)/\text{mm}^2$ in the peak region and $(55 \pm 14)/\text{mm}^2$ in the valley region at day 7 in the tumor tissue.

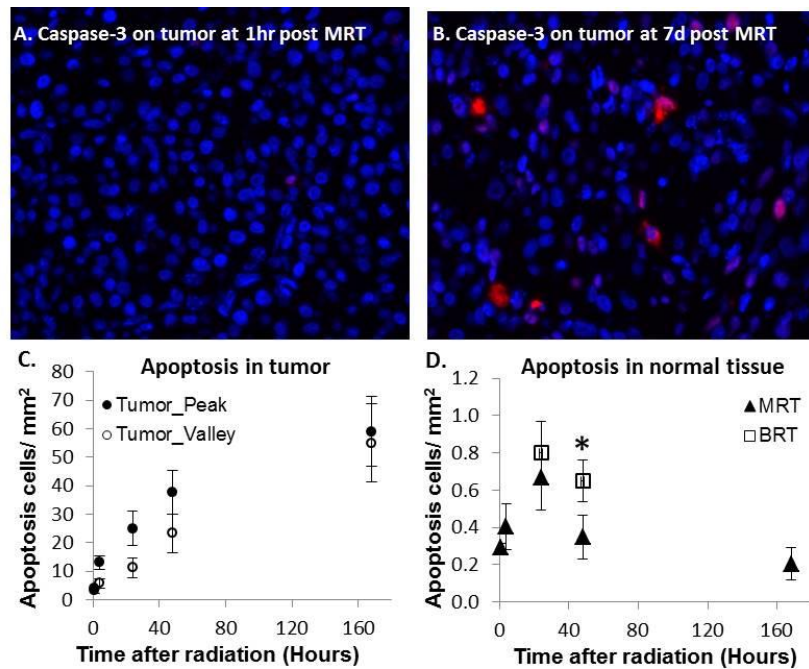


Figure 6.6 Immunofluorescence staining of cleaved caspase-3 as cell apoptosis assay. Cleaved caspase-3 signal is shown in red, while DAPI counterstaining of the nuclei is shown in blue. A and B: Levels of apoptosis in tumor at 1h and 7d after MRT. Reprinted with permission from Yuan *et al. Radiation Research* 184, 322-333 (2015).

The number of apoptotic cells in contralateral normal brain tissue within the microbeam radiation field was quantified after the low-dose MRT (Figure 6.6 D). Compared to the tumor tissue, there was a much lower level of apoptosis in the normal brain tissue after MRT. Apoptotic cells were mainly in the microbeam peak region with little to no apoptotic cells in the valley region, as shown in Figure 6.8. The number of apoptotic cells peaked at 24 h after MRT ($0.66 \pm 0.12/\text{mm}^2$) and reduced thereafter in the normal brain tissue. Apoptosis level was also assessed in normal brain tissue at 24 and 48 h after BRT and was significantly higher ($0.65 \pm 0.11/\text{mm}^2$) compared with that in the MRT group ($0.35 \pm 0.09 /\text{mm}^2$) at 48 h after irradiation.

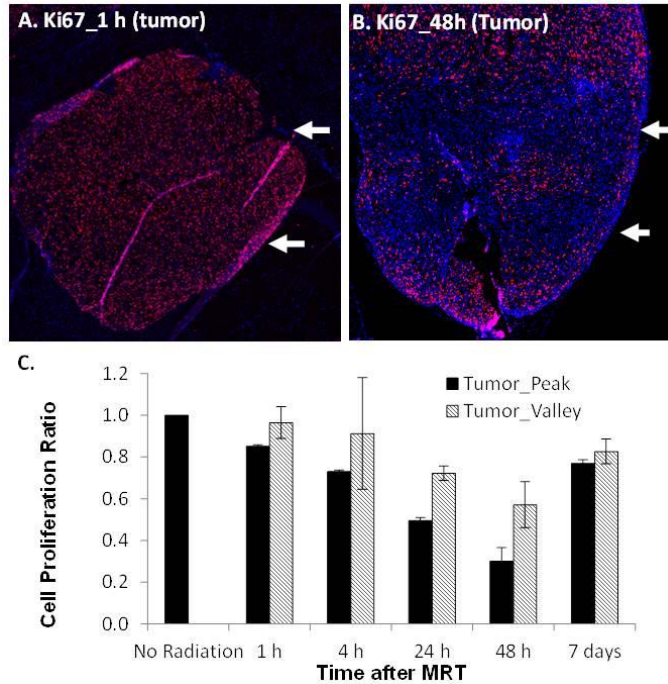


Figure 6.7 Immunofluorescence staining of Ki-67 on tumor as biomarker for cell proliferation 1h (A) and 48h (B) after MRT. Ki-67 positive cells are shown in red, while DAPI counterstaining of the nuclei are shown in blue. White arrows indicate the microbeam radiation paths on the tumor. Ratios of proliferation staining to non-irradiated control are plotted (C) over time for both the peak and valley regions. Proliferation rate continuously decreased from 1h to 48 h, but bounced back at day 7 after MRT. Reprinted with permission from Yuan *et al. Radiation Research* 184, 322-333 (2015).

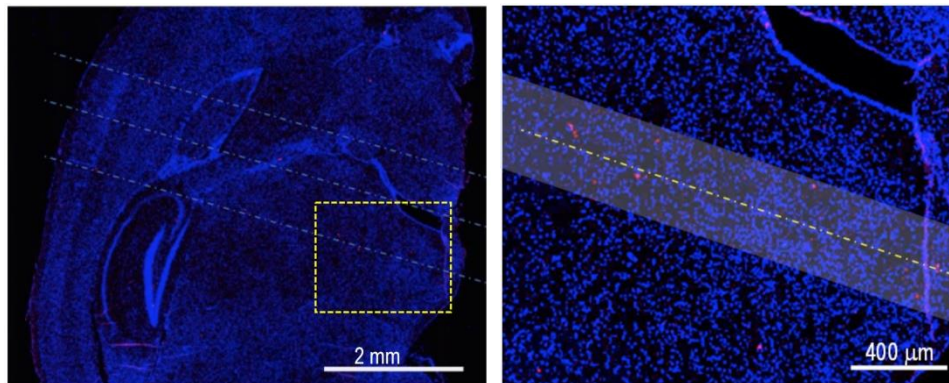


Figure 6.8 Apoptosis in normal mouse brain tissue after MRT. Reprinted with permission from Yuan *et al. Radiation Research* 184, 322-333 (2015).

Proliferation measurement with Ki-67 staining showed that tumor proliferation was significantly reduced in the radiation beam passing region at 1 h after irradiation (average of 15% drop from the non-irradiated control level), and continued to drop at 4, 24 and 48 h after

irradiation (average of 27, 50 and 70% drop, respectively), as shown in Figure 6.7. Tumor cells in the valley dose region had a lower reduction on proliferation compared to the irradiated region (3, 9, 28 and 43% drop at 1, 4, 24, and 48 h after MRT, respectively). However, at day 7, tumor proliferation recovered to the level similar to that at 4 h post-irradiation. The irradiated region and radiation valley region at day 7 had averages of 77 and 83% proliferation levels compared to the non-irradiated tumor tissue, suggesting tumor regrowth after MRT.

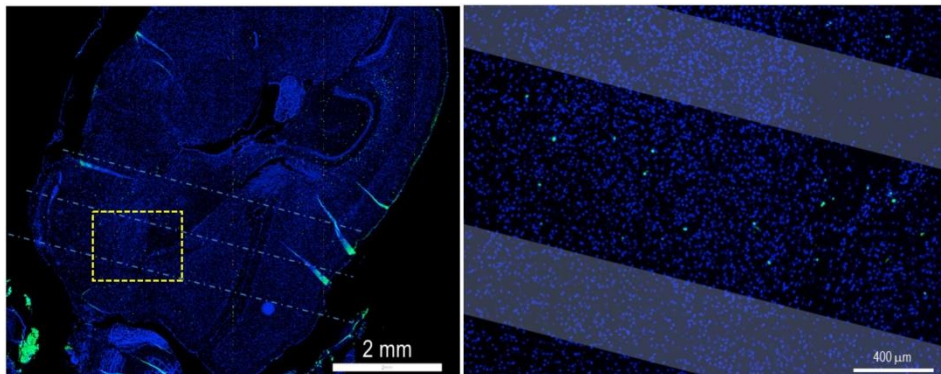
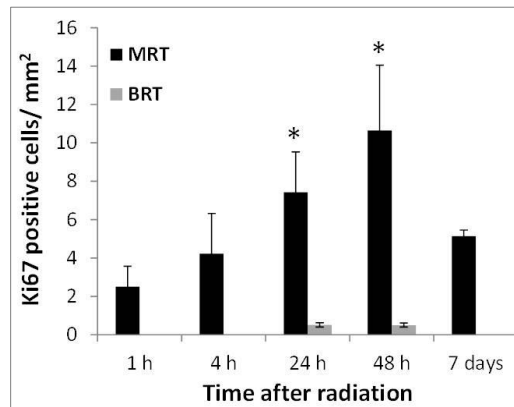


Figure 6.9 Quantification of cell proliferation using Ki-67 immunohistological staining on the contralateral normal mouse brain tissue after MRT and BRT. A significantly higher number of proliferation cells were found in the MRT treated mice, but not in the BRT treated mice at 24h or 48h post-irradiation (* $P < 0.05$, compared to BRT). Reprinted with permission from Yuan *et al. Radiation Research* 184, 322-333 (2015).

In the contralateral normal tissue, there was an increase of cell proliferation after MRT that peaked at 48 h, as shown in Figure 6.9 (top row). The proliferation cells were found mainly in the valley region in the MRT field, as shown in Figure 6.9 (bottom two images). Compared to

the normal brain tissue after BRT, there was a dramatically higher level of cell proliferation in the MRT-treated normal tissue ($7.43 \pm 2.09/\text{mm}^2$ and $10.64 \pm 3.41/\text{mm}^2$ for 24 and 48 h, respectively, for the MRT vs. $0.51 \pm 0.11/\text{mm}^2$ and $0.50 \pm 0.11/\text{mm}^2$ for 24 and 48 h, respectively, for the BRT), which was more than 20 times higher at 48 h after irradiation. The higher proliferation level after MRT suggests a rapid tissue regeneration process in the normal brain tissue after MRT.

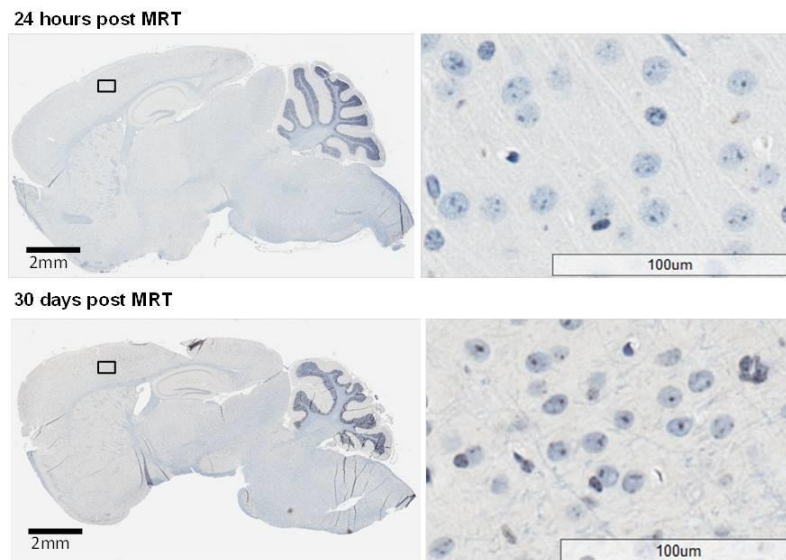


Figure 6.10 F4/80 immunostaining on normal mouse brain tissue at 24 hours and 30 days after MRT. No positively stained macrophages or microglia cells were found at either time point. No other morphological brain tissue damage was detected. Reprinted with permission from Yuan *et al. Radiation Research* 184, 322-333 (2015).

Normal mice were irradiated with the low-dose MRT protocol in the forebrain region, and expressions of γ -H2AX, caspase-3 and F4/80 on normal brain tissue were examined at 24 h and day 30 after MRT. Thirty days after MRT, there was no obvious track of γ -H2AX positive signals, although low γ -H2AX staining signal was found sporadically in the irradiated region. The apoptosis level at 24 h after MRT on normal mouse brain was $0.41 \pm 0.07/\text{mm}^2$, which was much lower than the level at the contralateral normal brain tissue in the tumor mice ($0.66 \pm$

0.12/mm²) ($P = 0.08$). Thirty days after MRT, the apoptosis level in the irradiated region dropped to its lowest ($0.18 \pm 0.04/\text{mm}^2$) compared to all time points examined.

Neither microglial activation nor macrophage infiltration was found on normal brain at 24 h or day 30 after irradiation, as shown in F4/80 staining images (Figure 6.10). There was some nonspecific F4/80 staining in the neuron cells, but no positive staining in microglial or macrophages compared to a positive control.

6.3.6 Preliminary results with MRT delivered in orthogonal arrays

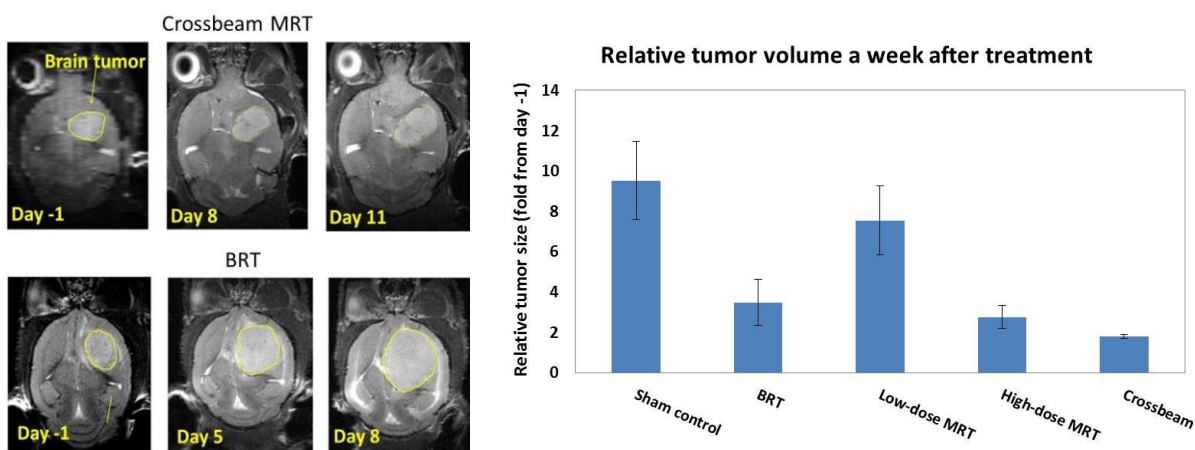


Figure 6.11 Tumor progression monitored by MRI following different treatments. Tumor volume was shown as relative to the volume one day prior to treatment. Adapted from Zhang *et al.* in *Expert Review of Anticancer Therapy* 14 (12), 1411 – 1418 (2014) [4].

Compared to the BRT group where 10 Gy MV radiation was delivered homogeneously to the entire tumor volume, more significant suppression of tumor growth was seen in the animals treated with crossbeam MRT as expected (Figure 6.11). Assuming both arrays were accurately delivered to the tumor target in the crossbeam group, about 50% tumor volume was irradiated by high dose radiation whereas the rest of the tumor cells received minimal exposure. No obvious radiation-induced normal tissue complications such as skin infections or behavior change were detected clinically either in the beam overlapping areas or in microbeam paths with peak doses.

No complete tumor ablation was achieved partially due to the relatively large initial tumor size by the time of treatment and the insufficient valley doses in the crossbeam MRT group.

6.4 Discussion

The work described above was the initial radiobiological studies carried out using the CNT-based image-guided MRT system. The preliminary results showed that the life span of animals in the two MRT-treated groups was significantly extended compared to the sham group even at the relatively low-dose level. Although more than half of the tumor volume was in the valley dose regions, which received lower dose radiation (less than 5 Gy, calculated with the average PVDR of 15), the MST in MRT group was shown similar to that of the 10 Gy BRT group. In-beam dose (peak dose) was 4 – 8 times higher in the MRT than in BRT. No apparent skin complications were found in the treatment area including the peak dose region. Tumor growth was greatly suppressed in the high-dose MRT group over the two-week monitoring period after irradiation, although it did not result in a significant extension of survival compared to the low-dose MRT and BRT group. Animals treated with low-dose MRT had initial tumor suppression, with tumor regrowth at a later phase, which was consistent with the Ki-67 staining of tumor proliferation. Immunostaining of γ -H2AX and cleaved caspase-3 showed higher DNA damage and more apoptosis in tumor tissue compared to normal brain tissue. MRT on normal brain tissue caused low apoptosis and little macrophage infiltration at 30 days after exposure, indicating that normal brain tissue tolerates the prescribed MRT.

The results from the discussed survival study was similar to the synchrotron-based MRT study by Prezado *et al* [10]. They reported an increased life span of about 42% on 9L glioma rats treated with unidirectional MRT (as used in this study) with 100 Gy peak dose, 0.64 mm

beamwidth and 1.12 mm center-to-center distance. In their study, the life span was further increased to 100% when an interlaced microbeam pattern was applied.

Histologically, low level of normal tissue damage was detected in normal mouse brain after MRT with either 48 Gy or 72 Gy. At 48 h post-irradiation, the number of apoptotic cells was significantly fewer in MRT treated animals compared to those received 10 Gy BRT. A low level of apoptosis and no F4/80⁺ macrophages were observed at 24 h or day 30 after MRT in normal mouse brain, indicating a good tolerance to the prescribed dose in MRT. So far, only DNA damage and apoptosis were quantified regarding to the evaluation of normal tissue complications. More physiological and functional assays including blood-brain-barrier and inflammation measurement remain to be investigated for a comprehensive assessment of normal tissue responses.

Although there is yet no conclusive theories to fully explain the preferential effects demonstrated in MRT preclinical studies, the main hypothesis pointed to the fast repair of normal microvessels and the radiation-induced bystander effects (RIBE) [11, 12]. Dilmanian *et al.* also proposed beneficial bystander effects through the release of growth factors after MRT, promoting proliferation, migration and differentiation of the progenitor glial cells to produce new functional glial cells [13]. However, the exact pathway, dynamics and essential molecular elements of bystander effects still require extensive investigation. The results presented here showed over 20 times higher cell proliferation in the MRT treated normal brain compared to those treated with BRT. Crosbie *et al.* reported that normal skin tissue showed increased proliferation starting from 48 h after MRT as one of the tissue-repairing processes [14]. In our study, increased number of Ki-67-positive cells was observed beginning at 24 h and continuing

48 h after MRT of the brain, indicating rapid tissue regeneration and repair from MRT. The mechanisms of normal tissue repair and regeneration warrant further investigation.

One interesting finding from the tissue immunohistological staining is the spreading of the γ -H2AX expression from the radiation peak region to the valley region at 48 h and day 7 after irradiation. A similar situation was also observed in the cleaved caspase-3 stained tissue for apoptosis. Although the ratio of apoptosis in general is relatively low compared to other cell lines after radiation treatment [15], the distribution of the apoptotic cells can be clearly observed. Two mechanisms that might be attributed to this phenomenon are cell migration or bystander effect. Crosbie *et al.* reported on the different responses between tumor cells and normal tissue, with results showing that the irradiated peak and valley zones were indistinguishable in tumors because of extensive cell migration between the zones [14]. Sprung *et al.* also reported that γ -H2AX foci at later time points did not directly correspond with the targeted regions, which suggests cell movement or bystander effects as a potential mechanism for MRT effectiveness. Kashino *et al.* showed that the induction of DNA DSBs and cell migration in glioma cells exposed to MRT in vitro were mediated by bystander effects [16]. Our results are consistent with those studies in terms of indistinguishable damage in tumor tissue. However, extensive mechanistic studies are needed in the future.

The survival time and normal tissue damage from the MRT treated animals were compared with BRT treated animals. The dose level of 10 Gy was chosen for BRT in the study mainly because it has been widely used in small animal studies with single-fraction conventional radiation [12, 17, 18]. However, it is quite a challenge to establish the true biological equivalence in dose between MRT and BR due to the complex dosimetry in MRT. Priyadarshika *et al.* suggested that the integrated dose of MRT, which is the microbeam dose averaged over the

entire radiation volume, might be more relevant than the peak or valley dose when compared to broad-beam radiation [19]. Recently, Ibahim *et al.* conducted serial cell irradiation studies to evaluate the equivalence between synchrotron MRT and conventional BRT, and reported that BRT doses of 3.4 ± 0.1 Gy were radiobiologically equivalent to a peak microbeam dose of 112 Gy (25 μm wide spaced, 175 μm on center) in clonogenic assays on EMT6.5ch cells [17], which is much lower than the integrated MRT dose. On the other hand, the *in vitro* cell radiation study could not truly represent *in vivo* irradiation where possible bystander effects and vascular network factors might greatly influence the final efficacy. It is still debatable which dose level of broad-beam radiation can be used for a comparison with the MRT study. Our study showed that 10 Gy of BRT led to a survival extension similar to MRT. However, the histological results shown in this study indicated that BRT might cause more normal brain tissue damage than MRT. Apoptosis doubled at 48 h in normal brain tissue after BRT compared to MRT, although apoptosis levels in both BRT and MRT groups were very low ($0.65 \pm 0.11/\text{mm}^2$ vs. $0.35 \pm 0.09/\text{mm}^2$, respectively). In addition, Ki-67 staining revealed the number of proliferating cells to be $20 \times$ higher in the normal tissue after MRT than after BRT, which indicates much more rapid tissue repair and recovery after MRT, and thus low damage to normal tissue functionality. Future studies to compare MRT to the clinical standard of care for glioblastoma, i.e., the combination of fractionation radiation and temozolomide [20] will be needed for a more clinically relevant comparison in terms of therapeutic efficacy.

Despite the lack of large statistical sampling, the preliminary results demonstrated that increasing the total integral dose and tumor coverage by spatially distributing the microbeam peak doses into two multi-directional arrays can increase the efficiency in tumor growth delay without serious normal tissue damage. Further investigation is still to be carried out to compare

the therapeutic efficacy to that from the same total dose delivered in a single array. As the true evaluation relies on the accurate dose delivery, implementing MRI/CT with 3D image registration is also desired in future experiments.

The preclinical results discussed above validated the treatment efficacy of the unique dosimetric characteristics generated by the prototype microbeam irradiator. For the current prototype system, two major differences in the beam dosimetric parameters compared to synchrotron-based MRT preclinical experiments are the beamwidth and dose rate. As described earlier, the intrinsically divergent beam is about 300 μm thick at the skin entrance, versus 25 – 75 μm as in classical MRT studies at ESRF beamline ID17. However, increasing evidence has shown that normal tissue sparing effect can be preserved even with a beamwidth of up to several hundred microns, as long as the valley doses were kept under the threshold. MRT with thicker beams (up to 0.68 mm) is usually termed as minibeam radiation therapy, or MBRT, as proposed by Dilmanian *et al* [10, 21-23]. Admittedly, a higher dose rate would largely limit the motion-induced beam blurring and errors in beam delivery. However this is no convincing evidence so far to demonstrate the therapeutic advantage of the extremely high dose rate as produced with synchrotron beamline. The beam blurring originated from the respiration or cardiac pulsation can be eliminated with the physiological gating technique for radiation beam delivery [24].

The dose rate produced by the current prototype microbeam irradiator is comparable with a clinically used radiotherapy system, or any commercially available small animal radiotherapy devices [25]. However, since the microbeam peak doses delivered within a single fraction can be as high as two orders of magnitude higher than the conventional RT, a higher microbeam dose is still desirable in order to deliver the total prescribed dose within the time window allowable for animal anesthesia, and for patient immobilization. A second-generation CNT-based microbeam

irradiator has been constructed and is currently under testing which will potentially provide a more than 20 times higher microbeam dose rate (see chapter 7).

REFERENCES

1. Hadsell, M., *The development and characterization of a first generation carbon nanotube x-ray based microbeam radiation therapy system*, in *Department of Physics and Astronomy*. 2013, University of North Carolina at Chapel Hill. p. 196-254.
2. Zhang, L., et al., *Image-guided microbeam irradiation to brain tumour bearing mice using a carbon nanotube x-ray source array*. *Physics in Medicine and Biology*, 2014. **59**(5): p. 1283.
3. Yuan, H., et al., *Treating Brain Tumor with Microbeam Radiation Generated by a Compact Carbon-Nanotube-Based Irradiator: Initial Radiation Efficacy Study*. *Radiat Res*, 2015. **184**(3): p. 322-33.
4. Zhang, L., et al., *Nanotube x-ray for cancer therapy: a compact microbeam radiation therapy system for brain tumor treatment*. *Expert Rev Anticancer Ther*, 2014. **14**(12): p. 1411-8.
5. Mariotti, L.G., et al., *Use of the γ -H2AX Assay to Investigate DNA Repair Dynamics Following Multiple Radiation Exposures*. *PLoS ONE*, 2013. **8**(11): p. e79541.
6. Zarnescu, O., et al., *Immunohistochemical localization of caspase-3, caspase-9 and Bax in U87 glioblastoma xenografts*. *Journal of Molecular Histology*, 2008. **39**(6): p. 561-569.
7. Nikolaishvilli-Feinberg, N., et al., *Development of DNA Damage Response Signaling Biomarkers using Automated, Quantitative Image Analysis*. *Journal of Histochemistry & Cytochemistry*, 2014. **62**(3): p. 185-196.
8. Winsor, L., *Tissue processing*, in *Laboratory Histopathology*, A.E. Woods and R.C. Ellis, Editors. 1994, Churchill Livingstone: New York p. 4.2-1-4.2-39.
9. Banath, J.P., S.H. Macphail, and P.L. Olive, *Radiation sensitivity, H2AX phosphorylation, and kinetics of repair of DNA strand breaks in irradiated cervical cancer cell lines*. *Cancer Res*, 2004. **64**(19): p. 7144-9.
10. Prezado, Y., et al., *Increase of lifespan for glioma-bearing rats by using minibeam radiation therapy*. *J. Synchrotron Radiat.*, 2012. **19**(Pt 1): p. 60-5.
11. Brauer-Krisch, E., et al., *Effects of pulsed, spatially fractionated, microscopic synchrotron X-ray beams on normal and tumoral brain tissue*. *Mutat. Res.*, 2010. **704**(1-3): p. 160-6.
12. Sabatasso, S., et al., *Microbeam radiation-induced tissue damage depends on the stage of vascular maturation*. *Int J Radiat Oncol Biol Phys*, 2011. **80**(5): p. 1522-32.
13. Dilmanian, F.A., et al., *Tissue-sparing effect of x-ray microplanar beams particularly in the CNS: is a bystander effect involved?* *Exp. Hematol.*, 2007. **35**(4 Suppl 1): p. 69-77.

14. Crosbie, J.C., et al., *Tumor cell response to synchrotron microbeam radiation therapy differs markedly from cells in normal tissues*. *Int. J. Radiat. Oncol. Biol. Phys.*, 2010. **77**(3): p. 886-94.
15. Hara, S., et al., *p53-independent ceramide formation in human glioma cells during γ -radiation-induced apoptosis*. *Cell Death & Differentiation*, 2004. **11**(8): p. 853-861.
16. Kashino, G., et al., *Induction of DNA double-strand breaks and cellular migration through bystander effects in cells irradiated with the slit-type microplanar beam of the spring-8 synchrotron*. *Int. J. Radiat. Oncol. Biol. Phys.*, 2009. **74**(1): p. 229-36.
17. Ibahim, M.J., et al., *An Evaluation of Dose Equivalence between Synchrotron Microbeam Radiation Therapy and Conventional Broadbeam Radiation Using Clonogenic and Cell Impedance Assays*. *PLoS One*, 2014. **9**(6): p. e100547.
18. Sprung, C.N., et al., *DNA damage and repair kinetics after microbeam radiation therapy emulation in living cells using monoenergetic synchrotron X-ray microbeams*. *J Synchrotron Radiat*, 2011. **18**(Pt 4): p. 630-6.
19. Priyadarshika, R., et al., *Biodosimetric quantification of short-term synchrotron microbeam versus broad-beam radiation damage to mouse skin using a dermatopathological scoring system*. 2014.
20. Stupp, R., et al., *Radiotherapy plus concomitant and adjuvant temozolomide for glioblastoma*. *N Engl J Med*, 2005. **352**(10): p. 987-96.
21. Dilmanian, F.A., et al., *Interlaced x-ray microplanar beams: a radiosurgery approach with clinical potential*. *Proc. Natl. Acad. Sci. USA*, 2006. **103**(25): p. 9709-14.
22. Dilmanian, F.A., et al., *Microbeam radiation therapy: Tissue dose penetration and BANG-gel dosimetry of thick-beams' array interlacing*. *European Journal of Radiology*, 2008. **68**(3, Supplement): p. S129-S136.
23. Deman, P., et al., *Monochromatic Minibeams Radiotherapy: From Healthy Tissue-Sparing Effect Studies Toward First Experimental Glioma Bearing Rats Therapy*. *International Journal of Radiation Oncology*Biophysics*, 2012. **82**(4): p. e693-e700.
24. Chtcheprov, P., et al., *Physiologically gated microbeam radiation using a field emission x-ray source array*. *Med Phys*, 2014. **41**(8): p. 081705.
25. Verhaegen, F., P. Granton, and E. Tryggestad, *Small animal radiotherapy research platforms*. *Phys. Med. Biol.*, 2011. **56**(12): p. R55-83.

CHAPTER 7: CONCLUSIONS AND PROSPECTS

7.1 Summary of This Work

Microbeam radiation therapy is a radical experimental RT modality for cancer treatment, with remarkable preferential tumoricidal effects that have been demonstrated in preclinical studies. It differs dramatically from conventional RT modalities with a highly confined radiation field with orders of magnitude higher flux delivered within one fraction. The unique dosimetric characteristics yield an unprecedented therapeutic outcome, but also pose a great challenge in microbeam radiation production using conventional methods. Other than the national synchrotron facilities that are currently employed as the sole source of microbeam radiation, compact and economically viable technologies for microbeam generation is largely desired to translate the promising RT modality from preclinical investigation to clinical application.

The novel CNT x-ray source array technology overcomes the limitations of conventional orthovoltage tubes and makes it possible to develop a first of its kind compact laboratory-scale MRT systems for cancer research and provides a potential pathway for clinical translation. Compared to the current synchrotron-based MRT facilities, CNT-based MRT also has several intrinsic advantages, including orders of magnitude lower in dimensions and cost. The electronically controlled and near-instantaneous beam response ensures a great reliability and safety in radiation dose delivery as desired in clinical uses. Additionally, the programmable source control allows for physiologically gated radiation delivery where radiation exposure is synchronized with the respiratory or cardiac signals, to minimize motion-induced microbeam

blur during treatment [1]. Work from this dissertation presented the development, characterization, and preclinical evaluation of the first prototype CNT-based image-guided microbeam radiation therapy system. The effort mainly focused on two specific aspects, i.e. development and optimization of system characterization, dosimetry calibration, implementation of image guidance for microbeam delivery, and preliminary radiobiological studies. The first part detailed the effort in improving the system performance in terms of stability and heat management. Modifications have been made to the anode assembly in order to alleviate the vibration induced anode rotation. While further effort is still needed in the complete motion isolation with alternative in the design of the anode assembly, heat related anode deformation should be reduced in the next-generation prototype where an active oil cooling system is employed. Radiation source and beam dosimetric characterization with Gafchromic EBT3 films was described in detail. While EBT3 film offers great sensitivity and accuracy of dosimetry in the lower dose range, other films with a larger dynamic dose range such as Gafchromic HD-810 might be desirable as the prescribed dose levels increase in future studies.

On-board image guidance is implemented, for the first time, in microbeam radiation delivery. A CNT-based micro-CT was constructed and integrated with microbeam irradiator in the same chamber. Dedicated multi-modality imaging and registration methods have been developed to facilitate the delivery of microbeams radiation in small animal models. The evaluation using brain tumor bearing mice yielded a high consistency and accuracy in beam targeting. Orthogonally crossed multi-array microbeam radiation therapy was demonstrated feasible with the aid of 3D MRI/CT guided targeting method. The image-guidance protocols established in this work bring the system development a step further towards preclinical evaluations.

The first MRT biological assessments using the compact MRT system were conducted and the key findings were presented in detail in Chapter 6. Effective tumor control and lifespan extension without clinical normal tissue complications were demonstrated in U87MG human glioma bearing mice treated with the prototype system. Further investigation in cellular responses with histopathological staining revealed elevated levels of DNA damages and apoptosis in tumor versus normal tissue after microbeam irradiation. Less damage was also confirmed in low-dose MRT treated normal tissue compared to that irradiated with conventional broad beams. Rapid repair in normal tissue was identified histologically in microbeam irradiated normal tissue.

7.2 High-power Compact MRT System

7.2.1 The second-generation prototype

Although the feasibility of the CNT source array technology for microbeam radiation therapy has been demonstrated with the first prototype irradiator, the full potential of this technology for higher flux production remains to be explored. The maximum dose rate achievable using the first prototype is around 1.2 Gy/min at the entrance plane. This dose rate is considered sufficient as a preclinical and a clinical RT system, but it is not ideal to achieve the extremely high peak dose typically utilized in MRT. Besides, a higher dose rate is needed when physiologically gated radiation delivery is employed, which generally requires substantially longer treatment time compared to non-gated dose delivery. The achievable radiation flux is currently limited by the relatively low efficiency in the anode heat dissipation in the first prototype system. Higher power output can be potentially achieved by introducing active anode cooling device, or by implementing a rotating cylindrical anode.

A second-generation CNT-MRT system has been constructed and is currently under conditioning and calibration, as illustrated in Figure 7.1. An active oil cooled device is incorporated into this upgraded system to increase anode heat capacity and radiation output. Three cathode arrays generate 3 parallel microplanar beams simultaneously, with an anticipated 20 times higher dose rate and a higher mean photon beam energy compared to the first prototype device (Table 7.1). This will allow for high dose (200 – 700 Gy) delivery within 1 hour for small animal irradiation.

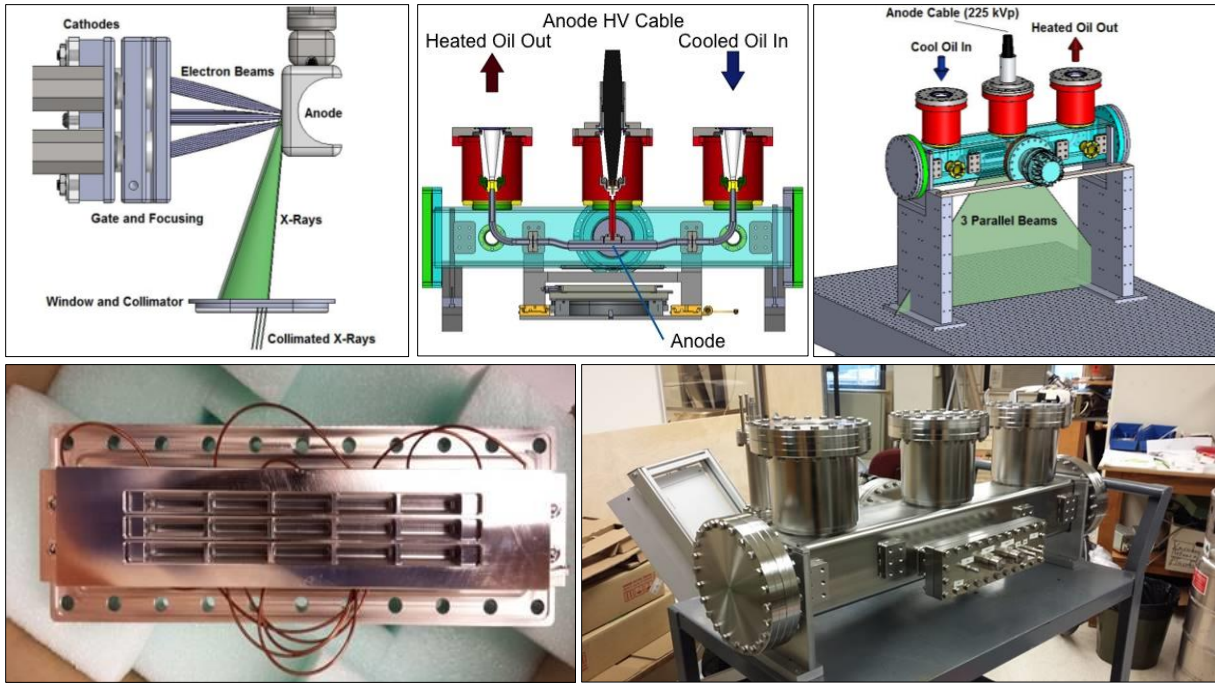


Figure 7.1 Top row: design of concept of the second-generation compact MRT system with three CNT cathodes arrays. A specially designed oil cooling system is incorporated in this upgraded system to increase anode heat capacity and radiation output. Three microbeams with adjustable width can be generated simultaneously. Bottom row: a photograph of the three-line cathode assembly is shown on left; on right shows a photograph of the vacuum chamber of the second-generation system.

7.2.2 Design for human MRT with multiple beam arrays

Perhaps the only way for MRT to benefit brain cancer treatment is through spatial distribution of beam arrays. With this distribution, the physical dose conformality from spatial modulation of radiation beam, and the biological tissue specificity from MRT can be combined

to widen the therapeutic window and to improve treatment outcomes. Particularly, the CNT distributed source arrays with simultaneous dose delivery from different ports/directions, has the advantages of a single fraction MRT treatment less patient motion, short hospitalization time, and reduced amounts of anesthesia for patients. Figure 7.2 illustrates the design of concept of a CNT-based human MRT system with microbeam array spatially distributed in a circular configuration. Radiation from each direction is individually collimated with both microbeam collimator and conformal collimator. Each microbeam is generated by a cathode array and can be thus electronically controlled individually. This design would reduce the toxicity to skin and subcutaneous tissue caused by high dose orthovoltage radiation and improve the radiation dose delivery to deep-seated and invasive tumor targets.

Table 7.1 Comparison of the system specifications of the first and second generation CNT-based MRT prototypes

CNT-based Compact MRT Systems		
Parameters	First prototype	Second-generation
Number of CNT source arrays	1	3
Peak beam energy	160 kV	225 kV
Mean power	384 W	6750 W
Focal line size	200 μm \times 160 mm	200 μm \times 160 mm
Anode cooling	Passive	Active oil cooling
Average dose rate (entrance)	1.2 Gy/min	25 Gy/min
Microbeam width	Adjustable	Adjustable
On-board imager	Micro-CT	Micro-CT
Additional feature	Physiologically gated MRT	

7.3 Future Directions

Microbeam radiation therapy is attractive and promising in many ways. As a novel RT modality, its potential impact on the clinical practice of cancer management as well as

fundamental radiobiological research in oncology is revolutionary and cannot be overestimated. In recent years MRT research has attracted worldwide attention from various research groups within the synchrotron communities and beyond. A lot of progress has been made towards a better understanding of the underlying therapeutic mechanism, which is beneficial not only the development of MRT as a single treatment modality, but also inspiring as for cancer therapy in general. Other than the potential as a single RT modality, a few additional aspects of MRT remain to be explored including dose enhancement with radiosensitizers, the feasibility as a combined treatment with chemotherapy, potential utilization in whole-body RT for immunotherapy, etc. Ideally, microbeam radiation therapy would contribute to the eventual realization of an effective cure for brain malignancies in the foreseeable future.

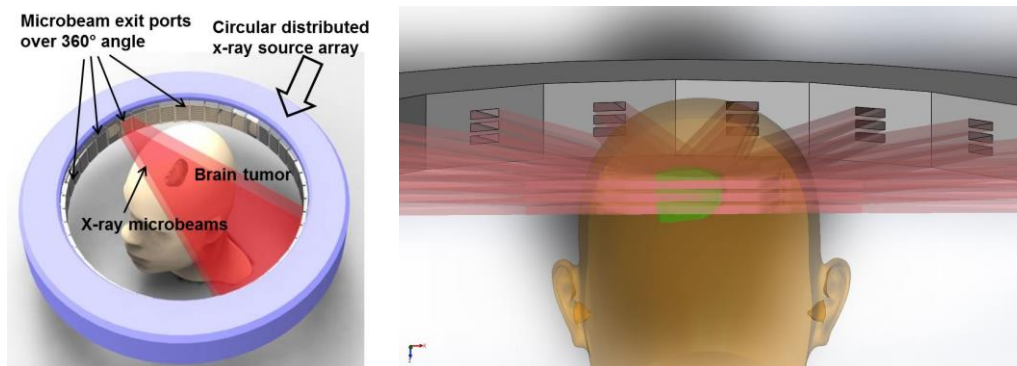


Figure 7.2 Schematic illustration of the CNT-based human MRT system in a circular design. Microbeam are generated from distributed CNT source arrays from multiple directions and directed towards the treatment target simultaneously. Each beam array contains multiple microbeams for which the beamwidth and lengths can be adjusted individually. Figures were not drawn to scale. Picture on the left is adapted from Zhang *et al. Expert Review of Anticancer Therapy* 14(12), 1411-1418 (2014) [2]

REFERENCES

1. Chtcheprov, P., et al., *Physiologically gated microbeam radiation using a field emission x-ray source array*. Med Phys, 2014. **41**(8): p. 081705.
2. Zhang, L., et al., *Nanotube x-ray for cancer therapy: a compact microbeam radiation therapy system for brain tumor treatment*. Expert Rev Anticancer Ther, 2014. **14**(12): p. 1411-8.